

EFFECT OF COBALT DOPING ON PHOTOCATALYTIC ACTIVITY OF LEAD
TITANATE

A THESIS SUBMITTED TO
THE GRADUATE SCHOOL OF NATURAL AND APPLIED SCIENCES
OF
MIDDLE EAST TECHNICAL UNIVERSITY

BY

SELDA ODABAŞI

IN PARTIAL FULFILLMENT OF THE REQUIREMENTS
FOR
THE DEGREE OF MASTER OF SCIENCE
IN
CHEMICAL ENGINEERING

AUGUST 2018

Approval of the thesis:

**EFFECT OF COBALT DOPING ON PHOTOCATALYTIC ACTIVITY OF
LEAD TITANATE**

submitted by **SELDA ODABAŞI** in partial fulfillment of the requirements for the degree of **Master of Science in Chemical Engineering Department, Middle East Technical University** by,

Prof. Dr. Halil Kalıpçılar
Dean, Graduate School of **Natural and Applied Sciences** _____

Prof. Dr. Pınar Çalık
Head of Department, **Chemical Engineering** _____

Prof. Dr. Deniz Üner
Supervisor, **Chemical Engineering Dept., METU** _____

Examining Committee Members:

Prof. Dr. Oğuz Gülseren
Physics Dept., Bilkent University _____

Prof. Dr. Deniz Üner
Chemical Engineering Dept., METU _____

Dr. Selçuk Yerci
Electrical And Electronics Engineering Dept., METU _____

Dr. Bahar İpek
Chemical Engineering Dept., METU _____

Dr. Emre Büküşoğlu
Chemical Engineering Dept., METU _____

Date: 20.07.2018

I hereby declare that all information in this document has been obtained and presented in accordance with academic rules and ethical conduct. I also declare that, as required by these rules and conduct, I have fully cited and referenced all material and results that are not original to this work.

Name, Last name : Selda Odabaşı

Signature :

ABSTRACT

EFFECT OF COBALT DOPING ON PHOTOCATALYTIC ACTIVITY OF LEAD TITANATE

Odabaşı, Selda
MSc, Department of Chemical Engineering
Supervisor: Prof. Dr. Deniz Üner

August 2018, 92 pages

The effect of cobalt doping on photocatalytic activity of lead titanate was studied by NO oxidation and TP_x analyses. PbTiO₃, Pb_{0.875}Co_{0.125}TiO₃, Pb_{0.75}Co_{0.25}TiO₃ and Pb_{0.5}Co_{0.5}TiO₃ were synthesized by sol-gel method. Temperature programmed reduction and UV-desorption experiments were used to demonstrate the reducibility of TiO₂, which is a commercial photocatalyst, 0.5 wt% Pt/TiO₂ and synthesized perovskites under UV irradiation. By comparing the amount of hydrogen used to reduce fresh and UV treated samples, the reducibility of samples by UV treatment was analyzed. It was found that TiO₂ was reduced around 125°C and between 200°C and 700°C. Platinum oxide was reduced around 50°C and 130°C by UV irradiation. The amount of hydrogen to reduce UV treated PbTiO₃ was more than to reduce fresh PbTiO₃. However, UV treated PbTiO₃ was reduced at lower temperatures. The amount of hydrogen to reduce UV treated Pb_{0.875}Co_{0.125}TiO₃ was less than to reduce fresh Pb_{0.875}Co_{0.125}TiO₃ and UV treated Pb_{0.875}Co_{0.125}TiO₃ was reduced at lower temperatures. The amount of hydrogen to reduce UV treated Pb_{0.75}Co_{0.25}TiO₃ was less than to reduce fresh Pb_{0.75}Co_{0.25}TiO₃ and UV treated Pb_{0.75}Co_{0.25}TiO₃ was reduced at lower temperatures. The amount of hydrogen to reduce UV treated Pb_{0.5}Co_{0.5}TiO₃ was more than to reduce fresh Pb_{0.5}Co_{0.5}TiO₃. However, UV treated Pb_{0.75}Co_{0.25}TiO₃ was reduced at lower temperatures. Photocatalytic activity of synthesized perovskite samples was analyzed by photocatalytic NO oxidation under UV and visible light irradiation. The amount of hydrogen consumption increased with increasing cobalt amount in perovskites. The effect of flow rate and relative humidity in air were

investigated. For all synthesized perovskites, it was observed that increasing flow rate resulted in a decrease in NO conversion. It means that photocatalytic NO oxidation reaction was kinetic controlled. For lead titanate, as relative humidity increases NO conversion increases under UV irradiation. However, for Co-doped perovskites, as relative humidity increases NO conversion decreases under UV irradiation. It is seen that water poisons the surface of Co-doped perovskites. Dark-light cycling NO oxidation experiments were conducted to see the stability of perovskites. Increasing humidity provided better stability for all perovskites.

Keywords: Photocatalysis, Photocatalytic Oxidation, Lead Titanate, Oxygen Vacancy, Cobalt

ÖZ

KOBALT İLAVESİNİN KURŞUN TİTANATIN FOTOKATALİTİK AKTİVİTESİNE ETKİSİ

Odabaşı, Selda
Yüksek Lisans, Kimya Mühendisliği Bölümü
Tez Yöneticisi: Prof. Dr. Deniz Üner

Ağustos 2018, 92 sayfa

Kobalt ilavesinin kurşun titanatın fotokatalitik aktivitesine etkisi NO oksitlenmesi ve sıcaklık programlı analizlerle incelendi. $PbTiO_3$, $Pb_{0.875}Co_{0.125}TiO_3$, $Pb_{0.75}Co_{0.25}TiO_3$ ve $Pb_{0.5}Co_{0.5}TiO_3$ ince asıltılı pelte methoduyla sentezlendi. Sıcaklık programlı indirgenme ve UV-desorplama deneyleri, ticari olarak alınmış TiO_2 , kütlece 0.5% Pt içeren TiO_2 ve sentezlenen perovskitlerin UV ışınlanması altında indirgenebilirliğini kanıtlamak için kullanıldı. Hiç kullanılmamış numune ve UV ışınlanmasına maruz kalmış numuneyi indirgemek için harcanan hidrojen miktarları karşılaştırmasıyla UV ışınlanması yardımıyla indirgenebilirlik analiz edildi. TiO_2 'nin 125°C ve 200°C ile 700°C arasında UV yardımıyla indirgendiği gözlemlendi. Platinum oksitse 50°C ve 130°C UV ışınlanmasıyla indirgendi. UV ışınlanmasına maruz kalmış $PbTiO_3$ 'ü indirgemek için kullanılan hidrojen miktarının hiç kullanılmamış $PbTiO_3$ 'tan daha fazla olduğu fakat UV ışınlanmasına maruz kalmış $PbTiO_3$ 'ün daha düşük sıcaklıklarda indirgenebildiği görüldü. UV ışınlanmasına maruz kalmış $Pb_{0.875}Co_{0.125}TiO_3$ 'ü indirgemek için kullanılan hidrojen miktarının hiç kullanılmamış $Pb_{0.875}Co_{0.125}TiO_3$ 'tan daha az olduğu ve UV ışınlanmasına maruz kalmış $Pb_{0.875}Co_{0.125}TiO_3$ 'ün daha düşük sıcaklıklarda indirgenebildiği görüldü. UV ışınlanmasına maruz kalmış $Pb_{0.75}Co_{0.25}TiO_3$ 'ü indirgemek için kullanılan hidrojen miktarının hiç kullanılmamış $Pb_{0.75}Co_{0.25}TiO_3$ 'tan daha az olduğu ve UV ışınlanmasına maruz kalmış $Pb_{0.75}Co_{0.25}TiO_3$ 'ün daha düşük sıcaklıklarda indirgenebildiği görüldü. UV ışınlanmasına maruz kalmış $Pb_{0.5}Co_{0.5}TiO_3$ 'ü indirgemek için kullanılan hidrojen

miktarının hiç kullanılmamış $Pb_{0.5}Co_{0.5}TiO_3$ 'tan daha fazla olduğu fakat UV ışınlanmasına maruz kalmış $Pb_{0.5}Co_{0.5}TiO_3$ 'ın daha düşük sıcaklıklarda indirgenebildiği görüldü. Sentezlenen perovskit örneklerinin fotokatalitik aktiviteleri, UV ışınlanması ve görünür ışık altında fotokatalitik NO oksitlemesiyle analiz edildi. Akış hızının ve havadaki bağıl nemin etkisi incelendi. Sentezlenen bütün perovskitler için, akış hızının artması NO dönüşümünü azalttı. Bu fotokatalitik NO oksitlemesi tepkimesinin kinetik parametreler tarafından kontrol edildiğini gösterdi. Kurşun titanat için UV ışınlanması altında NO dönüşümü artan bağıl nemle birlikte arttı. Fakat, kobalt ilave edilmiş perovskitler için artan bağıl nemle UV ışınlanması altında daha az NO dönüşümü elde edildi. Bu kobalt ilave edilmiş perovskitler için suyun yüzeyi zehirlediğini gösterdi. Karanlık-aydınlık periyodik NO oksitlenmesi deneyleriyle perovskitlerin sabitliğini gözlemlendi. Bağıl nemin tüm perovskitlerin sabitliğine katkısı olduğu görüldü.

Anahtar Kelimeler: Fotokataliz, Fotokatalitik oksitleme, Kurşun Titanat, Oksijen Boşluğu, Kobalt

To my parents

ACKNOWLEDGEMENTS

First of all, I would like to express my profound and sincere gratitude to my supervisor Prof Dr. Deniz Üner for her continuous support, guidance, motivation and generous advice throughout my master studies. It was a privilege and an honor to be a part of her research group. Her kindness, patience, insightfulness and wisdom helped me a lot about my studies and in every sphere of my life. She was always more than a thesis supervisor.

I would like to thank Prof. Dr. Mehmet Parlak for his help and guidance in light intensity measurements experiments. I, also, would like to thank Prof. Dr. Saim Özkar and Dr. Serdar Akbayrak for their help and guidance in diffuse reflectance measurements. I am grateful to Orhun Kahraman for his help in NO oxidation experiments, Begüm Yılmaz for her help in calorimetry experiments and Mustafa Yasin Aslan for his help in chemisorption experiments.

I want to thank all the present and former members of Cactus research group. Their help and friendship gave me strength. I, especially, want to express my thankfulness to Atalay Çalışan, Ezgi Yavuzyılmaz, Zeynep Öztan, Deniz Kaya, Hale Ay and Taymaz Tabari.

Technical staff of chemical engineering department; Mihrican Açıkgöz, Cemil Araçlı, İsa Çağlar, Mustafa Cansuyu were appreciated for their kindness and technical support.

The Scientific and Research Council of Turkey (TÜBİTAK, Research Grant No: 117M040) was acknowledged for the financial support during my studies.

I would like to express my special thanks to Merve Sarıyer, Özge Batır, Canan Aksoy, Merve Özkutlu, Gökhan Gök and Fatma Şahin for their friendship and support. I am thankful to my roommates in C Block; Fatma Betül Oflaz and Ezgi Gözde for their kind friendship.

I would like to thank my roommates Semanur Kandil and Selay Atışlı for being a family for me. Without their warm friendship, I would not laugh a lot and enjoy my last two years. I also want to thank my friends: Gözde Şahin, Esranur Yıldırım and Özge Erdem for the laughter and inspiration they provided me throughout my whole university life. I am grateful to my former roommates; Hande Kayma, Şebnem Çetken and Özlem Atmaca and my close friends; Pelin Savcı, Seha Demirel, İlayda Tokatlı and Ecem Kahyaoğlu. Ankara was shining brighter by courtesy of those people.

My dear bird-son, Nabi the cockatiel, was warmly acknowledged for the love, joy and happiness he gave me.

I always think that I am very lucky to be the daughter of my dad and mom. I want to express my thankfulness to my parents, my brother and my grandparents. They were always supportive and they always helped me when I wanted to spread my wings and fly away. I want to thank my cousin Esra Pak for being there for me when I needed to have a heart-to-heart talk and my cousin Burcu Yılmaz for introducing me a new world.

Lastly, I want to express my deepest gratitude to Dong Hyeok Lee for motivation, support and love. He always cheered me up whenever I needed him.

TABLE OF CONTENTS

ABSTRACT	v
ÖZ	vii
ACKNOWLEDGEMENTS	x
TABLE OF CONTENTS	xii
LIST OF FIGURES	xv
LIST OF TABLES	xviii
LIST OF SYMBOLS	xx
CHAPTERS	
1 INTRODUCTION	1
1.1 Oxygen Vacancies in Catalysis	1
1.2 Methods of Creating Oxygen Vacancies	2
1.3 Methods of Healing Oxygen Vacancies	4
1.4 Objectives	5
2 LITERATURE REVIEW	7
2.1 Perovskites	7
2.1.1 Lead Titanate (PbTiO ₃)	9
2.1.1.1 Lead Titanate Applications	10
2.1.1.2 Synthesis Methods of Lead Titanate	12
2.1.1.2.1 Sol-gel Method	12
2.1.1.2.2 Solid State Reaction	13
2.1.1.2.3 Hydrothermal Synthesis	13
2.1.1.2.4 Other Methods	13
2.1.1.3 Oxygen Vacancy Formation in Lead Titanate	15
2.1.1.4 The Photocatalytic NO Oxidation over Lead Titanate	18

2.1.1.5	Doping lead titanate by other atoms.....	24
2.1.1.5.1	Doping A site of Lead Titanate.....	24
2.1.1.5.2	Doping B site of Lead Titanate.....	25
3	MATERIALS AND METHODS.....	27
3.1	Materials.....	27
3.2	Synthesis Method.....	27
3.2.1	Synthesis of PbTiO ₃ by Sol-Gel Method.....	27
3.2.2	Synthesis of Pb _x CO _{1-x} TiO ₃ by Sol-Gel Method.....	28
3.3	Characterization Methods.....	29
3.3.1	XRD Analysis.....	29
3.3.2	UV-Vis Spectroscopy.....	29
3.3.3	BET Analysis.....	30
3.3.4	DSC Analysis.....	30
3.3.5	ICP Analysis.....	30
3.4	NO Oxidation Experiments.....	30
3.4.1	Coating Method.....	30
3.4.2	NO Oxidation Experimental Set up.....	31
3.4.3	NO Oxidation Experimental Procedure.....	32
3.5	TP _x Analysis.....	33
3.6	Adsorption Measurements and Adsorption Calorimetry.....	34
4	RESULTS.....	35
4.1	XRD Analysis.....	35
4.2	UV-Vis Analysis.....	36
4.3	BET Analysis.....	37
4.4	DSC Analysis.....	37
4.5	ICP- OES Analysis.....	38
4.6	TP _x Analyses.....	39

4.6.1	TRP of TiO ₂ before and after UV-irradiation exposure	39
4.6.2	TPR of 0.5 wt% Pt/TiO ₂ before and after UV-irradiation exposure	41
4.6.3	TPR of lead titanate before and after UV-irradiation exposure	42
4.6.4	TPR of Pb _{0.875} Co _{0.125} TiO ₃ before and after UV-irradiation exposure ..	43
4.6.5	TPR of Pb _{0.75} Co _{0.25} TiO ₃ before and after UV-irradiation exposure.....	44
4.6.6	TPR of Pb _{0.5} Co _{0.5} TiO ₃ before and after UV-irradiation exposure	44
4.6.7	TPR of fresh perovskites	46
4.7	NO Oxidation Experiments	48
4.7.1	Effect of Flow rate on Photocatalytic NO Oxidation	48
4.7.1.1	Photocatalytic NO Oxidation in 0 RH% in Air	49
4.7.1.2	Photocatalytic NO Oxidation in 50 RH% in Air	53
4.7.2	Effect of Relative Humidity on Photocatalytic NO Oxidation	57
4.7.3	Dark-Light Cyclic Photocatalytic NO Oxidation Experiments.....	59
4.7.3.1	Dark-Light Cyclic Photocatalytic NO Oxidation Experiments in 0% RH in air	59
4.7.3.2	Dark-Light Cyclic Photocatalytic NO Oxidation Experiments in 50% RH in air	60
4.8	Adsorption Measurements and Adsorption Calorimetry.....	61
5	CONCLUSION.....	65
	REFERENCES	67
	APPENDIX A	77
	APPENDIX B.....	79
	APPENDIX C	81
	APPENDIX D	85
	APPENDIX E.....	91

LIST OF FIGURES

Figure 1.1 Schematic description of the oxygen photodesorption (adapted from [6] with permission).....	3
Figure 1.2 Desorption of oxygen by UV-treatment and heat treatment (adapted from [7] with permission)	3
Figure 1.3 The correlation between photodesorption of oxygen and photo-oxidation of CO to CO ₂ [11]	4
Figure 1.4 Photocatalytic water splitting on lead titanate (adapted from [14] with permission).....	5
Figure 2.1 The scheme of the relationship between electrically polarizable and magnetically polarizable properties [18].....	8
Figure 2.2 Lead titanate structure in cubic paraelectric phase and in tetragonal ferroelectric phase (adapted from [31] with permission).....	10
Figure 2.3 The cubic PbTiO ₃ crystal with an oxygen vacancy (adapted from [63] with permission).....	16
Figure 2.4 The tetragonal PbTiO ₃ crystal with an oxygen vacancy in dimerized Ti–O–Ti chains (adapted from [63] with permission).....	16
Figure 2.5 Effect of total flow rate on photocatalytic activity of TiO ₂ (adapted from [75] with permission)	19
Figure 2.6 The effect of relative humidity on the photocatalytic NO oxidation over TiO ₂ (adapted from [75] with permission).....	20
Figure 2.7 Change in the concentrations of NO (a) and NO ₂ (b) during photocatalytic oxidation (adapted from [74] with permission).....	21
Figure 2.8 Dark-light cyclic experiments over perovskite structures under full spectrum (adapted from [74] with permission).....	22
Figure 2.9 Photocatalytic NO Oxidation Pb ₂ Bi ₄ Ti ₅ O ₁₈ showed over with various nanoscale morphologies under visible light (adapted from [76] by permission).....	23
Figure 2.10 Photocatalytic NO Oxidation over SrTiO ₃ and LaFeO ₃ under visible light (adapted from [77] with permission)	24

Figure 3.1 Chemical structures (a: Lead (II) Acetate Trihydrate, b: Cobalt (II) Acetate Tetrahydrate, c: Titanium (IV) Isopropoxide, d: Citric Acid e: Ethanol, f: Acetic Acid Glacial).....	28
Figure 3.2 Coated samples on flat glass (a: PbTiO_3 , b: $\text{Pb}_{0.875}\text{Co}_{0.125}\text{TiO}_3$, c: $\text{Pb}_{0.75}\text{Co}_{0.25}\text{TiO}_3$, d: $\text{Pb}_{0.5}\text{Co}_{0.5}\text{TiO}_3$)	31
Figure 3.3 Experimental set up for NO oxidation over photocatalysts (adapted from [75] with permission)	32
Figure 4.1 XRD patterns of PbTiO_3 , $\text{Pb}_{0.875}\text{Co}_{0.125}\text{TiO}_3$, $\text{Pb}_{0.75}\text{Co}_{0.25}\text{TiO}_3$, $\text{Pb}_{0.5}\text{Co}_{0.5}\text{TiO}_3$	35
Figure 4.2 UV-Visible Diffuse Reflectance Spectra of PbTiO_3 , $\text{Pb}_{0.875}\text{Co}_{0.125}\text{TiO}_3$, $\text{Pb}_{0.75}\text{Co}_{0.25}\text{TiO}_3$, $\text{Pb}_{0.5}\text{Co}_{0.5}\text{TiO}_3$	36
Figure 4.3 DSC curve of PbTiO_3 , $\text{Pb}_{0.875}\text{Co}_{0.125}\text{TiO}_3$ and $\text{Pb}_{0.75}\text{Co}_{0.25}\text{TiO}_3$	38
Figure 4.4 TPR profile of TiO_2 after and before photodesorption	39
Figure 4.5 TPR profile of 0.5 wt% Pt/ TiO_2 after and before photodesorption	41
Figure 4.6 TPR profile of PbTiO_3 before and after photodesorption	42
Figure 4.7 TPR profile of $\text{Pb}_{0.875}\text{Co}_{0.125}\text{TiO}_3$ before and after photodesorption	43
Figure 4.8 TPR profile of $\text{Pb}_{0.75}\text{Co}_{0.25}\text{TiO}_3$ before and after photodesorption	44
Figure 4.9 TPR profile of $\text{Pb}_{0.5}\text{Co}_{0.5}\text{TiO}_3$ before and after photodesorption.....	45
Figure 4.10 TPR profile of synthesized perovskites and Co_3O_4	46
Figure 4.11 Photocatalytic NO Oxidation over PbTiO_3 at various flow rates	49
Figure 4.12 Photocatalytic NO Oxidation over $\text{Pb}_{0.875}\text{Co}_{0.125}\text{TiO}_3$ at various flow rates	50
Figure 4.13 Photocatalytic NO Oxidation over $\text{Pb}_{0.75}\text{Co}_{0.25}\text{TiO}_3$ at various flow rates	51
Figure 4.14 Photocatalytic NO Oxidation over $\text{Pb}_{0.5}\text{Co}_{0.5}\text{TiO}_3$ at various flow rates.....	52
Figure 4.15 Photocatalytic NO Oxidation over PbTiO_3 at various flow rates	53
Figure 4.16 Photocatalytic NO Oxidation over $\text{Pb}_{0.875}\text{Co}_{0.125}\text{TiO}_3$ at various rates ..	54
Figure 4.17 Photocatalytic NO Oxidation over $\text{Pb}_{0.75}\text{Co}_{0.25}\text{TiO}_3$ at various flow rates	55
Figure 4.18 Photocatalytic NO Oxidation over $\text{Pb}_{0.5}\text{Co}_{0.5}\text{TiO}_3$ at various flow rates.....	56
Figure 4.19 Dark-Light Cyclic Photocatalytic NO Oxidation over perovskites in 0% RH	59

Figure 4.20 Dark-Light Cyclic Photocatalytic NO Oxidation over perovskites in 50% RH.....	61
Figure 4.21 H ₂ O adsorption isotherms for TiO ₂ , PbTiO ₃ , Pb _{0.875} Co _{0.125} TiO ₃ , Pb _{0.75} Co _{0.25} TiO ₃ and Pb _{0.5} Co _{0.5} TiO ₃ at 50°C	62
Figure 4.22 Differential heats of H ₂ O adsorption on TiO ₂ , PbTiO ₃ and Pb _{0.875} Co _{0.125} TiO ₃ at 50°C	63
Figure A.1 The color of mixtures that contains LAT, CAT and solvents (a: PbTiO ₃ , b: Pb _{0.875} Co _{0.125} TiO ₃ , c: Pb _{0.75} Co _{0.25} TiO ₃ , d: Pb _{0.5} Co _{0.5} TiO ₃)	77
Figure A.2 The color of gel formed after the addition of CA- ethanol mixture (a: PbTiO ₃ , b: Pb _{0.875} Co _{0.125} TiO ₃ , c: Pb _{0.75} Co _{0.25} TiO ₃ , d: Pb _{0.5} Co _{0.5} TiO ₃).....	78
Figure B.1 The photoreactor used in photocatalytic NO Oxidation experiments.....	79
Figure D.1 c _{A0} vs τ graph for CSTR assumption.....	86
Figure D.2 c _{A0} vs τ graph for CSTR assumption (τ=2 is omitted).....	87
Figure D.3 ln (c _{A0} /c _A) vs τ graph for PFR Assumption	88
Figure E.1 TPR profile of Pb _{0.875} Co _{0.125} TiO ₃ before and after photodesorption	91

LIST OF TABLES

Table 2.1 Properties of some perovskite oxides (adapted from [17] with permission)	9
Table 2.2 Lattice parameters of cubic and tetragonal PbTiO_3	10
Table 2.3 Materials used in sol-gel synthesis method of lead titanate	14
Table 2.4 Charges on atoms and atomic displacements in cubic and tetragonal lead titanate with an oxygen vacancy (adapted from [63] with permission)	17
Table 4.1 BET Surface Areas for synthesized perovskites	37
Table 4.2 ICP measured stoichiometry of synthesized perovskites	40
Table 4.3 Amount of hydrogen consumed to reduce fresh and photodesorbed samples	42
Table 4.4 TPR peak positions of synthesized perovskites.....	45
Table 4.5 Amount of hydrogen consumed to reduce fresh and photodesorbed samples and oxygen removed from samples.....	47
Table 4.6 NO oxidation conversion over PbTiO_3 at various rates	50
Table 4.7 NO Oxidation conversion over $\text{Pb}_{0.875}\text{Co}_{0.125}\text{TiO}_3$ at various rates	51
Table 4.8 NO oxidation conversion over $\text{Pb}_{0.75}\text{Co}_{0.25}\text{TiO}_3$ at various rates	52
Table 4.9 NO oxidation conversion over $\text{Pb}_{0.5}\text{Co}_{0.5}\text{TiO}_3$ at various rates.....	53
Table 4.10 NO oxidation conversion over PbTiO_3 at various rates	54
Table 4.11 NO oxidation conversion over $\text{Pb}_{0.875}\text{Co}_{0.125}\text{TiO}_3$ at various rates.....	55
Table 4.12 NO oxidation conversion over $\text{Pb}_{0.75}\text{Co}_{0.25}\text{TiO}_3$ at various flow rates	56
Table 4.13 NO oxidation conversion over $\text{Pb}_{0.5}\text{Co}_{0.5}\text{TiO}_3$ at various flow rates.....	57
Table 4.14 UV and Visible Light Conversions of NO over PbTiO_3 at different RH	57
Table 4.15 UV and Visible Light Conversions of NO over $\text{Pb}_{0.875}\text{Co}_{0.125}\text{TiO}_3$ at different RH.....	58
Table 4.16 UV and Visible Light Conversions of NO over $\text{Pb}_{0.75}\text{Co}_{0.25}\text{TiO}_3$ at different RH.....	58
Table 4.17 UV and Visible Light Conversions of NO over $\text{Pb}_{0.5}\text{Co}_{0.5}\text{TiO}_3$ at different RH	59
Table 4.18 NO Conversions in 0% RH	60

Table 4.19 NO Conversions in 50% RH	60
Table D.1 Parameters for CSTR Assumption	86
Table D.2 Parameters for PFR Assumption	88
Table D.3 Comparison of CSTR and PFR Assumptions	89

LIST OF SYMBOLS

BET	Brunauer-Emmett-Teller
C	Concentration of reactive species, mol/L
CA	Citric Acid
CAT	Cobalt (II) Acetate Tetrahydrate
CSTR	Continuously Stirred Tank Reactor
DSC	Differential Scanning Calorimetry
F	Molar flow rate, mol/min
ICP-OES	Inductively Coupled Plasma - Optical Emission Spectrometry
k(T)	Rate Constant, min ⁻¹
LAT	Lead (II) Acetate Trihydrate
PFR	Plug Flow Reactor
RH	Relative Humidity
x	Conversion
t	Time, min
TCD	Thermal conductivity detector
TIP	Titanium (IV) Isopropoxide
TPO	Temperature programmed oxidation
TPR	Temperature programmed reduction
TPtD	Temperature programmed thermal decomposition
UV	Ultraviolet
V	Volume, L
τ	Space Time, min ⁻¹
v	Volumetric Flow rate, L/min

CHAPTER I

INTRODUCTION

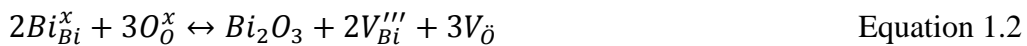
1.1 Oxygen Vacancies in Catalysis

Lately, it is realized that numerous properties of solid materials are controlled by the faults or defects in the structure. Therefore, a new discipline called defect engineering has come to exist. There are various kinds of defects in metal oxide structure. Among those defects, oxygen vacancies identify the electronic structure of the metal oxides. Generally, regular surface sites do not get involved in chemical reactions while defect sites, especially oxygen vacancies, are very reactive [1].

An oxygen vacancy is formed by detracting an oxygen atom from the structure. Formation reaction of an oxygen vacancy is shown in Equation 1.1 using Kröger-Vink Notation[2]:



The Kröger-Vink notation of the formation of oxygen vacancies in BiFeO₃ structure is shown in Equation 1.2 [3]:



It shows that oxygen vacancies can be formed by removing oxygen molecules or other molecules containing oxygen. In Equation 1.1, it is seen that when an oxygen atom in the structure is removed, a positively charged oxygen vacancy formed in structure and two electrons remain in the conduction band. In Equation 1.2, it is seen that 2 Bi atoms and 3 O atoms is removed from structure. Bi₂O₃ is formed and removed from the structure and negatively charged two bismuth vacancies and positively charged three oxygen vacancies are formed in the structure.

1.2 Methods of Creating Oxygen Vacancies

There are several methods to create oxygen vacancies in the structure such as annealing, electron-/photo-stimulated desorption, and chemical reactions with hydrogen sources[4]. Oxygen vacancies in metal oxides, especially TiO₂, has been studied comprehensively[5]–[7]. It is reported that chemical reaction of TiO₂ with hydrogen at high temperature helps to create oxygen vacancies [8]. These oxygen vacancies act like electron donors. Increase in the donor density, namely amount of oxygen vacancies, results in photocurrent enhancement which associates with the improved photoactivity in the UV region [8]. It is also reported that annealing TiO₂ under UHV conditions helps to create oxygen vacancies [5]. To create oxygen vacancies, TiO₂ is annealed at 850K for 10 minutes in UHV [9]. Another method to create oxygen vacancies in TiO₂ is told to be UV treatment by photodesorption of oxygen [6], [7]. It is thought that adsorbed oxygen molecules interact with photogenerated holes and photodesorption occurs. The proposed mechanism of photodesorption of oxygen is explained in Equation 1.3-1.6 [6].



Equation 1.3 shows the formation of electron-hole pairs by the exposure of light. It is known that to form electron hole pairs, photons with higher energies than the band gap energy of the photocatalyst is needed. An electron in the valance band can be excited by the photon and move to conduction band [10]. The positively charged holes in valance band may be captured in hole trap which is indicated as T in Equation 1.4, may recombine with the electrons that moved to conduction band as in Equation 1.5 or may interact with the adsorbed O₂ molecules and result in photodesorption of oxygen. This is schematically shown in Figure 1.1.

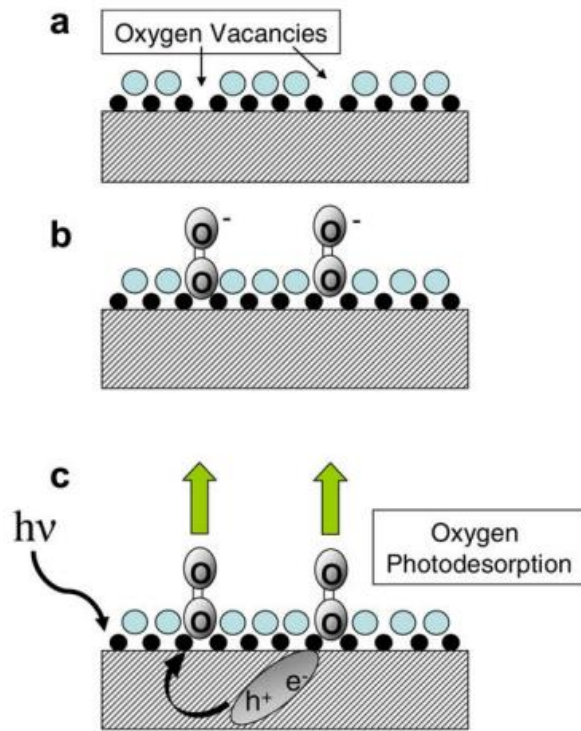


Figure 1.1 Schematic description of the oxygen photodesorption (adapted from [6] with permission)

In Figure 1.2, photodesorption and thermal desorption of oxygen from TiO₂ are compared. ¹⁸O adsorbed on Ti¹⁶O₂ surface at 105 K was desorbed by both by the help of UV irradiation and heat. It is concluded that there is no isotropic mixing between ¹⁸O adsorbed and ¹⁶O which is present in titania.

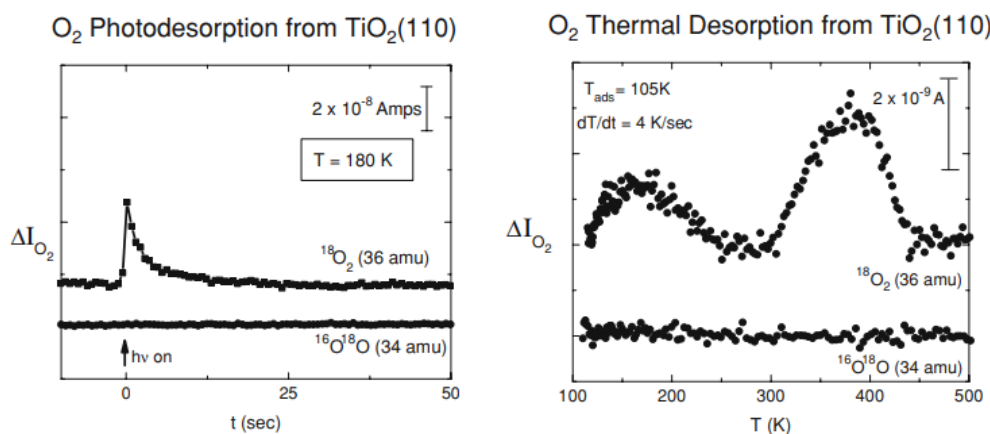


Figure 1.2 Desorption of oxygen by UV-treatment and heat treatment (adapted from [7] with permission)

In Figure 1.3, the correlation between photodesorption of oxygen and photo-oxidation of CO to CO₂ is shown. The graph on the left shows the photodesorption of O₂ from TiO₂. When TiO₂ is exposed to UV irradiation, O₂ is desorbed. As the temperature increases to 105 K to 350 K, the type of oxygen desorbed is changed from α-O₂ to β-O₂. The graph on the right indicates that photodesorbed α-O₂ can oxidize CO to CO₂.

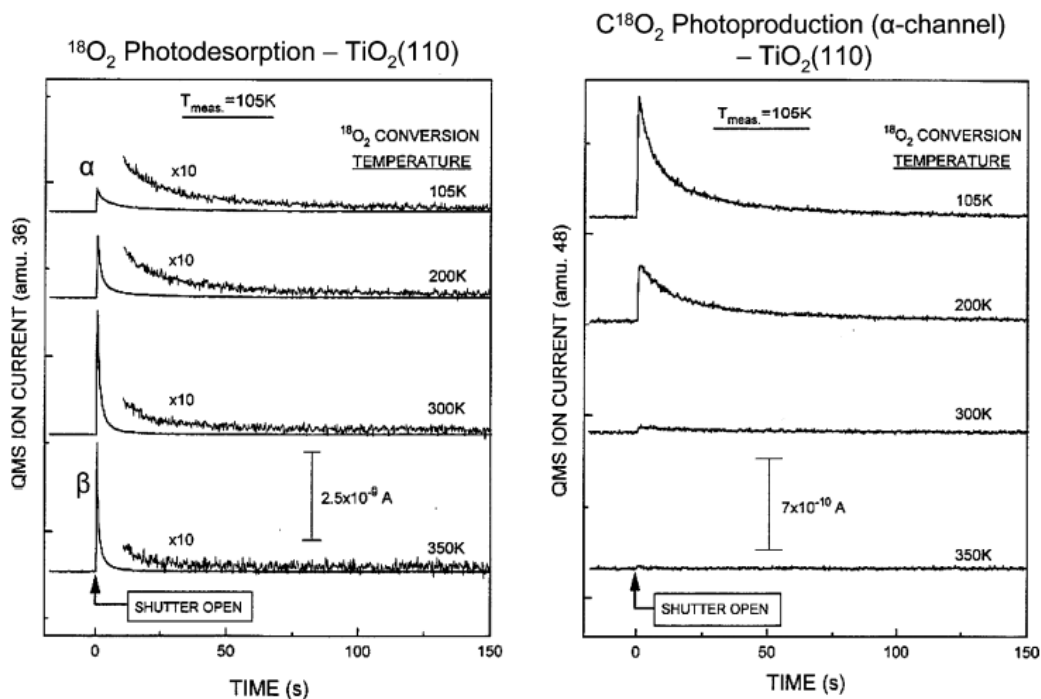


Figure 1.3 The correlation between photodesorption of oxygen and photo-oxidation of CO to CO₂ [11]

1.3 Methods of Healing Oxygen Vacancies

After creating oxygen vacancies, several molecules can be adsorbed in the vacant sites. The healing of oxygen vacancies is very important because CO₂ and H₂O can be adsorbed on vacant sites like O₂ is adsorbed. In Figure 1.1, it is shown that oxygen molecules can be adsorbed on oxygen vacancies and redesorbed. It is important because adsorbed oxygen molecules can be used as oxidizer to oxidize CO to CO₂ [6] or NO_x oxidation.

In addition, CO₂ can be adsorbed on TiO₂ [12]. It is very important because CO₂ capture is a step in artificial photosynthesis. By CO₂ reduction, hydrocarbons and

to investigate the effect of addition of cobalt atoms to lead titanate structure in oxygen vacancy formation by heat and light treatments.

In accordance with this purpose, PbTiO_3 , $\text{Pb}_{0.875}\text{Co}_{0.125}\text{TiO}_3$, $\text{Pb}_{0.75}\text{Co}_{0.25}\text{TiO}_3$ and $\text{Pb}_{0.5}\text{Co}_{0.5}\text{TiO}_3$ were synthesized by sol-gel method and oxygen adsorption-desorption of the catalysts were investigated. Temperature Programmed Reduction, photo-desorption under UV irradiation and NO photooxidation experiments were conducted.

CHAPTER II

LITERATURE REVIEW

2.1 Perovskites

Perovskite materials have the formula of ABO_3 where dodecahedral A sites can be occupied by rare earth, alkaline earth, alkali and other large ions such as Sr^{+2} , Ba^{+2} , Pb^{+2} , Ca^{+2} , La^{+2} , Na^+ , K^+ . The octahedral B sites can be occupied by 3d, 4d or 5d transitional metal ions such as Cu^{+2} , Mg^{+2} , Fe^{+3} , Ti^{+4} , Mn^{+4} [15].

Perovskites became substantial by the detection of their dielectric and ferroelectric properties in 1940s [16]. By courtesy of various properties such as superconductivity, ferromagnetism, luminescence and ionic conductivity, perovskites have been used as sensors, superconductors, light emitters, fuel cells and solar cells, are expected to be used in other fields of applications[17].

Perovskites have several physical properties shown in Table 2.1. These properties add specific characteristics to materials. The relation between ferromagnetic, magnetoelectric and ferroelectric materials was shown in Figure 2.1. Magnetoelectric and ferromagnetic materials have magnetically polarizable property and ferroelectric and magnetoelectric materials have electrically polarizable property. The materials which have both magnetically and electrically polarizable property are called multiferroic materials [18].

Ferromagnetic materials have spontaneous magnetic moments [19]. The spontaneous magnetization is temperature dependent; above the Curie temperature the material has paramagnetic property and below the Curie temperature it has ferromagnetic property, therefore, temperature has a fundamental significance in characterizing ferromagnetic materials [20]. Ferromagnetic materials are used as magnetic data-storage devices, sensors, magnetic resonance contrast media and therapeutic agents in cancer treatment[21], [22].

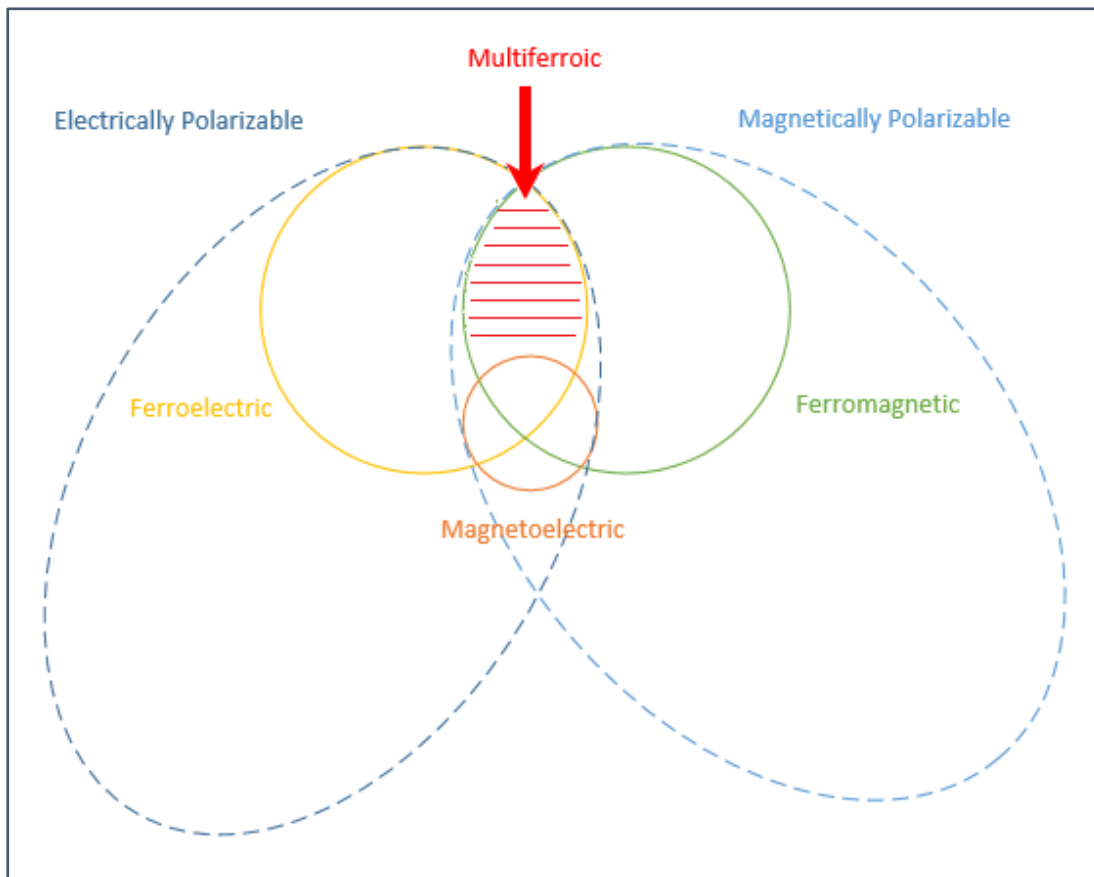


Figure 2.1 The scheme of the relationship between electrically polarizable and magnetically polarizable properties [18]

In some materials, external electric field causes magnetic moment and external magnetic field causes electric polarization. Such materials are called magnetoelectric materials [23]. Magnetoelectric materials have a potential to be used in forthcoming applications such as magnetic field sensors, transducers, actuators, microwave devices and so on [24].

Ferroelectric materials have electrically switchable spontaneous polarization property. A ferroelectric material possesses a spontaneous polarization emerging from the displacement of the center of the negative and positive charges. Ferroelectricity is a temperature dependent property. Curie temperature is a phase transition temperature and phase transformation occurs at Curie temperature between paraelectric phase and ferroelectric phase [25]. Ferroelectric materials are used as memories, radio frequency and microwave devices, pyroelectric and piezoelectric sensors and actuators [26].

Multiferroic materials have both ferroelectric and ferromagnetic properties. They exhibit a spontaneous electric polarization, magnetization [27].

Table 2.1 Properties of some perovskite oxides (adapted from [17] with permission)

Properties	Perovskite Oxides
Ferromagnetic	SrRuO, La ₂ CoMnO ₆ , ScFeO ₃ , BaRuO ₃ , BiFeO ₃ , BiMnO ₃ , BaTi _{0.85} Sn _{0.15} O ₃ , PbVO ₃ , La _{0.7} Ca _{0.3} MnO ₃
Ferroelectric	BaTiO ₃ , PbTiO ₃ , AgNbO ₃ , Y ₂ NiMnO ₆ , YMnO ₃ , TbMnO ₃ , BiFeO ₃ , BiMnO ₃ , PbVO ₃
Magnetoelectric	EuMnO ₃ , Sr ₂ CoMoO ₆ , BaTi _{0.85} Sn _{0.15} O ₃ , La _{0.7} Ca _{0.3} MnO ₃ , YMnO ₃ , TbMnO ₃
Multiferroic	BiFeO ₃ , BiMnO ₃ , PbVO ₃ , Bi ₂ CrFeO ₆

2.1.1 Lead Titanate (PbTiO₃)

Lead titanate is a perovskite material in which dodecahedral A sites are occupied by Pb⁺² ions and octahedral B sites are occupied by Ti⁺⁴ ions. Lead titanate is a yellow-tan colored powder which has a molar mass of 303.09 g/mol. Lead titanate has ferroelectric, piezoelectric and dielectric properties [28]. Piezoelectricity is defined as an electric polarization in a material resulting from the application of mechanical stress. A dielectric material is able to be polarized by an applied electric field. Lead titanate has cubic structure in paraelectric phase and tetragonal structure in ferroelectric phase as shown in Figure 2.2. Lead titanate has cubic structure at high temperatures. It is subjected to a phase transition from cubic phase to a tetragonal phase below 490°C [29], with the polarization along the [100] direction [30].

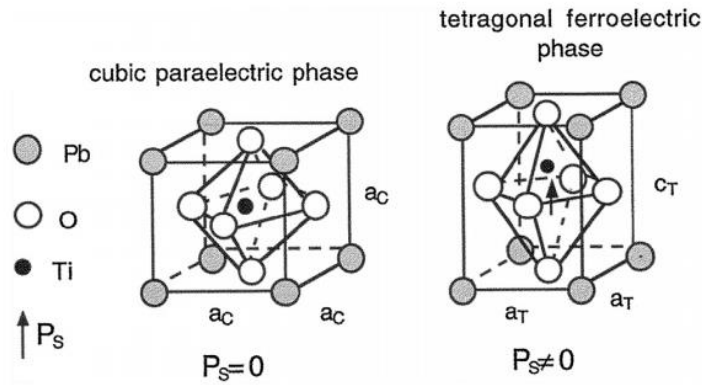


Figure 2.2 Lead titanate structure in cubic paraelectric phase and in tetragonal ferroelectric phase (adapted from [31] with permission)

Lead titanate has cubic paraelectric structure above the Curie temperature and tetragonal ferroelectric phase below the Curie temperature as shown in Figure 2.2 [31], [32],[14]. The large Pb cation is coordinated by 12 oxygen atoms cubooctahedrally, while the smaller Ti cation is coordinated to 6 oxygen atoms in an octahedral way. Lattice parameters of cubic and tetragonal PbTiO_3 were stated in Table 2.2. During from cubic to tetragonal phase transformation, O and Ti ions shift relative to Pb. In the ferroelectric phase the crystal is spontaneously strained. Lattice parameters a and b of tetragonal phase get smaller and lattice parameter c of tetragonal phase gets larger when tetragonal to cubic phase transformation occurs. Therefore, there relationship between the lattice parameters of cubic and tetragonal PbTiO_3 is $a_T \leq a_C < c_T$. The lattice distortion parameter, c/a , is important because it is an indicator of ferroelectric behavior of the crystal [31].

Table 2.2 Lattice parameters of cubic and tetragonal PbTiO_3

Cubic ($\text{Pm}\bar{3}\text{m}$, 221)			Tetragonal (P4mm , 99)			
a (Å)	3.9692 [33]	3.904 [34]	a (Å)	3.9040 [33]	3.866 [33]	3.805 [34]
c/a	1 [33]	1 [34]	c/a	1.065 [33]	1.045 [33]	1.146 [34]

2.1.1.1 Lead Titanate Applications

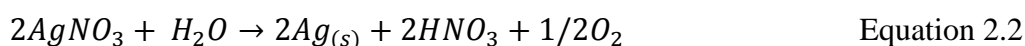
Lead titanate had been studied mostly in the USA and Japan until 1990s. There are almost 780 publications related to lead titanate until 1990. After 1990, the interest in PbTiO_3 has increased. Between 1990 and 2005, around 7800 articles were published

mostly in the USA, Japan and PRC. After 2005, the research about lead titanate has gained acceleration; after 2005, 14000 articles were published mostly in PRC, the USA and Japan. Now, almost 23000 publications related to lead titanate are available.

As the research interest increases, various application areas ensued. Until 1990s, lead titanate thin films were used in tests to produce electronic devices such as nonvolatile memory, infrared sensor, ultrasonic sensor and low-threshold electroluminescent devices [35]. Surface acoustic wave filters were fabricated using lead titanate and modified lead titanate materials [36], [37]. They made use of two properties of lead titanate: the high Curie temperature and low dielectric constant. In 2000s materials derived from lead titanate were used in underwater imaging as transducers and acoustic amplifiers, medical ultrasound devices, in actuator applications [38], [39] and as sensors [40].

Lately, lead titanate has been considered as visible a light active photocatalytic material because of its ability to absorb visible light of the solar spectrum [41]. Lead titanate is reported to have a band gap energy of 2.3 eV [42] ~2.75 eV [43], it absorbs the photons with energies greater than its band gap energy. Therefore, lead titanate can make use of visible light. The ability of making use of visible light is significant. With regards to energy, 47% of solar spectrum is composed of visible light and 3-5% of it is composed of UV-light [44]. Therefore, having a visible light active photocatalyst or photoanode is better than having a UV-light active one, such as TiO₂.

Lead titanate was used as photocatalyst for the production of H₂ and O₂ under visible light (>420 nm). To calculate the amount of H₂ formed, 1 wt% Pt/lead titanate was used and CH₃OH was used as a hole scavenger. From the amount of CO₂ generated, the amount of H₂ formed is measured which was shown in Equation 2.1 For the water photooxidation reactions, 1 wt% RuO/lead titanate was used and AgNO₃ was used as a sacrificial reagent. The amount of O₂ formed was measured by using Equation 2.2 [43].



Vertically aligned core-shell PbTiO_3 at TiO_2 heterojunction nanotube arrays were used as photoanode for photoelectrochemical water splitting and as photocatalyst for organic compound decomposition under visible light (>420 nm) [41].

Lead titanate is used in CO_2 photoreduction which is also known as artificial photosynthesis reaction. Basalt fiber core-shells coated with TiO_2 and PbTiO_3 were produced and basalt fiber core-shells coated with lead titanate showed better photocatalytic activity [45].

2.1.1.2 Synthesis Methods of Lead Titanate

2.1.1.2.1 Sol-gel Method

Sol-gel method came to light in 1960s. Sol is defined as a stable suspension of colloidal particles, which are generally nanoparticles, in a liquid and gel contains a porous, 3D continuous solid network surrounding and supporting a continuous liquid phase. Gel formation occurs by the reason of the formation of covalent bonds between sol particles [46]. Commonly, inorganic metal salts or metal organic compounds such as metal alkoxides and acetates are used as precursors to form sols by being dissolved into organic solvent such as 2-methoxyethanol. Then temperature and pH value are kept under control and concentration of alkoxides is controlled by adding water and alcohol during hydrolysis [47].

After gelation, the gel is dried and the obtained powder is calcined at a specific temperature with a specific heating rate. These processes are significant because during drying process, organic molecules are removed and calcination takes an active role in the formation the final structure of the sol-gel derived materials [47].

In sol-gel synthesis method, different kinds of precursor materials and solvents can be used. As seen in Table 2.2, lead acetate is widely-used Pb precursor. Titanium isopropoxide is the most common Ti precursor and other Ti precursors such as titanium n-butoxide, tetrabutyl titanate are used, too.

Synthesis of lead titanate by sol-gel method starts with dissolving metal precursors (Pb,Ti) in appropriate solvents. Then, the gelation is induced either by simple

reorganization of the sol or by the addition of a gelation agent. The obtained gel is dried and calcined at high temperatures. Studies about the effect of the calcination temperature on crystalline structure of lead titanate showed that crystallization starts around 400°C and single phase tetragonal lead titanate is obtained for $T_{calcination} \geq 500^\circ\text{C}$ [48][49][50].

2.1.1.2.2 Solid State Reaction

In solid state reactions, solid materials are used as starting materials and they react. It is reported that lead monoxide (PbO) and titanium dioxide (titania, TiO₂) are the starting materials for the synthesis of lead titanate by solid state reaction [43][51][52].

In 1937, by using PbO and titania as starting materials, lead titanate was synthesized. The temperature of the initial formation of lead titanate started at 360°C completed at 375°C [53]. PbO and titania were mixed by ball milling process first in isopropyl alcohol for 24 hours and dried at 120°C for 2 hours. The mixture was calcined at different temperatures and the optimum temperature was found as 600°C by XRD data [51]. To synthesize lead-modified perovskites, the same procedure is repeated by mixing starting materials by considering the final composition of the material [52].

2.1.1.2.3 Hydrothermal Synthesis

Lead nitrate and titanium butoxide are used as starting materials. Lead nitrate was dissolved in water and titanium butoxide was dissolved in ethanol and these solutions were mixed with a pH of 11.4 and 14.2 in an autoclave. The reaction takes places at a temperature range of 100-160°C with a heating rate of 3°C/min for 1-2 hours. After reaction, a PbO-TiO₂ solid solution was formed with a tabular morphology and then it was transformed into the tetragonal perovskite structure over 550°C [31], [58].

2.1.1.2.4 Other Methods

To produce lead titanate, other methods such as emulsion method, coprecipitation method, polymer precursor method, mechanochemical method are employed [31].

Table 2.3 Materials used in sol-gel synthesis method of lead titanate

Precursor Materials		Solvents
Pb Precursor	Ti Precursor	
Lead acetate trihydrate [53]	Titanium isopropoxide [53]	Methoxyethanol [53]
Lead acetate trihydrate [54]	Titanium isopropoxide [54]	Acetic Acid Glacial [54]
Lead acetate [46]	Tetrabutyl titanate [46]	Ethylene glycol monomethyl ether, cellosolve, glacial acetic acid [46]
Lead acetate [46]	Titanium n-butoxide [46]	Methoxyethanol [46]
Lead acetate trihydrate [41]	Tetrabutyl titanate [41]	Ethanol [41]
Lead acetate trihydrate [49]	Titanium(IV) tertbutoxide [49]	Acetic acid glacial, 1-butanol [49]
Lead acetate trihydrate [55]	Titanium n-butoxide [55]	Ethanol [55]
Lead acetate trihydrate [56]	Titanium isopropoxide [56]	Methoxyethanol [56]

2.1.1.3 Oxygen Vacancy Formation in Lead Titanate

It is known that defects, specifically lattice vacancies, have a great impact on the performance of lead titanate which is a ferroelectric material. Lead titanate lattice has defects such as Pb vacancies, oxygen vacancies. In oxygen rich environment Pb vacancies are stable and in oxygen poor environments oxygen vacancies are stable [59], [60].

Oxygen vacancy studies have been done both experimentally and computationally. Oxygen vacancies are important for several reasons: Firstly, lead-derived titanate materials in the form of thin film have been widely used in ferroelectric random access memories and lattice vacancies results in fatigue problem in ferroelectric RAMs [59]. However, having oxygen vacancies in metal oxides and perovskites which are used as photocatalyst is preferred. Because it plays a crucial role in photocatalytic activity. The electrons trapped on oxygen vacancies are thought to be firmly related to the photocatalytic oxidation of NO under visible light irradiation [61]. In addition, lead titanate doped with some ions such as lithium showed a better photocatalytic activity due to the Ti^{+3} ions and oxygen vacancy formation [62].

Oxygen vacancy formation studies have mostly done using density functional theory (DFT) calculations and other computational methods. Both cubic and tetragonal lead titanate structures were studied using a quantum chemical method [63].

It is seen in Figure 2.3 that, when an oxygen atom which is negatively charged is removed from the cubic crystal, the vacancy becomes positively charged. According to study, oxygen atoms and lead atoms head towards to the vacancy, whereas, titanium atoms steer away from the vacancy [63].

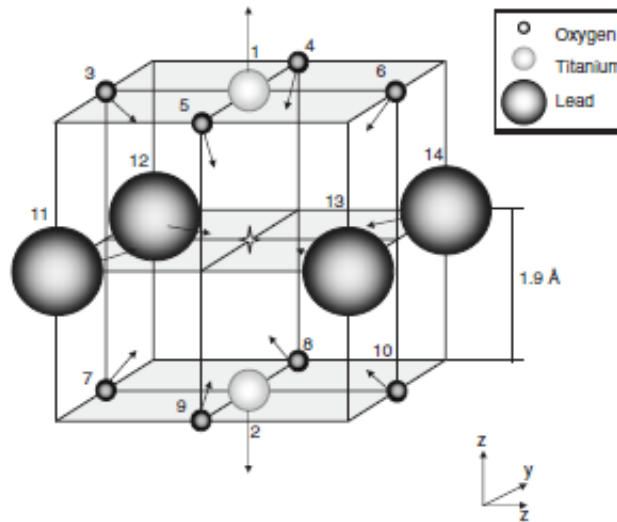


Figure 2.3 The cubic PbTiO_3 crystal with an oxygen vacancy (adapted from [63] with permission)

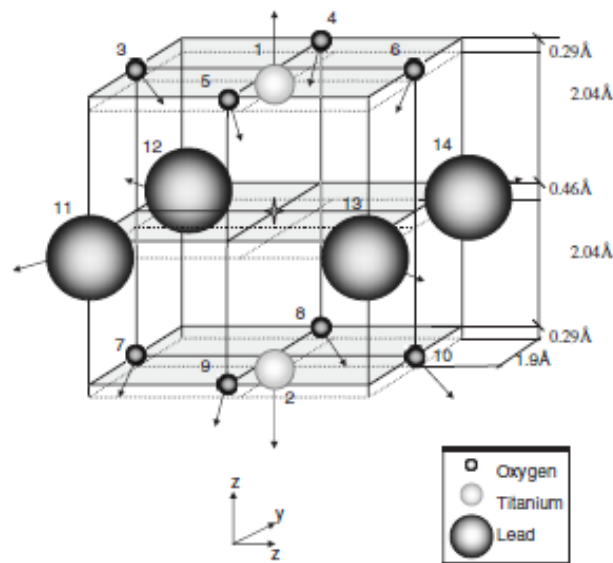


Figure 2.4 The tetragonal PbTiO_3 crystal with an oxygen vacancy in dimerized Ti–O–Ti chains (adapted from [63] with permission)

For tetragonal lead titanate, upper titanium atom which is numbered as 1 is closer to oxygen vacancy than the lower one which is number as 2 as seen in Figure 2.4. Therefore, they are repelled by the vacancy stronger than lower titanium atoms. According to Coulomb law, upper oxygen atoms head towards oxygen vacancy while the lower oxygen atoms steer away. Lead atoms move away from the vacancy. The

charges on each atom, the new charges and the displacement after removing an oxygen atom are tabulated in Table 2.4. It is stated that the structural, electronic and optical properties are changed by the displacement of atoms and change in charges [63]. Therefore, having oxygen vacancies may affect the interactions between lead titanate and other chemicals.

Table 2.4 Charges on atoms and atomic displacements in cubic and tetragonal lead titanate with an oxygen vacancy (adapted from [63] with permission)

Atoms	Cubic lead titanate			Tetragonal lead titanate		
	Charge (e)		Displacement (Å)	Charge (e)		Displacement (Å)
	Perfect Crystal	With Vacancy		Perfect Crystal	With Vacancy	
Ti (1)	2.48	2.38	0.17	2.37	2.26	0.53
Ti (2)	2.48	2.38	0.17	2.40	2.29	0.06
O (3)	-1.39	-1.38	0.14	-1.32	-1.30	0.21
O (4)	-1.39	-1.38	0.14	-1.32	-1.30	0.21
O (5)	-1.39	-1.38	0.14	-1.32	-1.30	0.21
O (6)	-1.39	-1.38	0.14	-1.32	-1.30	0.21
O (7)	-1.39	-1.38	0.14	-1.38	-1.36	0.23
O (8)	-1.39	-1.38	0.14	-1.38	-1.36	0.23
O (9)	-1.39	-1.38	0.14	-1.38	-1.36	0.23
O (10)	-1.39	-1.38	0.14	-1.38	-1.36	0.23
Pb (11)	1.70	1.71	0.07	1.74	1.69	0.03
Pb (12)	1.70	1.71	0.07	1.74	1.69	0.03
Pb (13)	1.70	1.71	0.07	1.74	1.69	0.03
Pb (14)	1.70	1.71	0.07	1.74	1.69	0.03

The formation energies of Pb, Ti and O vacancies are reported as: $V_{Ti} > V_O > V_{Pb}$. Computational methods illustrate the structure of the cubic and tetragonal lead titanate before and after an oxygen vacancy is formed and formation energies of V_{Ti}, V_O, V_{Pb} [64].

Experimental methods are also reported where oxygen vacancies are deliberately introduced to observe the effect of oxygen vacancies in photo-activity. It is reported that some methods such as doping, noble metal deposition, surface sensitization and coupling of two semiconductors help to improve photo-activity. Li doped PbTiO_3 showed a better photoactivity due to the formation of Ti^{3+} and oxygen vacancies in the structure while degrading methylene blue [62].

In addition, room temperature photoluminescence measurement of lead titanate single crystalline nanowires synthesized by hydrothermal method shows a blue-green light emission peaking at about 471 nm and two weak emission bands increasing excitation wavelength results in the increase in the intensity of the main emission peak. This emission was attributed to the oxygen vacancies [65].

In an experimental study, heat treatment for two hours under a hydrogen atmosphere was performed on lead titanate thin films to create oxygen vacancies. The oxygen vacancies were observed after the heat treatment by analyzing the photoluminescence spectra of lead titanate thin films before and after heat treatment at 700°C . For heat-treated sample, photoluminescence peak position shifts from 560 to 570 nm due to the fact that the emission related to the oxygen vacancies becomes dominant. Also, Raman spectroscopy studies were done. The intensity of the additional phonon mode increases with the increasing heat treatment temperature when the wavelength of the excitation laser was fixed at 568.2 nm, which is the resonant condition for oxygen vacancies. Therefore, it is found that when heat-treatment temperature increases, x in PbTiO_{3-x} gets larger, namely, the amount of oxygen vacancies increases [66].

To crosscheck the results, after the heat treatment, re-oxidation is done to fill in the oxygen vacancies with oxygen in PbTiO_3 thin films. Raman spectroscopy study showed that the intensity of the additional phonon mode increases with the increasing heat treatment in a reducing environment. After re-oxidizing, the intensity of the additional phonon mode becomes similar with the initial intensity of the additional phonon mode [67].

2.1.1.4 The Photocatalytic NO Oxidation over Lead Titanate

The photocatalytic NO oxidation was studied over photocatalysts such as TiO_2 , SrTiO_3 , BaTiO_3 , PbTiO_3 and noble metal doped TiO_2 , $\text{V}_2\text{O}_5/\text{TiO}_2$ and CeO_2 [68],[69],[70]–

[75]. It is reported that the oxygen vacancies of TiO_2 can cause the absorption of visible light and therefore, the separation of electron- hole pairs is provided [71]. Also, it is indicated that NO can be oxidized and NO_3^{3-} accumulate on the surface and NO_3^{3-} removal percentage is proportional to the electrons trapped in oxygen vacancies [61]. NO oxidation over TiO_2 under UV-irradiation is shown in Figure 2.5 [75]. The sharp decrease around 35th minute observed upon UV illumination and is due to the oxidation of NO already adsorbed on the surface before illumination is provided. Afterwards, NO concentration increases and a steady value is reached [75].

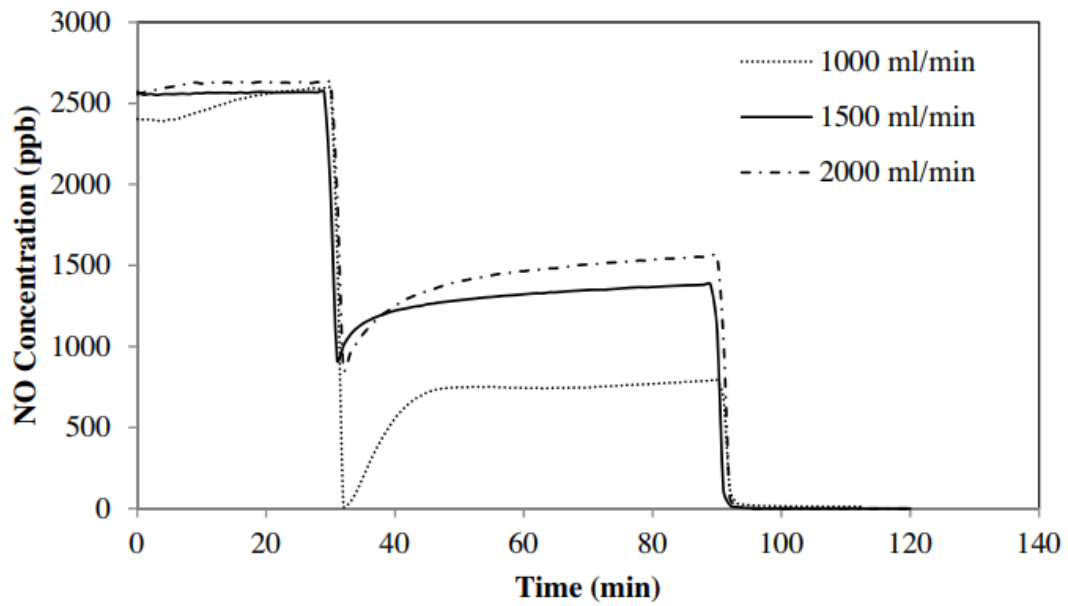
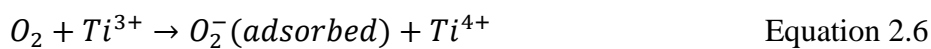
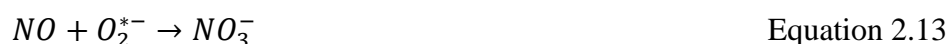
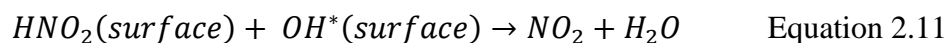
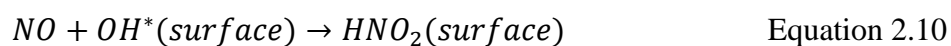


Figure 2.5 Effect of total flow rate on photocatalytic activity of TiO_2 (adapted from [75] with permission)

The NO oxidation mechanism under UV light irradiation is given as [75]:





Equation 2.7- Equation 2.9 show that water adsorbed on the surface results in the formation of OH groups on the surface. Equation 2.10 shows that NO can be oxidized effectively by the help of surface OH groups. Therefore, the effect of relative humidity is important in photocatalytic NO oxidation. Uner et al. showed that as relative humidity in air increases, NO conversion over TiO₂ increases in Figure 2.6.

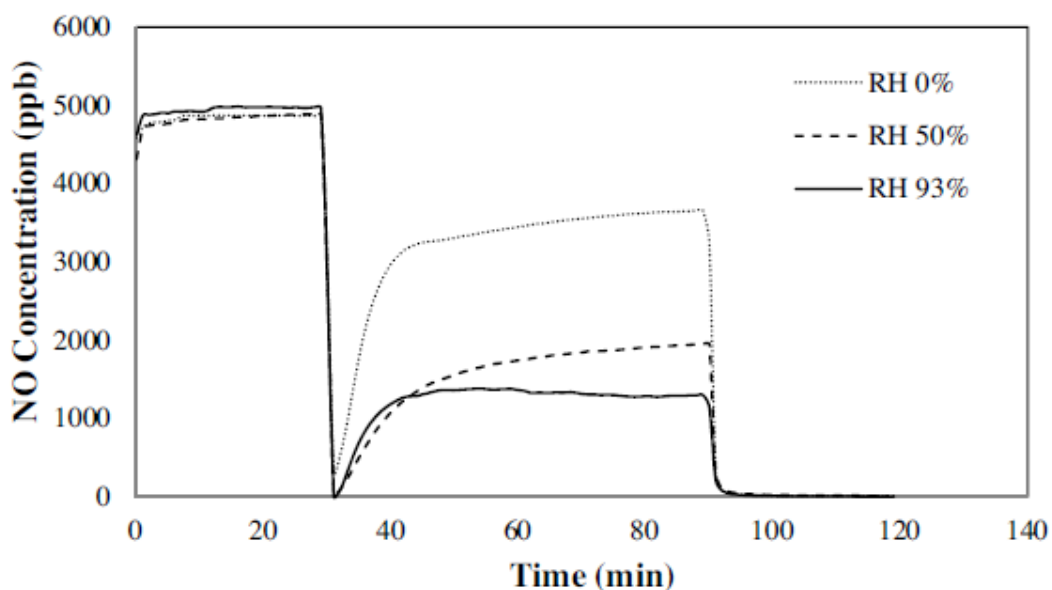


Figure 2.6 The effect of relative humidity on the photocatalytic NO oxidation over TiO₂ (adapted from [75] with permission)

In Figure 2.5, the effect of total flow rate on photocatalytic activity is shown. Titania load was 0.36 g, the light intensity was 18.8 W/m² and relative humidity was 50

percent. First 30 minutes, 2500 ppb NO was fed to reactor and then the reactor was exposed to UV-irradiation for 1 hour. After 1 hour of UV-irradiation, zero calibration gas was fed to the system. It is indicated that the sharp decrease around 30 minutes is due to the oxidation of NO molecules that had adsorbed on the active sites. Then an increase in NO concentration and then a steady NO concentration profile is observed [75].

Photocatalytic NO oxidation of some perovskites was conducted under full spectrum and visible light irradiation ($\lambda > 420\text{nm}$). A 150 W metal halide lamp was used as light source with the light intensity of 51.3 mW/cm^2 on the surface of the catalyst, the amount of catalysts was 60 mg and flow rate of NO and air was 1.51 L/min. The concentration of NO was 700 ppb [74].

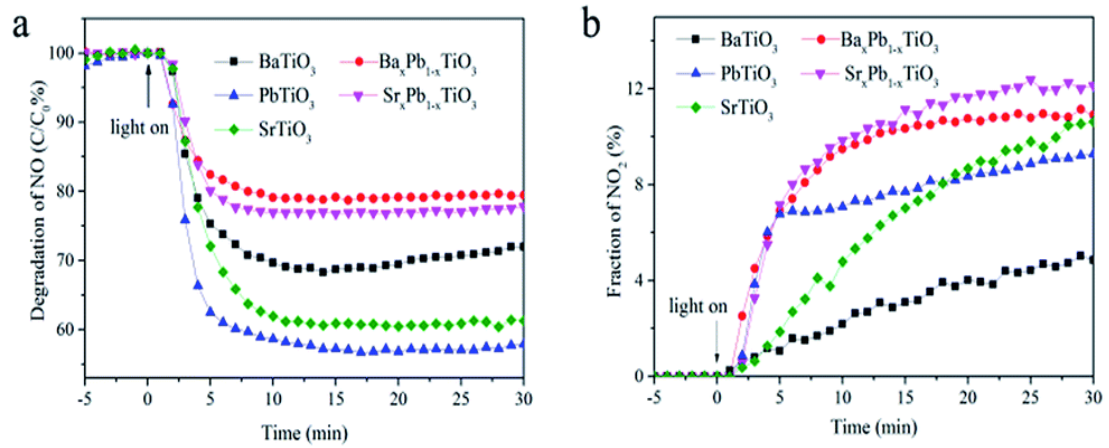


Figure 2.7 Change in the concentrations of NO (a) and NO₂ (b) during photocatalytic oxidation (adapted from [74] with permission)

In Figure 2.7a, the change in the concentration of NO when the system was exposed to visible light irradiation is shown. Lead titanate has the highest NO removal efficiency which was described in Equation 2.14 [74]:

$$\eta_{NO \text{ removal}} = \left(1 - \frac{C_{NO}}{C_{0NO}}\right) \times 100 \quad \text{Equation 2.14}$$

In Figure 2.7b, the fraction of NO₂ produced is shown. From the experiment NO₂ generation is the lowest for BaTiO₃ which means that more NO₃⁻³ is generated which is the desired product. The ratio of NO₂ generation is described in Equation 2.15 [74]:

$$\eta_{NO_2} = \frac{C_{NO_x} - C_{NO} - (C_{0NO_x} - C_{0NO})}{C_{NO_x}} \times 100 \quad \text{Equation 2.15}$$

From Figure 2.7 it can be concluded that lead titanate shows the best photocatalytic activity under visible light irradiation to oxidize NO. However, barium titanate promotes the generation of NO_3^{3-} more than the other perovskites.

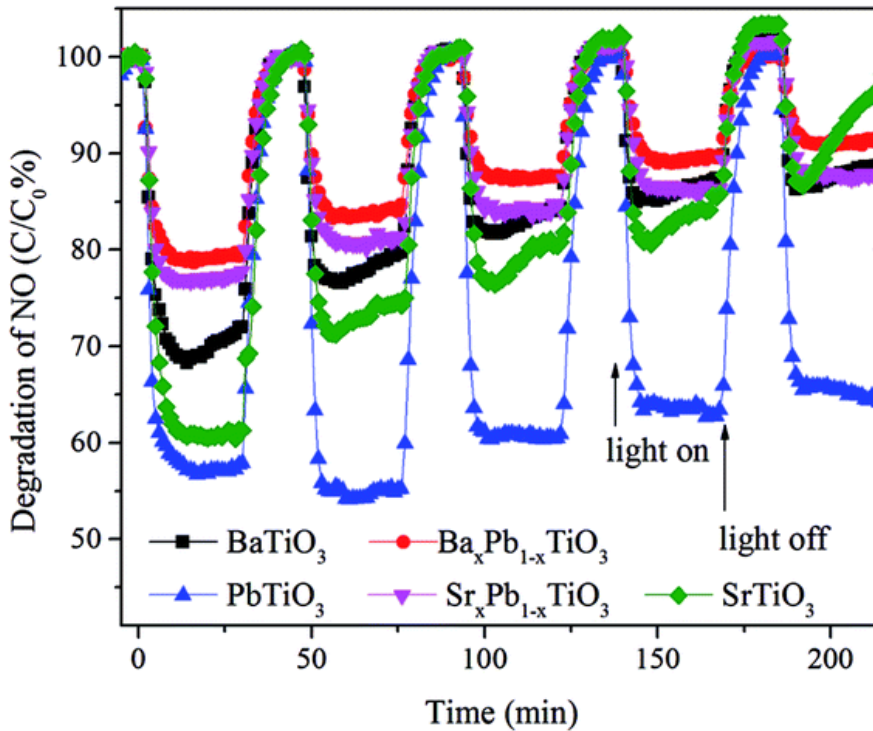


Figure 2.8 Dark-light cyclic experiments over perovskite structures under full spectrum (adapted from [74] with permission)

To see the reusability of perovskite structures, recycling experiments were conducted. Figure 2.8 shows the recycling experiments of NO oxidation. It is seen that lead titanate can oxidize NO better than other catalysts under full spectrum irradiation. Lead titanate can remove 43% of NO while $SrTiO_3$ can remove 40% and $BaTiO_3$ can remove 30% of NO for the first cycle. Photocatalytic activity of $SrTiO_3$ and $BaTiO_3$ is decreased sharply in the second cycle. However, there is no sharp decrease in the photocatalytic activity of lead titanate during five cycles.

Another study made by Hailili et al. showed that layered perovskite $\text{Pb}_2\text{Bi}_4\text{Ti}_5\text{O}_{18}$ showed a good NO oxidation activity under visible light. They used 50 mg of samples which was coated on a glass dish placed in the middle of the reactor. The initial concentration of NO was 500 ppb and the gas flow rate was 1 L/min [76]. Nanoparticle are nanosphere shaped perovskites showed a better photocatalytic activity than rectangular and nanosheet shaped perovskites as seen in Figure 2.9. While nanosphere shaped perovskite converts 50% of NO, rectangular shaped one converts 20% of NO.

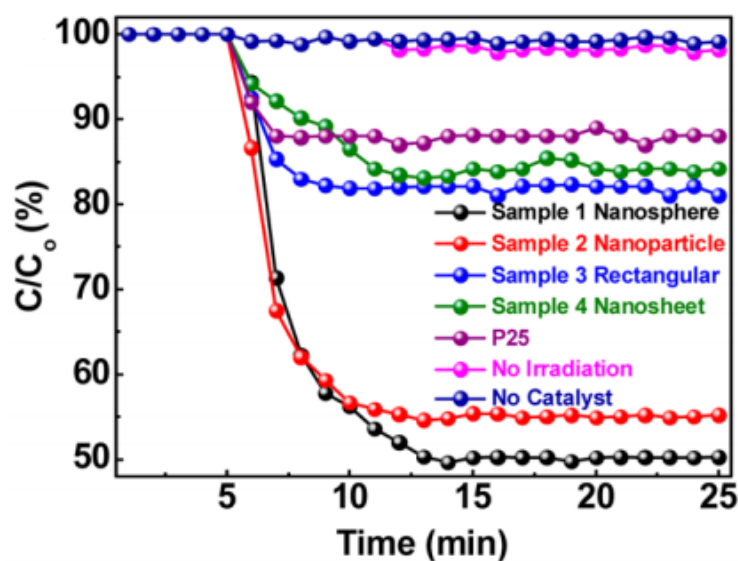


Figure 2.9 Photocatalytic NO Oxidation $\text{Pb}_2\text{Bi}_4\text{Ti}_5\text{O}_{18}$ showed over with various nanoscale morphologies under visible light (adapted from [76] by permission)

Different kinds of perovskites were studied by Zhang et al. for their visible light activity on NO Oxidation. They used 100 mg of samples which were spread on a glass holder and placed inside of a flow reactor. The initial NO concentration was 400 ppb and gas flow rate was 3L/min [77]. Figure 2. 1 shows the photocatalytic NO oxidation activity of SrTiO_3 and LaFeO_3 under visible light.

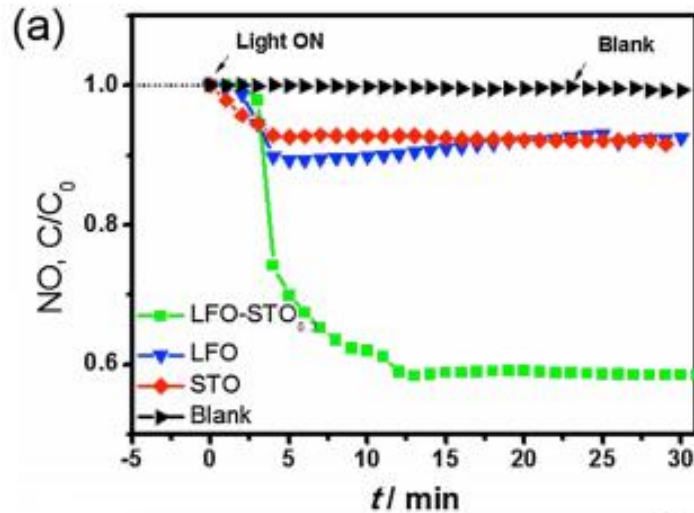


Figure 2.10 Photocatalytic NO Oxidation over SrTiO₃ and LaFeO₃ under visible light (adapted from [77] with permission)

2.1.1.5 Doping lead titanate by other atoms

Substitution of cations at A and B sites of perovskites has been studied lately [78], [79]. Some examples can be seen in Table 2.1. B site of BaTi_{0.85}Sn_{0.15}O₃ is occupied by titanium and stannum ions. A site of La_{0.7}Ca_{0.3}MnO₃ is occupied by lanthanum and calcium ions. Doping A and B sites of perovskites causes the change in piezoelectricity, Curie temperature, band gap, lattice parameters.

2.1.1.5.1 Doping A site of Lead Titanate

Lead titanate is modified by doping cations at A site such as Pb_xLa_{1-x}TiO₃ [80][81][82], Pb_{x1}La_{x2}Ca_{1-x1-x2}TiO₃ [83], Pb_xLa_{1-x}TiO₃ [81], Pb_{1-x}Sr_xTiO₃[84]. The sol-gel method [74] [75], spray pyrolysis [82], solid-state reaction [84] are used to synthesize this kind of modified perovskite structures. King et al. reported that doping Ca atoms at A site of lead titanate changes the lattice parameters. *c/a* ratio decreases when some of the Pb atoms replaced by the smaller Ca atoms[79]. Ikegami indicated that addition of La and Mn atoms in A site of lead titanate provides low dielectric constant, high thickness coupling factor, high mechanical quality factor, high stability, and high operating temperature [85].

2.1.1.5.2 Doping B site of Lead Titanate

Doping B site of lead titanate by Zr atoms have been widely studied [78], [83], [86], [87]. Cho et al. indicates that $\text{Pb}(\text{Ni}_{1/3}\text{Nb}_{2/3})\text{O}_3\text{-PbZrO}_3\text{-PbTiO}_3$, in which Pb atoms exist in A site and Ni, Zr, Nb and Ti atoms exist in B site randomly, has great piezoelectric properties [86]. Kumar et al. added Bi^{3+} and Fe^{3+} at A and Bi sites of lead titanate and reported an increase in the Curie temperature. However, addition of Fe^{3+} at only B site results in a decrease in the Curie temperature [87] Also to narrow the band gap, Ni atoms can be doped at the B site of lead titanate. Zhou et al. reported that doping Ni at the B site results in lattice expansion and it introduces oxygen vacancies [88]. Sun et al. found out that doping Al atoms in B site of lead titanate results in increased tetragonality, namely, stronger spontaneous polararization. Unlike Al doping on B site, Zr doping results in decreased tetragonality [89].

CHAPTER III

MATERIALS AND METHODS

3.1 Materials

In order to synthesize lead-based perovskites, Lead (II) Acetate Trihydrate (extra pure, MERCK), Titanium (IV) Isopropoxide (97%, Sigma-Aldrich), Cobalt (II) Acetate Tetrahydrate (pure, MERCK), Citric Acid (99%, Aldrich) were used. Acetic acid glacial and ethanol are used as solvents in synthesis. In NO oxidation experiments, NO (100 ppm in N₂, Linde) and air are used. In TPx experiments H₂ (10 vol% in Ar, Linde), and He (pure, Linde) gases are used.

3.2 Synthesis Method

3.2.1 Synthesis of PbTiO₃ by Sol-Gel Method

Lead (II) Acetate Trihydrate (extra pure, MERCK) was used as lead precursor and Titanium (IV) Isopropoxide (97%, Sigma-Aldrich) was used as titanium precursor. Citric acid (99%, Aldrich) was used as gelation agent. Acetic acid is used to dissolve LAT and 50 volume % mixture of ethanol-acetic and acid glacial was used to dissolve TIP and ethanol is used to dissolve citric acid. Chemical structures of metal precursors and solvents are shown in Figure 3.1.

LAT was dissolved in the minimum amount of acetic acid glacial. TIP was dissolved in the minimum amount of 50 volume % mixture of acetic acid glacial and ethyl alcohol. CA was dissolved in ethanol. The molar ratio of LAT, TIP and CA was (1:1:2), respectively.

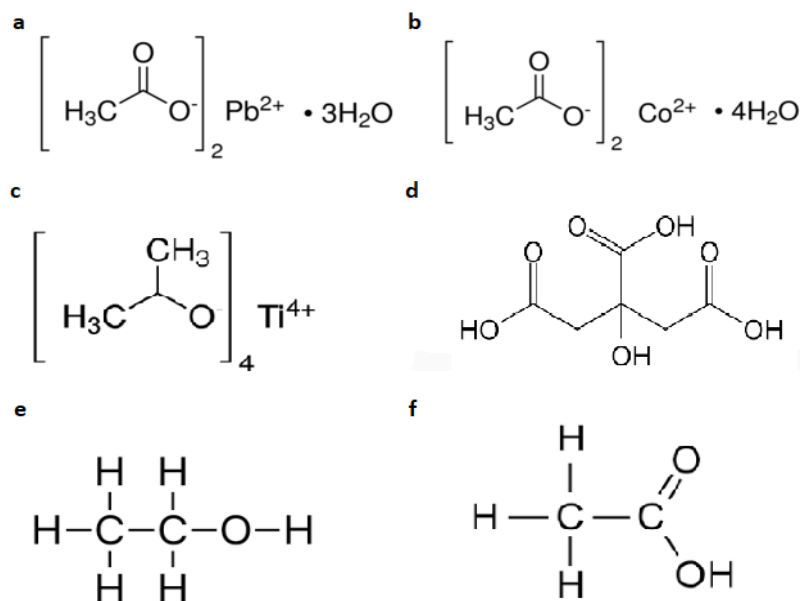


Figure 3.1 Chemical structures (a: Lead (II) Acetate Trihydrate, b: Cobalt (II) Acetate Tetrahydrate, c: Titanium (IV) Isopropoxide, d: Citric Acid e: Ethanol, f: Acetic Acid Glacial)

After dissolution, the solution that contains TIP was added to the solution that contains LAT. New solution that contains TIP and LAT was kept under vigorous stirring seen in Appendix A. Then, CA- ethanol solution was added to the solution that contains TIP and LAT. As soon as CA-ethanol solution was introduced, a white gel was formed. The gel was kept under vigorous stirring and later it was transferred on the hot plate. A white solidified gel was obtained which can be seen in Appendix A.

Afterwards, the white solidified gel was placed in the oven and it stayed there overnight at 100°C to remove volatile organic solvents and water that the gel contained. The white powder obtained next day was calcined in furnace with the rate of 5°C /min at 650°C for 3 hours. After calcination, a yellow powder was obtained.

3.2.2 Synthesis of $\text{Pb}_x\text{Co}_{1-x}\text{TiO}_3$ by Sol-Gel Method

Lead (II) Acetate Trihydrate (extra pure, MERCK) was used as lead precursor and Titanium (IV) Isopropoxide (97%, Sigma-Aldrich) was used as titanium precursor and Cobalt (II) Acetate Tetrahydrate (pure, MERCK) was used as cobalt precursor. LAT was dissolved in the minimum amount of acetic acid glacial and CAT was dissolved

in the LAT- acetic acid solution. TIP was dissolved in the minimum amount of 50 volume % mixture of acetic acid glacial and ethyl alcohol. Citric acid (99%, Aldrich) was dissolved in ethanol. The molar ratio of LAT, CAT, TIP and CA was (x:1-x:1:2), respectively (where $x \leq 1$).

After dissolution, the solution that contains TIP was added to the solution that contains LAT and CAT. New solution that contains TIP, LAT and CAT was kept under vigorous stirring seen in Appendix A. Then, CA- ethanol solution was added to the solution that contains TIP, CAT and LAT. As soon as CA-ethanol solution was introduced, a pink gel was formed. The gel was kept under vigorous stirring and later it was transferred on the hot plate. A pink solidified gel was obtained which can be seen in Appendix A.

Afterwards, the pink solidified gel was placed in the oven and it stayed there overnight at 100°C to remove volatile organic solvents and water. The pink powder obtained next day was calcined in furnace with the rate of 5°C /min at 650°C for 3 hours. After calcination, a gray powder was obtained for $x = 0.875$, a green powder was obtained for $x = 0.75$ and a green powder was obtained for $x = 0.5$

3.3 Characterization Methods

3.3.1 XRD Analysis

XRD analysis was used to determine phase identification and the crystallinity of PbTiO_3 and $\text{Pb}_x\text{Co}_{1-x}\text{TiO}_3$ samples. Analyses were performed in Philips PW 1840 Compact X-ray Diffractometer equipment (-30kV, 24mA- with Cu $K\alpha$ radiation). The scattering angle was from 5 to 90°.

3.3.2 UV-Vis Spectroscopy

UV-Vis spectroscopy analysis was done in Shimadzu UV-2450 equipment. The absorbance data was measured between 200 nm and 800 nm. Barium sulfate was used as reference sample.

3.3.3 BET Analysis

Surface area evaluation was done by using Micromeritics TriStar II Surface Area and Porosity equipment under nitrogen flow. To remove the moisture and adsorbed gases on the surface of synthesized perovskites, they were degassed for 4 hours at 120°C by using Micromeritics Vac Prep 061 Sample Degas System.

3.3.4 DSC Analysis

The Curie temperatures of the samples were found by using DSC analysis. Samples were enclosed in metal capsules and heated to 550°C with a rate of 10°C/min. The peak in the heat flow versus temperature data gives the Curie temperature of the perovskite samples.

3.3.5 ICP Analysis

The compositions of synthesized perovskites are analyzed by using Perkin Elmer Optima 4300DV equipment. Inductively coupled plasma - optical emission spectrometry is used to determine the compositions.

3.4 NO Oxidation Experiments

3.4.1 Coating Method

First of all, a slurry was prepared with powder catalysts (PbTiO_3 , $\text{Pb}_{0.875}\text{Co}_{0.125}\text{TiO}_3$, $\text{Pb}_{0.75}\text{Co}_{0.25}\text{TiO}_3$, $\text{Pb}_{0.5}\text{Co}_{0.5}\text{TiO}_3$) and distilled water. Then the slurry was spread on flat glasses by the help of a glass rod. After the coating on the flat glass is dried under ambient conditions, it was placed in oven above 100°C to get rid of the moisture. Figure 3.2 shows the coated films on flat glasses.

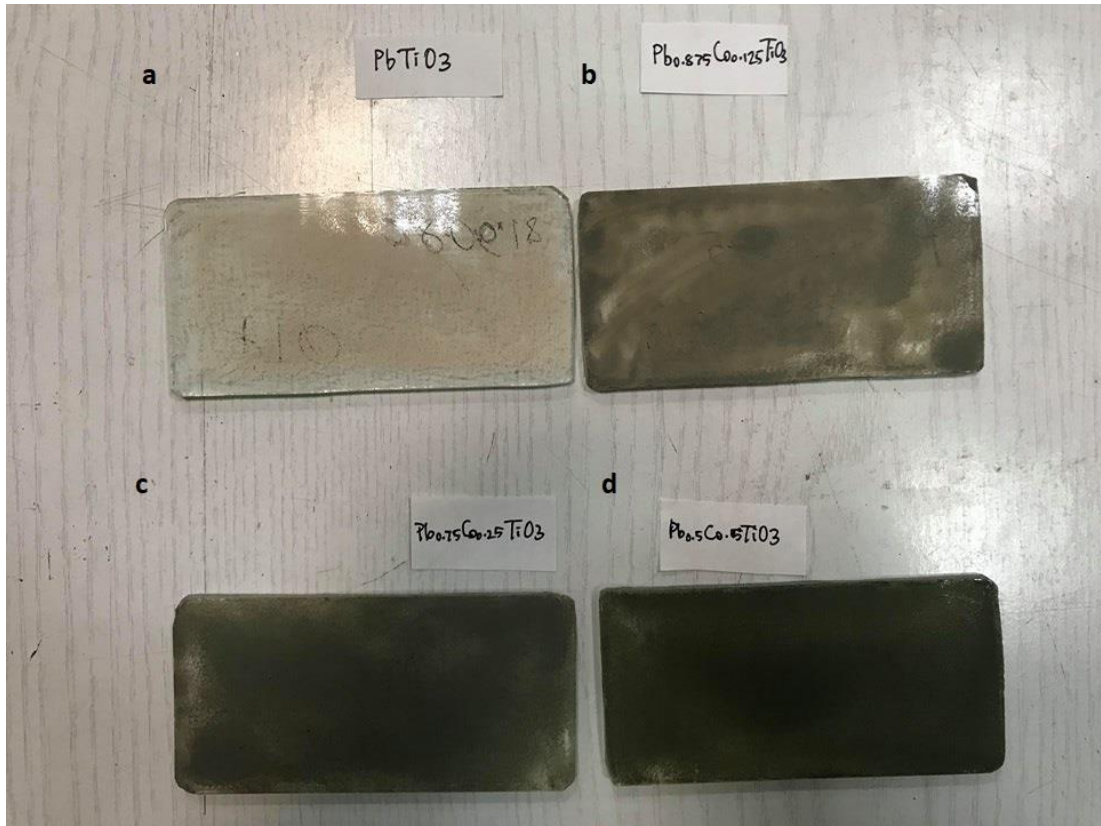
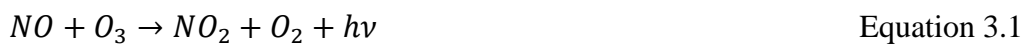


Figure 3.2 Coated samples on flat glass (a: PbTiO_3 , b: $\text{Pb}_{0.875}\text{Co}_{0.125}\text{TiO}_3$, c: $\text{Pb}_{0.75}\text{Co}_{0.25}\text{TiO}_3$, d: $\text{Pb}_{0.5}\text{Co}_{0.5}\text{TiO}_3$)

3.4.2 NO Oxidation Experimental Set up

NO oxidation experiments are based on ISO-22197:2007(E). The experimental set up consists of Thermo Fisher Scientific Model 42i NO_x analyzer, reactor, gas cylinders, humidifier, mass flow controllers and UV lamp. A schematic drawing of the experimental set up is depicted in Figure 3.3. NO_x analyzer has a chemiluminescent detector which measures a characteristic luminescence with an intensity linearly proportional to the NO concentration. The luminescence is produced by the reaction of nitric oxide (NO) and ozone. The reaction is seen in Equation 3.1.



The analyzer has two modes: NO mode where NO concentration is measured and NO_x mode where NO_x concentration is measured. In NO_x mode, NO₂ is converted to NO by the help of a molybdenum NO₂-to-NO converter which is heated to 325°C. NO_x

analyzer cannot measure NO_2 concentration directly but the difference between NO and NO_x concentration gives NO_2 concentration.

A longwave UV lamp with a peak emission at 365 nm and is used to activate the photocatalysts that was coated on flat glasses. By the help of mass flow controllers (Teledyne, HFC 202), the fraction of NO and relative humidity are adjusted. The dimensions of the flow reactor which is machined from Plexiglas with a quartz window. The picture of the reactor is shown in Appendix B, Figure B1. The lamps providing UV and the visible light irradiation were placed 24 cm above the reactor. The intensity of the light on the surface of the catalyst was measured as 18 mW/cm^2 for UV irradiation and 27 mW/cm^2 for visible light irradiation, by an oriel PV reference cell system (Newport: Model 91150V).

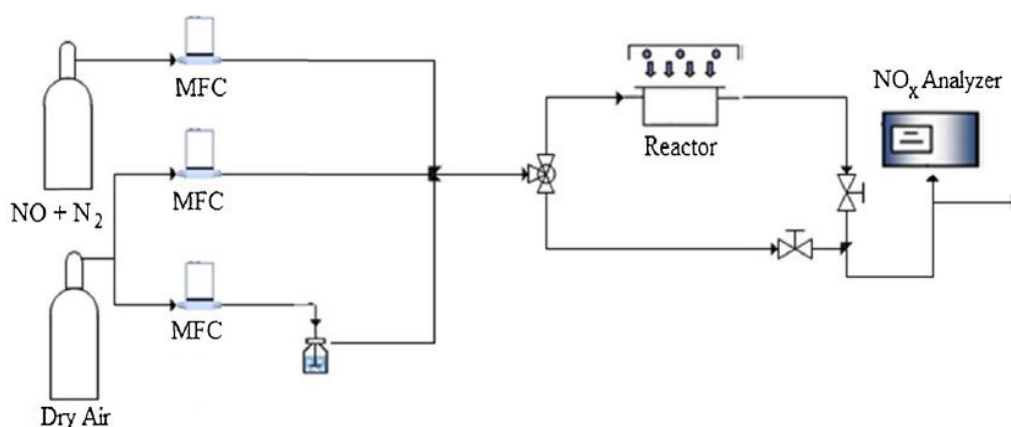


Figure 3.3 Experimental set up for NO oxidation over photocatalysts (adapted from [75] with permission)

3.4.3 NO Oxidation Experimental Procedure

The experiments were conducted according to ISO-22197:2007(E) standard. There are four steps while doing NO Oxidation experiments. Detailed experimental procedure is given in Appendix C.

Oxidation under UV: In this step, photocatalyst is exposed to UV irradiation under air flow to oxidize the combustible organic or inorganic contaminants present on the surface.

Stabilization of NO flow: After UV-exposition, the flow of the gases was switched to the flow of a gas mixture with pre-adjusted composition of NO, humidity and air without UV-irradiation. Prior to sending the gases to the reactor, the gas mixture was bypassed to the NO_x analyzer for the measurement of the inlet gas composition.

Photocatalytic NO Oxidation: After the NO flow in the reactor is stabilized, the reactor is exposed to UV-irradiation and the product gases were monitored in the NO_x analyzer.

Shut down: The shutdown starts by switching off the UV lamp, the reactive gases were bypassed and NO_x was turned off, then the reactor was flushed with pure air. After air flow is stopped, the top cover of the reactor can be removed to replace the sample.

3.5 TP_x Analysis

Micromeritics Chemisorb 2720 equipment was used for TP_x analyses. Temperature programmed reduction (TPR), temperature programmed thermal decomposition (TPtD), temperature programmed oxidation (TPO) photodesorption experiments were conducted to measure the reducibility of samples before and after UV and heat treatments.

The equipment utilizes the flowing gas technique of analysis, namely, the amount of gas adsorbed by the sample which is placed in a U-shaped quartz reactor is tracked by a thermal conductivity detector (TCD). The temperature where adsorption or desorption occurs is monitored. Reaction and carries gases are used to allow both physical and chemical adsorption.

Before letting the gas flow through the system, the samples are placed between quartz wool in the U-shaped quartz reactor and the quartz reactor is placed in a furnace which can be heated up to 1100°C. The top of the furnace is covered by an isolation material to minimize the heat loss from the furnace to environment. Cold trap is installed to condense water vapor during the experiments in which water is formed, for example TPR experiment. In cold trap, a mixture of ice, water and isopropyl alcohol are used as coolant. The final temperature, heating rate and stand by time at final temperature are fixed using TP_x controller.

While starting all experiments, He flows into by-pass and short path. After the stabilization of TCD signal, He flows through long path and sample to purge the air

from the system. Then gas flow is changed to 10% H₂-Ar for TPR and it is not changed for UV-desorption experiments. Detailed procedure is given in Appendix C.

3.6 Adsorption Measurements and Adsorption Calorimetry

Water adsorption isotherms over all of the samples were determined under static conditions. Furthermore, over two different samples, differential heats of adsorption were also measured by adsorption calorimetry.

Heat of H₂O adsorption on synthesized perovskites were studied in a Pyrex glass manifold. In this equipment, a calorimeter (Setaram C-80 TianCalvet) is connected to the multiport high vacuum Pyrex glass manifold. To vacuum the manifold, a turbo molecular pump station (Pfeiffer TCP 015, Pfeiffer TMH 065) is used. The pressure in the manifold is monitored by a pressure gauge (MKS Baratron Capacitance Manometer) and a digital power supply (MKS PR4000B).

First, the manifold was evacuated and both sample cell and reference cell were placed into calorimeter ports. Then the sample was heated to 100°C and treated by oxygen for an hour. The system was cooled down to 50°C and H₂O at different pressures (1 torr to 25 torr) was dosed to the sample.

CHAPTER IV

RESULTS

4.1 XRD Analysis

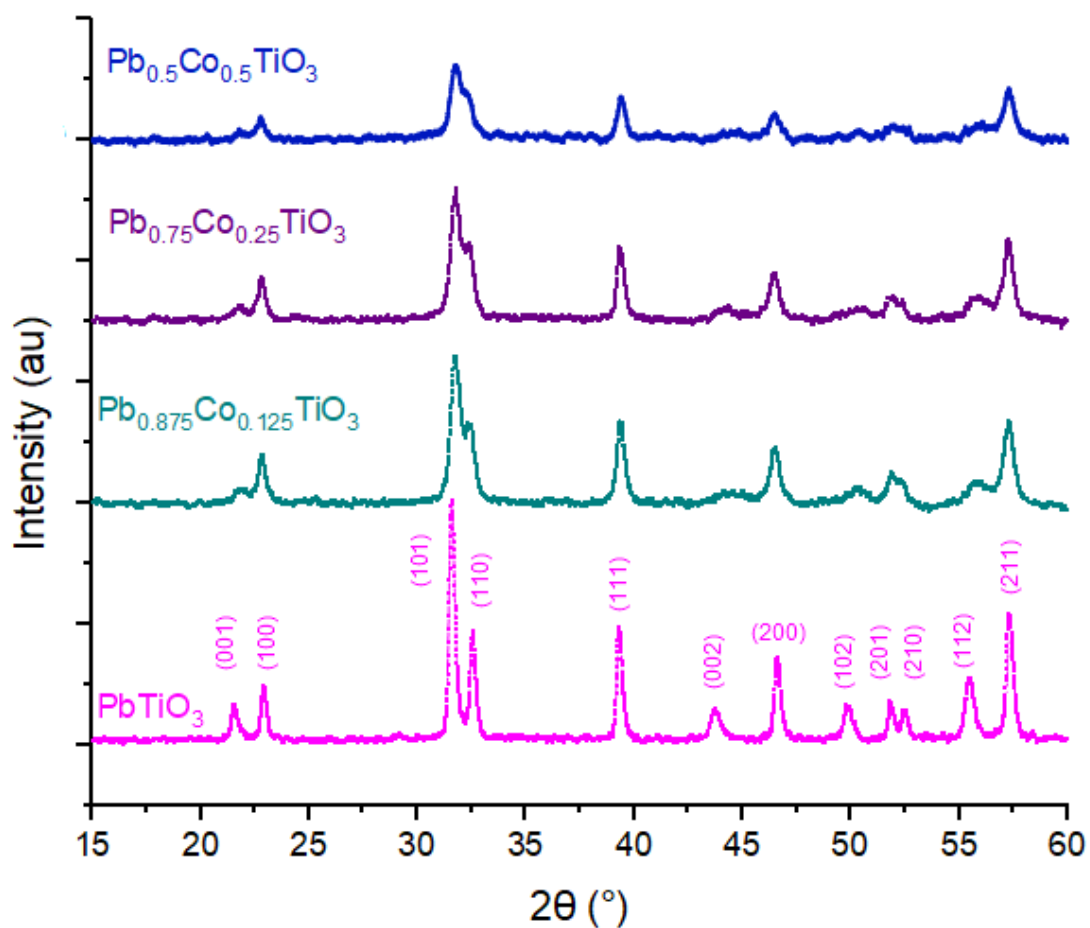


Figure 4.1 XRD patterns of PbTiO_3 , $\text{Pb}_{0.875}\text{Co}_{0.125}\text{TiO}_3$, $\text{Pb}_{0.75}\text{Co}_{0.25}\text{TiO}_3$, $\text{Pb}_{0.5}\text{Co}_{0.5}\text{TiO}_3$

Synthesized samples of PbTiO_3 , $\text{Pb}_{0.875}\text{Co}_{0.125}\text{TiO}_3$, $\text{Pb}_{0.75}\text{Co}_{0.25}\text{TiO}_3$, $\text{Pb}_{0.5}\text{Co}_{0.5}\text{TiO}_3$ were analyzed using XRD analysis. The results were compared with the literature which was reported by Yang et al. [90]. For PbTiO_3 synthesized by sol-gel method,

characteristic peaks were seen in Figure 4.1. Upon Co addition, the peaks corresponding to (101) and (110), (201) and (210), (112) and (211) broaden and merge. In addition, as cobalt content increased, intensity of the peaks decreased. These facts were interpreted to be due to the decrease of the crystal size as cobalt content increased.

4.2 UV-Vis Analysis

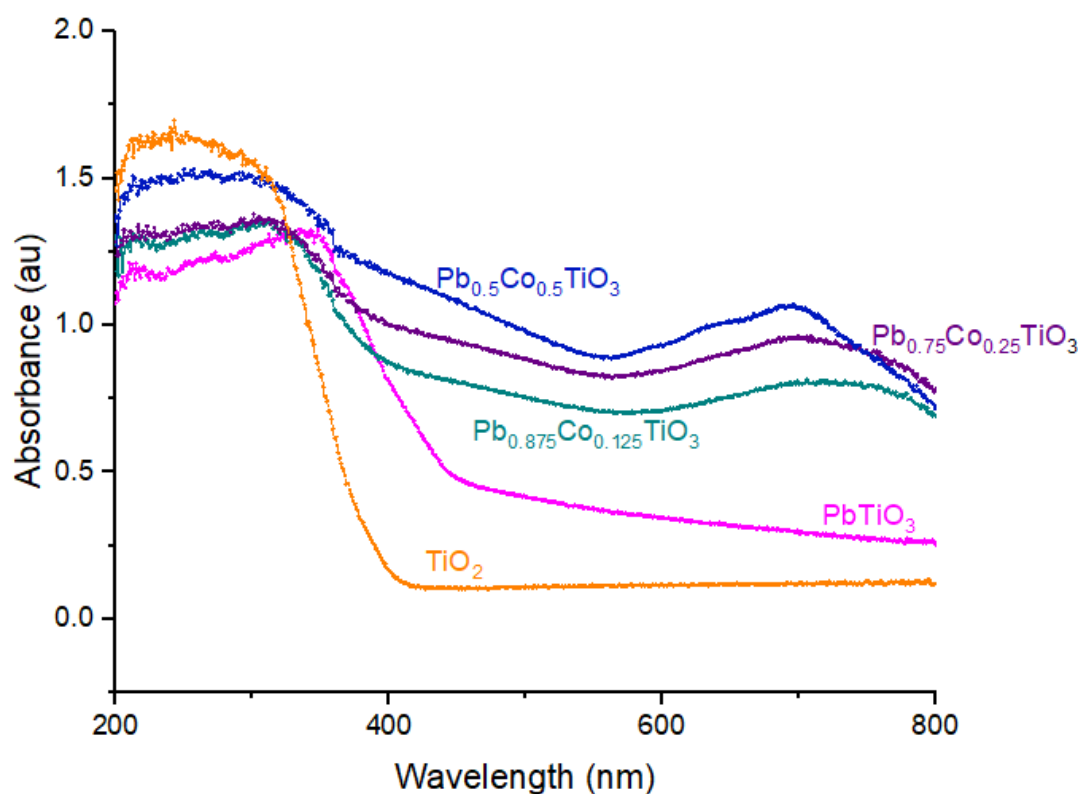


Figure 4.2 UV-Visible Diffuse Reflectance Spectra of PbTiO_3 , $\text{Pb}_{0.875}\text{Co}_{0.125}\text{TiO}_3$, $\text{Pb}_{0.75}\text{Co}_{0.25}\text{TiO}_3$, $\text{Pb}_{0.5}\text{Co}_{0.5}\text{TiO}_3$

In Figure 4.2, UV-visible diffuse reflectance spectra showed that all synthesized perovskites and TiO_2 had strong absorption between 200 nm - 400 nm. This behavior can be originated from Ti^{+4} that all samples have. For PbTiO_3 , absorption edge is larger than the absorption edge of TiO_2 . The result conforms with the literature [91], [92]. The peak around 650nm - 800 nm for Co-doped samples was originated from Co^{+4} species. Zhang et al. and Dai et al. showed that Co_3O_4 and $\text{Co}_3\text{O}_4/\text{TiO}_2$ had similar absorption spectra between 600-800 nm while for pure TiO_2 , there are no peaks in this

region [93], [92]. Band gap of TiO_2 and PbTiO_3 was calculated as 3.1 eV and 2.5 eV, respectively and as cobalt content increased the band gap decreased.

4.3 BET Analysis

The BET surface areas of the perovskites are given in Table 4.1.

Table 4.1 BET Surface Areas for synthesized perovskites

Perovskites	BET Surface Area (m^2/g)
PbTiO_3	1.9
$\text{Pb}_{0.875}\text{Co}_{0.125}\text{TiO}_3$	10.3
$\text{Pb}_{0.75}\text{Co}_{0.25}\text{TiO}_3$	12.3
$\text{Pb}_{0.5}\text{Co}_{0.5}\text{TiO}_3$	20.1

Table 4.1 shows that as cobalt content increased BET surface area of the perovskites increased. Since there was no mesopores detected in both samples BET surface areas could be correlated with the crystal size. XRD results showed that crystal size increased with increasing cobalt content. BET result supported this.

4.4 DSC Analysis

To see the effect of Co doping on the Curie temperature of PbTiO_3 , DSC analysis conducted. The Curie temperature of PbTiO_3 was found as 489.75°C which conforms with the literature. Figure 4.3 indicates that, the phase transformation of PbTiO_3 happened around 490°C . Co-doped samples have no peaks between $100\text{-}550^\circ\text{C}$. It means that phase transformation is not detected between those temperatures.

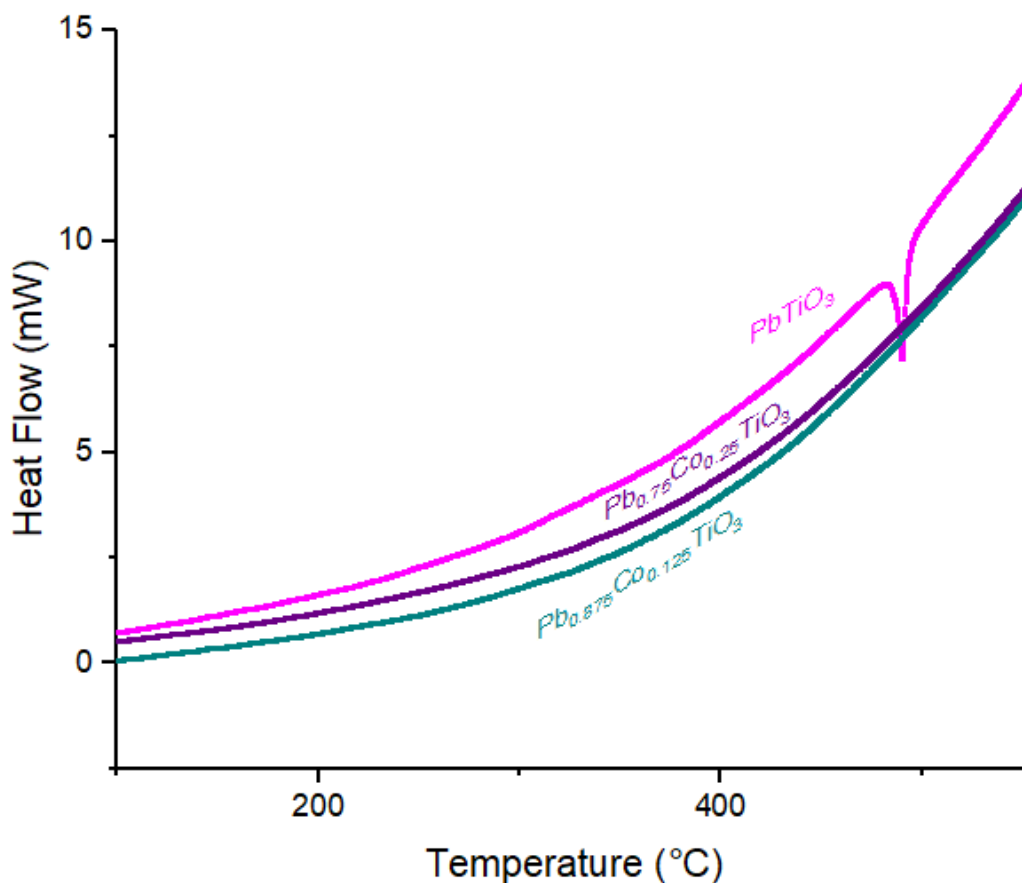


Figure 4.3 DSC curve of $PbTiO_3$, $Pb_{0.875}Co_{0.125}TiO_3$ and $Pb_{0.75}Co_{0.25}TiO_3$

4.5 ICP- OES Analysis

The composition of synthesized perovskites were determined by using ICP-OES analysis. Table 4.2 shows the mass percent and molar percents of Pb, Co, Ti and O atoms in the samples. The mass percentages of Pb, Co and Ti in synthesized samples are obtained from ICP-OES analysis and the remaining mass is assumed to be O.

ICP- OES analysis shows that for $PbTiO_3$, Pb/Ti molar ratio is 1.1. For $Pb_{0.875}Co_{0.125}TiO_3$, Pb/Co molar ratio is 7.2 and (Pb+Co)/Ti molar ratio is 1.1. For $Pb_{0.75}Co_{0.25}TiO_3$, Pb/Co molar ratio is 3.1 and (Pb+Co)/Ti molar ratio is 1.1. For $Pb_{0.5}Co_{0.5}TiO_3$, Pb/Co molar ratio is 1.0 and (Pb+Co)/Ti molar ratio is 1.1. The expected Pb/Co molar ratios are 7, 3 and 1 for $Pb_{0.875}Co_{0.125}TiO_3$, $Pb_{0.75}Co_{0.25}TiO_3$, $Pb_{0.5}Co_{0.5}TiO_3$, respectively. The expected (Pb+Co)/Ti molar ratios are 1 for all perovskites. ICP Measured stoichiometries are found as $Pb_{1.07}Ti_{0.69}$,

$\text{Pb}_{0.98}\text{Co}_{0.13}\text{TiO}_{2.50}$, $\text{Pb}_{0.84}\text{Co}_{0.27}\text{TiO}_{2.66}$, $\text{Pb}_{0.55}\text{Co}_{0.53}\text{TiO}_{2.71}$ for PbTiO_3 , $\text{Pb}_{0.875}\text{Co}_{0.125}\text{TiO}_3$, $\text{Pb}_{0.75}\text{Co}_{0.25}\text{TiO}_3$, $\text{Pb}_{0.5}\text{Co}_{0.5}\text{TiO}_3$, respectively. Oxygen stoichiometries are found to be lower than the expected value.

4.6 TP_x Analyses

4.6.1 TRP of TiO₂ before and after UV-irradiation exposure

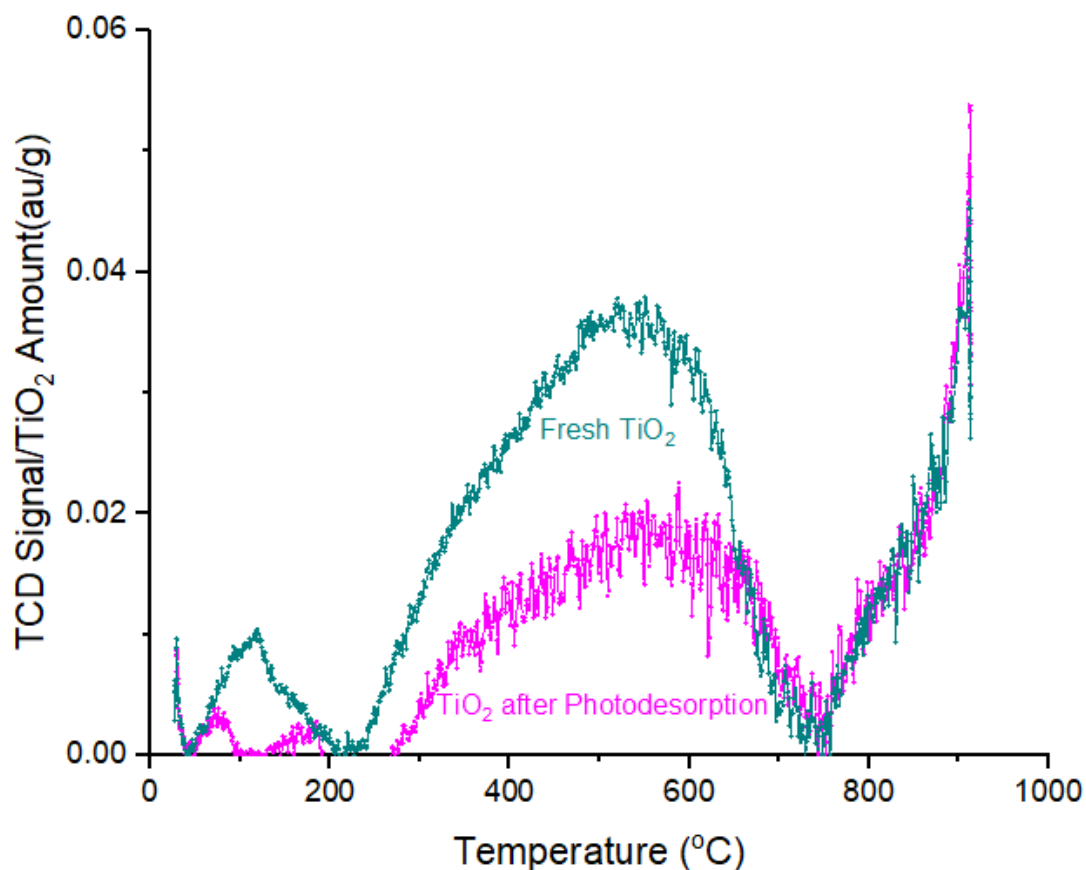


Figure 4.4 TPR profile of TiO₂ after and before photodesorption

First TPR profile of fresh TiO₂ is obtained under a flow of 25 ml/min H₂ (%10 vol.) in Ar, with a heating rate of 5°C/min. Secondly, a fresh TiO₂ sample is exposed to UV irradiation for 2 hours under a flow of 25 ml/min He and followed by a TPR experiment identical to the previous case. In Figure 4.4, for fresh TiO₂, there is a peak around 125°C while there are two smaller peaks around 60°C and 181°C for UV treated sample. Also the broad peak between 200°C and 700°C is larger for fresh TiO₂ and UV treated TiO₂. The amount of hydrogen consumed during the TPR experiments is shown in Table 4.3 and all samples were quantified against AgO TPR measurement.

Table 4.2 ICP measured stoichiometry of synthesized perovskites

Samples	Mass Percentage (%)				Molar Percentage (%)				ICP Measured Stoichiometry
	Pb	Co	Ti	O	Pb	Co	Ti	O	
PbTiO ₃	71 ± 1	-	15.3 ± 0.1	13.7	0.343	-	0.320	0.86	Pb _{1.07} TiO _{2.69}
Pb _{0.875} Co _{0.125} TiO ₃	68 ± 1	2.67 ± 0.02	16.0 ± 0.1	13.3	0.328	0.045	0.334	0.83	Pb _{0.98} Co _{0.13} TiO _{2.50}
Pb _{0.75} Co _{0.25} TiO ₃	62 ± 1	5.72 ± 0.01	17.1 ± 0.2	15.2	0.299	0.097	0.357	0.95	Pb _{0.84} Co _{0.27} TiO _{2.66}
Pb _{0.5} Co _{0.5} TiO ₃	48 ± 1	13.3 ± 0.1	20.3 ± 0.2	18.4	0.232	0.226	0.424	1.15	Pb _{0.55} Co _{0.53} TiO _{2.71}

4.6.2 TPR of 0.5 wt% Pt/TiO₂ before and after UV-irradiation exposure

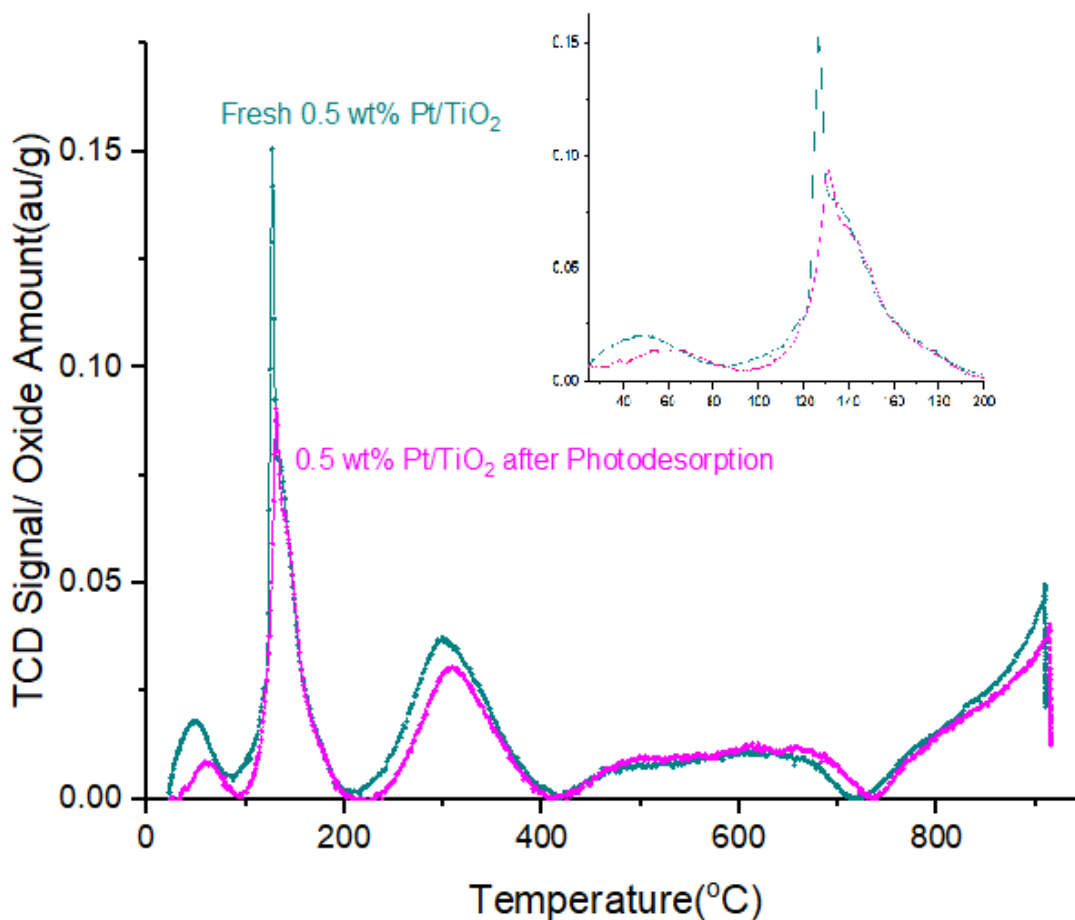


Figure 4.5 TPR profile of 0.5 wt% Pt/TiO₂ after and before photodesorption

For 0.5 wt% Pt/TiO₂, TPR experiments are conducted to reduce the samples and compare the amount of hydrogen used to reduce fresh and UV treated samples. The amount of reduction supplied by UV treatment was determined from the difference between the hydrogen consumed by fresh sample and UV treated sample. The amount of hydrogen consumed, shown in Figure 4.5, indicates that, the amount of hydrogen consumed to reduce fresh 0.5 wt% Pt/TiO₂ is more than UV treated 0.5 wt% Pt/TiO₂ samples. It can be explained as energy band theory. When the sample is UV treated, the electrons in valance band are excited and reduce Pt oxide species. The second and third peak around 130°C is related to reduction of Pt oxide species and the peak around 310°C is related to the reduction of surface particles [94]. When the sample is UV

treated, it had been already reduced by the electrons spring from valance band of TiO₂. Therefore, hydrogen consumed is less for reduction of UV-treated sample.

Table 4.3 Amount of hydrogen consumed to reduce fresh and photodesorbed samples

	Pt/TiO ₂			TiO ₂		
	H ₂ consump., mol/g _{oxide}	H ₂ consump, mol/mol _{TiO₂}	% Ti in reduced form	H ₂ consump., mol/g _{oxide}	H ₂ consump., mol/mol _{TiO₂}	% Ti in reduced form
Dark	2.54x10 ⁻⁴	2.03x10 ⁻²	1.010	1.86x10 ⁻⁴	1.49x10 ⁻²	0.743
After UV	2.07x10 ⁻⁴	1.65x10 ⁻²	0.827	1.52x10 ⁻⁴	1.21x10 ⁻²	0.607
Diff.	4.70x10 ⁻⁵	3.75x10 ⁻³	0.188	3.40x10 ⁻⁵	2.72x10 ⁻³	0.136

4.6.3 TPR of lead titanate before and after UV-irradiation exposure

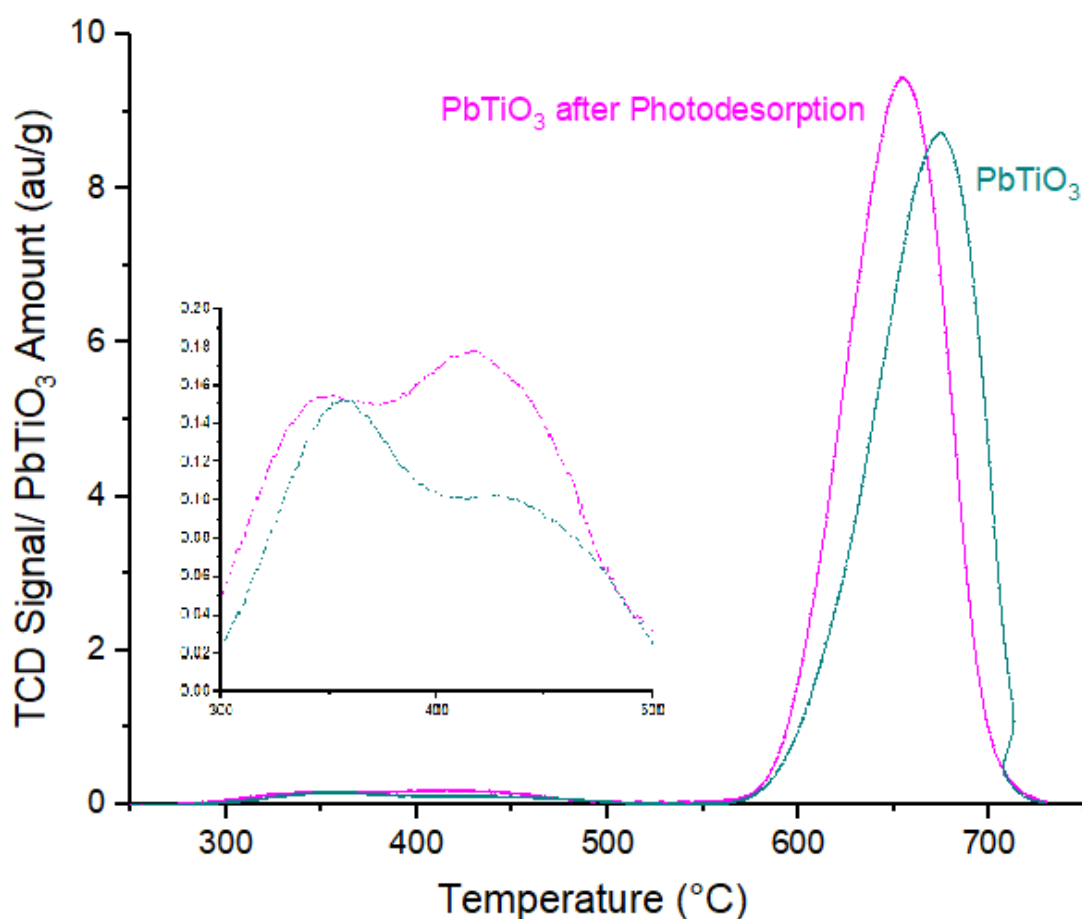


Figure 4.6 TPR profile of PbTiO₃ before and after photodesorption

The experimental procedure implemented from the TiO₂ - TPR and UV desorption experiments. However, heating rate in TPR experiments were 10°C/min for all

synthesized perovskites. In Figure 4.6, it is seen that more hydrogen is consumed after the lead titanate sample was exposed to UV-irradiation. However, it can be reduced at lower temperature. The TRP peak for fresh lead titanate is at 675°C, whereas the peak for UV treated sample is at 655°C.

4.6.4 TPR of $\text{Pb}_{0.875}\text{Co}_{0.125}\text{TiO}_3$ before and after UV-irradiation exposure

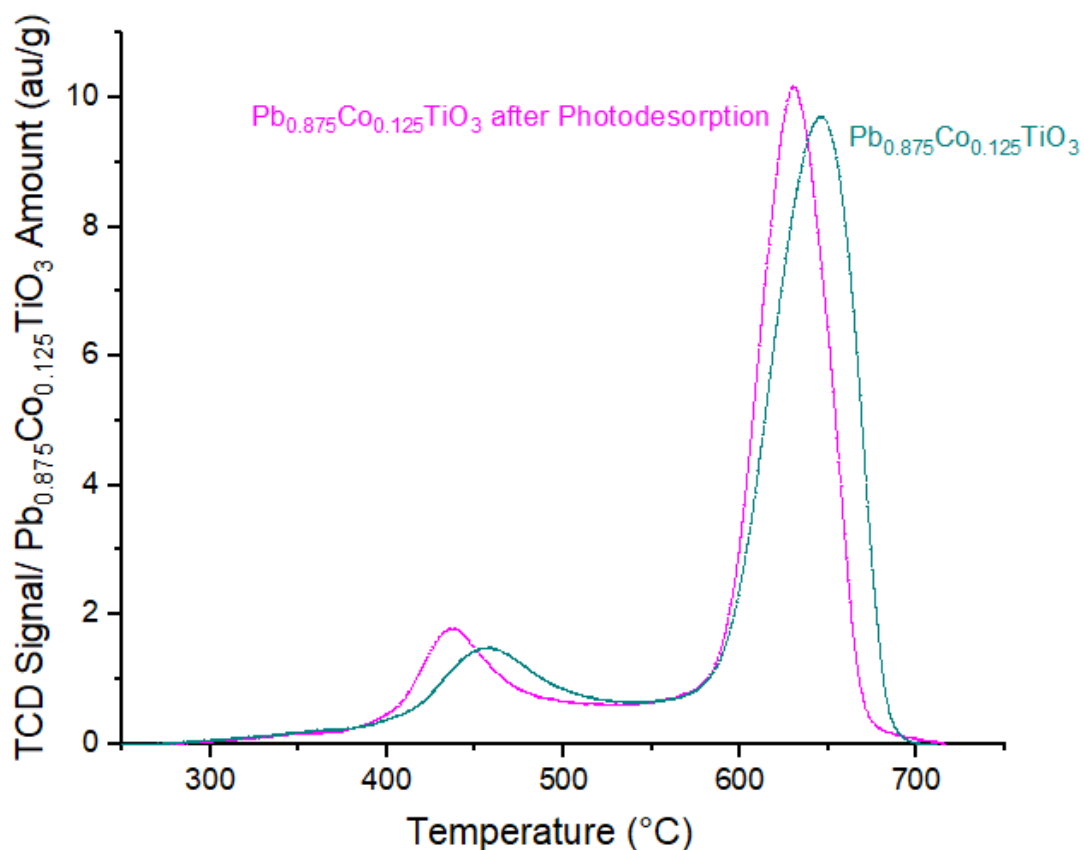


Figure 4.7 TPR profile of $\text{Pb}_{0.875}\text{Co}_{0.125}\text{TiO}_3$ before and after photodesorption

Figure 4.7 shows that there are two peaks for $\text{Pb}_{0.875}\text{Co}_{0.125}\text{TiO}_3$ before and after photodesorption. For UV treated sample the first and second peaks are at 437°C and 631°C, respectively. However, for fresh sample the first and second peaks are at 455°C and 646°C, respectively. It means that UV treated sample can be reduced at lower temperatures. On the other hand, hydrogen consumed to reduce UV-treated sample is more than hydrogen consumed to reduce fresh sample. Photodesorption and TPR after photodesorption experiments were conducted twice for this sample and result is given in Appendix E, Figure E.1.

4.6.5 TPR of $\text{Pb}_{0.75}\text{Co}_{0.25}\text{TiO}_3$ before and after UV-irradiation exposure

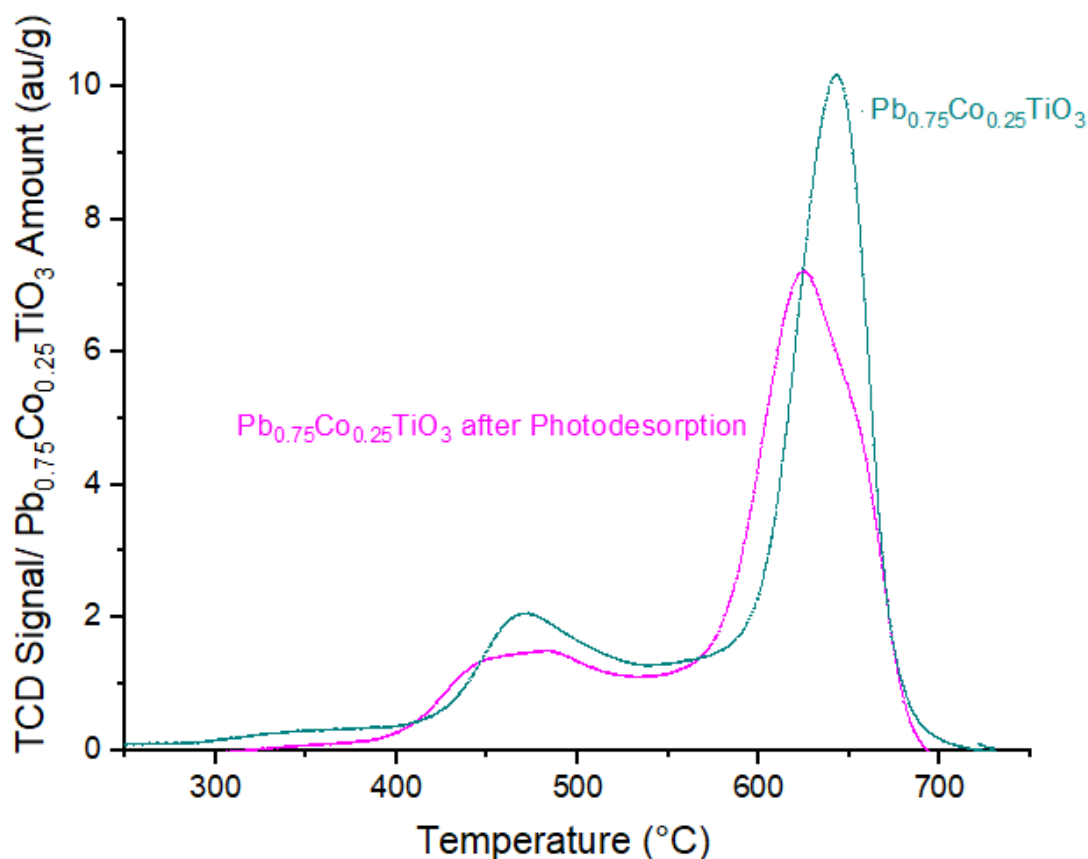


Figure 4.8 TPR profile of $\text{Pb}_{0.75}\text{Co}_{0.25}\text{TiO}_3$ before and after photodesorption

Figure 4.8 shows that there are three peaks for fresh $\text{Pb}_{0.75}\text{Co}_{0.25}\text{TiO}_3$ and two peaks for UV treated $\text{Pb}_{0.75}\text{Co}_{0.25}\text{TiO}_3$. For UV treated sample the first and second peaks are at 452°C and 625°C , respectively. For fresh sample the first, second and third peaks are at 158°C , 469°C and 643°C , respectively. The hydrogen consumed to reduce UV treated samples is less than the hydrogen consumed to reduce fresh sample. In addition, UV treated samples can be reduced at lower temperatures.

4.6.6 TPR of $\text{Pb}_{0.5}\text{Co}_{0.5}\text{TiO}_3$ before and after UV-irradiation exposure

As in Figure 4.9, there are four peaks for fresh and UV treated $\text{Pb}_{0.5}\text{Co}_{0.5}\text{TiO}_3$. For fresh sample, there are peaks at 400°C , 478°C , 558°C and 640°C and for UV treated sample the peaks are at 390°C , 464°C , 546°C and 632°C . The hydrogen consumption for the first three peaks are almost the same for UV treated and fresh samples. However, the for the last peak, hydrogen consumption to reduce UV treated sample is more than

the fresh sample. For this sample, conducting photodesorption and TPR after photodesorption experiments is recommended as future work.

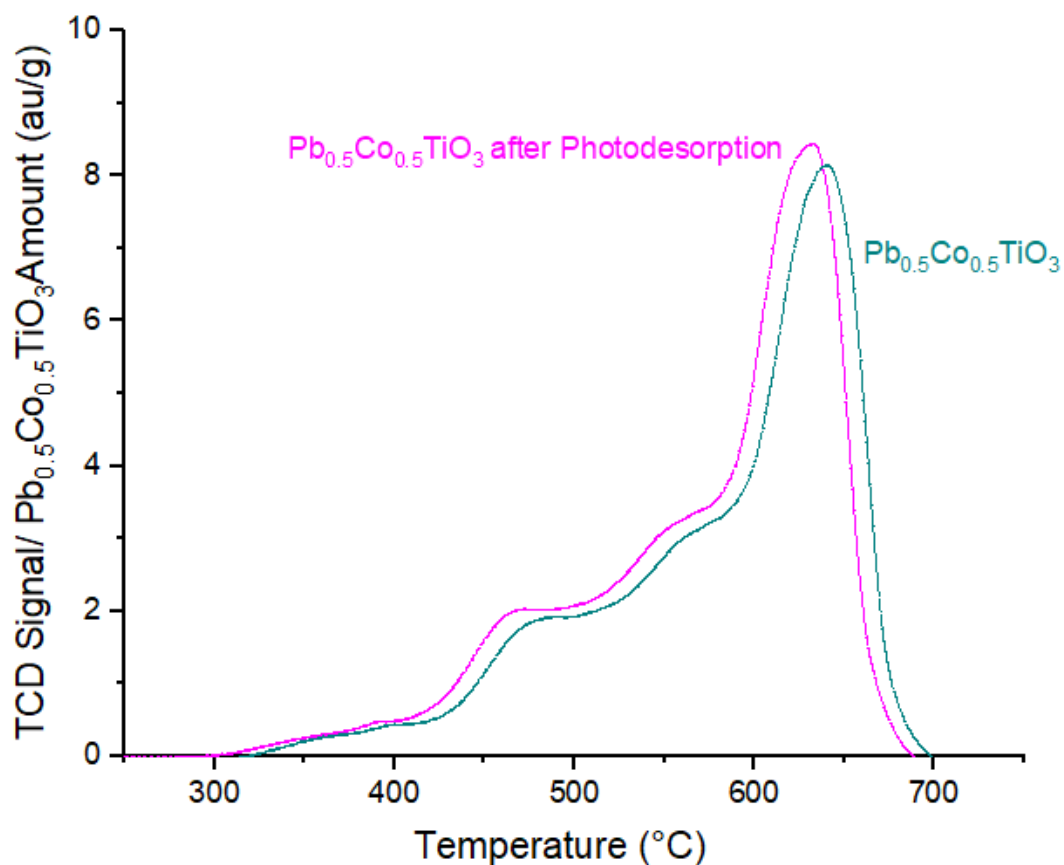


Figure 4.9 TPR profile of $\text{Pb}_{0.5}\text{Co}_{0.5}\text{TiO}_3$ before and after photodesorption

Table 4.4 TPR peak positions of synthesized perovskites

Samples	Peak Positions (°C)	
	UV treated samples	Fresh Sample
PbTiO_3	655	675
$\text{Pb}_{0.875}\text{Co}_{0.125}\text{TiO}_3$	437, 631	455, 646
$\text{Pb}_{0.75}\text{Co}_{0.25}\text{TiO}_3$	452, 625	158, 469, 643
$\text{Pb}_{0.5}\text{Co}_{0.5}\text{TiO}_3$	390, 464, 546, 632	400, 478, 558, 640

4.6.7 TPR of fresh perovskites

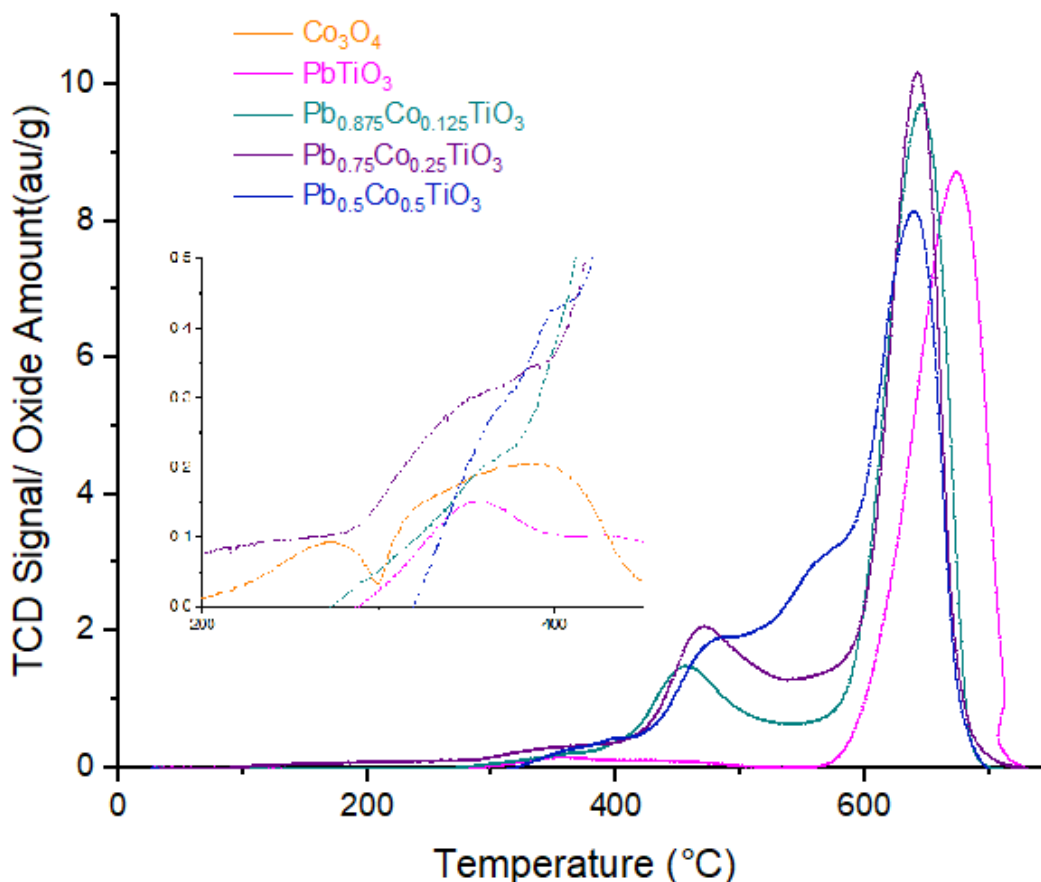


Figure 4.10 TPR profile of synthesized perovskites and Co_3O_4

To identify the TPR peaks, TPR analyses of fresh lead titanate, Co-doped lead titanate and Co_3O_4 were done. As seen in Figure 4.10, for lead titanate there is only one peak at 675°C and for Co_3O_4 there are three peaks at 159°C , 271°C and 386°C . For $\text{Pb}_{0.875}\text{Co}_{0.125}\text{TiO}_3$, there are two peaks are at 455°C and 646°C . For $\text{Pb}_{0.75}\text{Co}_{0.25}\text{TiO}_3$ the first, second and third peaks are at 158°C , 469°C and 643°C , respectively. For $\text{Pb}_{0.5}\text{Co}_{0.5}\text{TiO}_3$ there are peaks at 400°C , 478°C , 558°C and 640°C .

It is seen in Table 4.4 that the last peak can be seen for all perovskites which is around 630°C - 675°C . This peak is related to lead titanate. For lead titanate, by the help of UV treatment, sample can be reduced at lower temperatures. As Co content increases, peak position shifts to lower temperatures which means samples can be reduced at lower temperatures. Also, for UV treated samples, the ones containing cobalt can be reduced at lower temperatures. However, for UV treated samples, as Co content increases, peak position shifts to higher temperatures.

Table 4.5 Amount of hydrogen consumed to reduce fresh and photodesorbed samples and oxygen removed from samples

Sample	Calculated Area (au)			Hydrogen Consumption (mol/g _{oxide})			Oxygen removed (mol oxygen removed/mol oxygen stoichiometry)		
	Dark	After UV irradiation	Difference	Dark	After UV irradiation	Difference	Dark	After UV irradiation	Difference
PbTiO ₃	58.2	60.1	-1.9	4.25x10 ⁻³	4.39x10 ⁻³	-0.14x10 ⁻³	0.43	0.44	-0.01
Pb _{0.875} Co _{0.125} TiO ₃	69.8	62.8	7.0	5.10x10 ⁻³	4.59x10 ⁻³	0.51x10 ⁻³	0.48	0.44	0.04
Pb _{0.75} Co _{0.25} TiO ₃	75.4	65.8	9.6	5.50x10 ⁻³	4.81x10 ⁻³	0.71x10 ⁻³	0.49	0.43	0.06
Pb _{0.5} Co _{0.5} TiO ₃	80.4	84.8	-4.4	5.90x10 ⁻⁴	6.19x10 ⁻⁴	-0.29x10 ⁻⁴	0.45	0.47	-0.02

In Table 4.5, hydrogen consumption before and after UV treatment is given. While fresh PbTiO_3 consumed 4.25×10^{-3} moles of hydrogen per gram of fresh PbTiO_3 , UV treated PbTiO_3 consumed 4.39×10^{-3} moles of hydrogen per gram of UV treated PbTiO_3 . Fresh $\text{Pb}_{0.875}\text{Co}_{0.125}\text{TiO}_3$ consumed 5.10×10^{-3} moles of hydrogen per gram of fresh $\text{Pb}_{0.875}\text{Co}_{0.125}\text{TiO}_3$, UV treated $\text{Pb}_{0.875}\text{Co}_{0.125}\text{TiO}_3$ consumed 4.59×10^{-3} moles of hydrogen per gram of UV treated $\text{Pb}_{0.875}\text{Co}_{0.125}\text{TiO}_3$. Fresh $\text{Pb}_{0.75}\text{Co}_{0.25}\text{TiO}_3$ consumed 5.50×10^{-3} moles of hydrogen per gram of fresh $\text{Pb}_{0.75}\text{Co}_{0.25}\text{TiO}_3$, UV treated $\text{Pb}_{0.75}\text{Co}_{0.25}\text{TiO}_3$ consumed 4.81×10^{-3} moles of hydrogen per gram of UV treated $\text{Pb}_{0.75}\text{Co}_{0.25}\text{TiO}_3$. Fresh $\text{Pb}_{0.5}\text{Co}_{0.5}\text{TiO}_3$ consumed 5.90×10^{-4} moles of hydrogen per gram of fresh $\text{Pb}_{0.5}\text{Co}_{0.5}\text{TiO}_3$, UV treated $\text{Pb}_{0.5}\text{Co}_{0.5}\text{TiO}_3$ consumed 6.19×10^{-3} moles of hydrogen per gram of UV treated $\text{Pb}_{0.5}\text{Co}_{0.5}\text{TiO}_3$.

Oxygen stoichiometry of synthesized perovskites was studied by ICP-OES analysis and oxygen stoichiometries are given in Table 4.2. ICP measured stoichiometries were found as $\text{Pb}_{1.07}\text{TiO}_{2.69}$, $\text{Pb}_{0.98}\text{Co}_{0.13}\text{TiO}_{2.50}$, $\text{Pb}_{0.84}\text{Co}_{0.27}\text{TiO}_{2.66}$, $\text{Pb}_{0.55}\text{Co}_{0.53}\text{TiO}_{2.71}$ for PbTiO_3 , $\text{Pb}_{0.875}\text{Co}_{0.125}\text{TiO}_3$, $\text{Pb}_{0.75}\text{Co}_{0.25}\text{TiO}_3$, $\text{Pb}_{0.5}\text{Co}_{0.5}\text{TiO}_3$, respectively. It means that $\text{Pb}_{0.5}\text{Co}_{0.5}\text{TiO}_3$ has the largest oxygen content and $\text{Pb}_{0.875}\text{Co}_{0.125}\text{TiO}_3$ has the lowest oxygen content. However, in Table 4.5 it is seen that hydrogen consumption increases as cobalt content increases. Therefore, it can be concluded that cobalt doping results in easier reduction of PbTiO_3 .

4.7 NO Oxidation Experiments

4.7.1 Effect of Flow rate on Photocatalytic NO Oxidation

Figures 4.6- 4.11 shows the effect of cobalt doping on the reducibility and oxygen exchange behavior of lead titanate and Co-doped lead titanate under UV irradiation. The effect of Co-doping on photocatalytic activity of the perovskite materials were investigated by photocatalytic NO oxidation.

Effect of relative humidity, flow rate, wavelength of the light and initial NO concentration were examined. In addition, the dark light recycling experiments were conducted to see the stability of removal of NO under UV irradiation.

4.7.1.1 Photocatalytic NO Oxidation in 0 RH% in Air

To investigate the effect of flow rate on NO conversion with 0% RH, various flow rates were chosen as 0.5, 1.0 and 1.5 L/min. Initial NO concentration was around 500 ppb for all experiments. The amount of NO converted under UV irradiation and visible light irradiation was calculated.

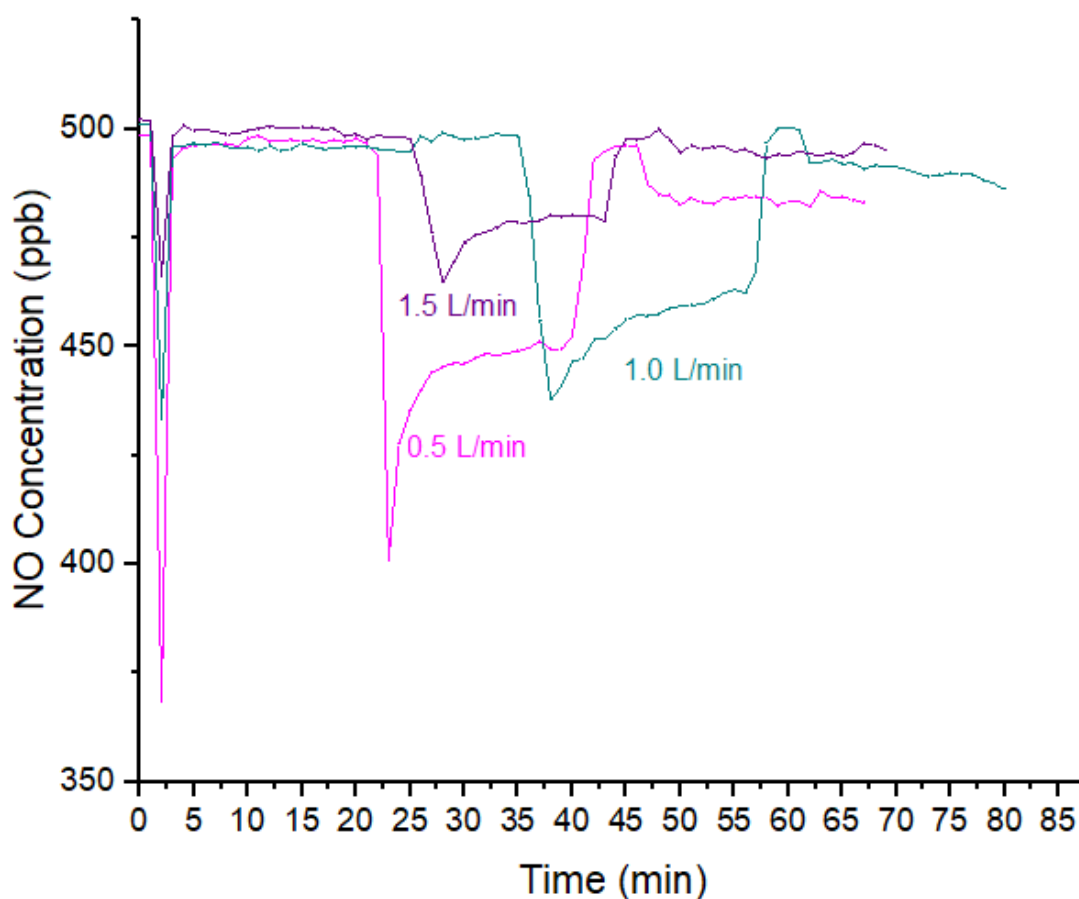


Figure 4.11 Photocatalytic NO Oxidation over PbTiO₃ at various flow rates

Figure 4.11 and Table 4.6 show that NO conversion over PbTiO₃ decreases with increasing flow rate. The sharp decrease at 25 min for 0.5 L/min, 30 min for 1.5 L/min and 37 min for 1L/min corresponds to when the UV is on. When UV is on, NO adsorbed on the surface is oxidized and NO conversion decreases by time. The sharp decrease and fast increase corresponds to the oxidation of NO adsorbed on surface during NO flow in dark. After 20 mins of UV irradiation exposure, NO flowed in the reactor for 5 minutes under dark condition. Then, the reactor was exposed to visible

light irradiation for 20 minutes. In Figure 4.12, it is seen that the effect of visible light irradiation is not significant.

Table 4.6 NO oxidation conversion over PbTiO₃ at various rates

Sample	UV conversion
PbTiO ₃ - 0% RH in air 0.5L/min	0.10
PbTiO ₃ - 0% RH in air 1.0L/min	0.07
PbTiO ₃ - 0% RH in air 1.5L/min	0.04

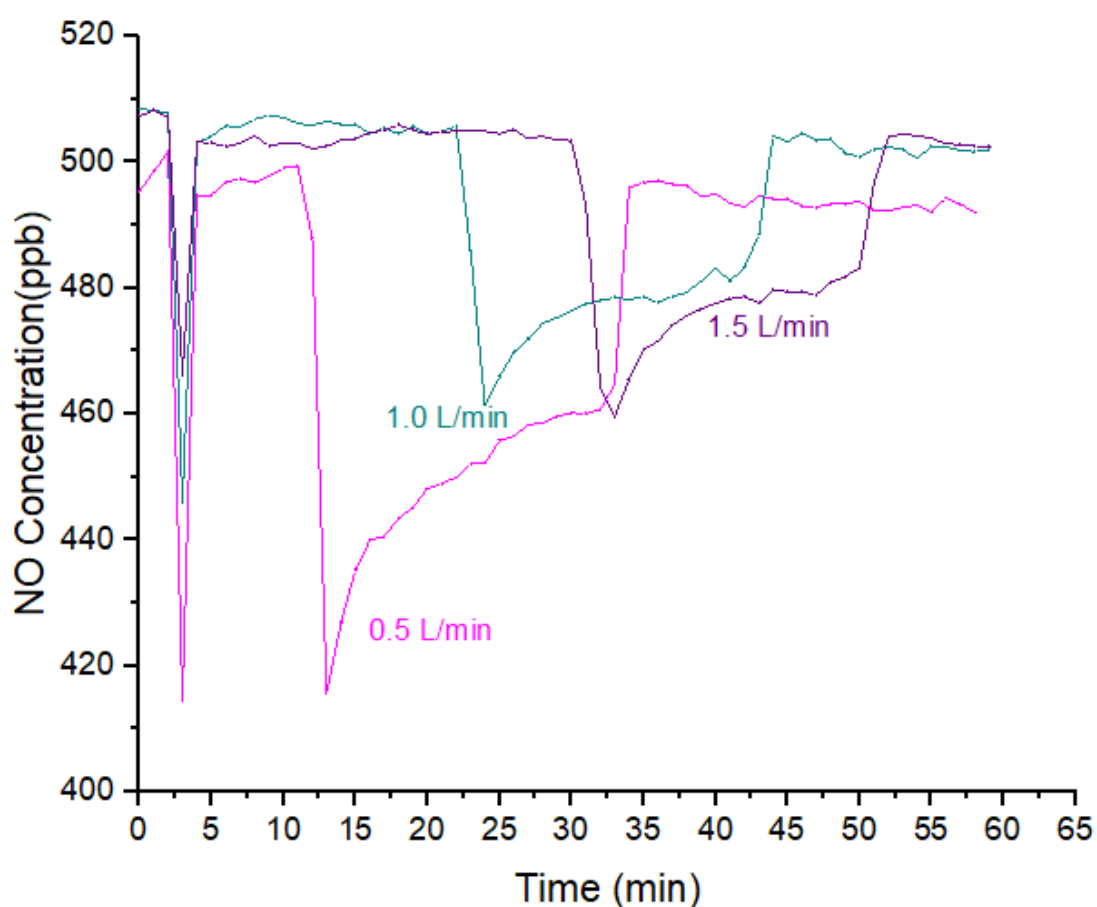


Figure 4.12 Photocatalytic NO Oxidation over Pb_{0.875}Co_{0.125}TiO₃ at various flow rates

Figure 4.12 and Table 4.7 show that NO conversion over Pb_{0.875}Co_{0.125}TiO₃ decreases with increasing flow rate. The sharp decrease at 13 min for 0.5 L/min, 25 min for 1 L/min and 35 min for 1.5 L/min corresponds to when the UV is on. The experimental

procedure was followed for $\text{Pb}_{0.875}\text{Co}_{0.125}\text{TiO}_3$. In Figure 4.14, it is seen that the effect of visible light irradiation is not significant.

Table 4.7 NO Oxidation conversion over $\text{Pb}_{0.875}\text{Co}_{0.125}\text{TiO}_3$ at various rates

Sample	UV conversion
$\text{Pb}_{0.875}\text{Co}_{0.125}\text{TiO}_3$ - 0% RH in air 0.5L/min	0.077
$\text{Pb}_{0.875}\text{Co}_{0.125}\text{TiO}_3$ - 0% RH in air 1.0L/min	0.054
$\text{Pb}_{0.875}\text{Co}_{0.125}\text{TiO}_3$ - 0% RH in air 1.5L/min	0.044

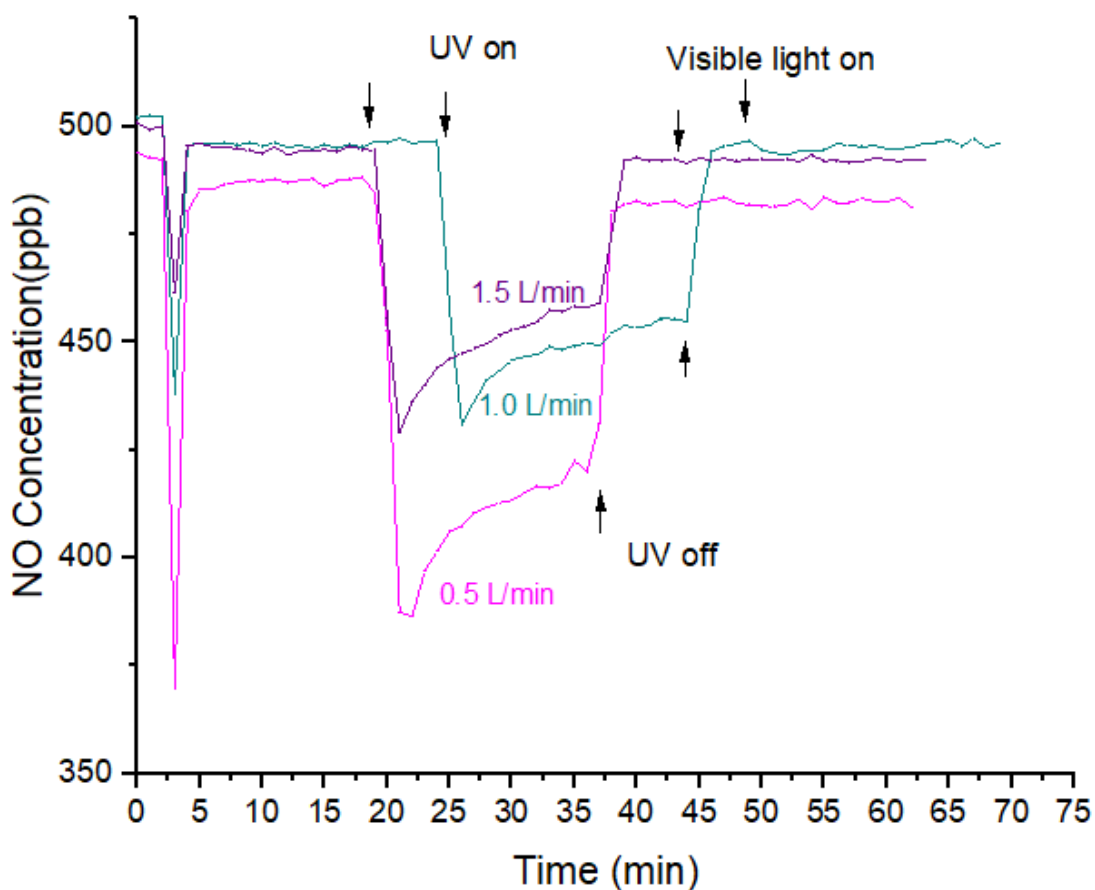


Figure 4.13 Photocatalytic NO Oxidation over $\text{Pb}_{0.75}\text{Co}_{0.25}\text{TiO}_3$ at various flow rates

Figure 4.13 and Table 4.8 show that NO conversion over $\text{Pb}_{0.75}\text{Co}_{0.25}\text{TiO}_3$ decreases with increasing flow rate. The sharp decrease at 20 min for 0.5 L/min and 1 L/min and 25 min for 1.5 L/min corresponds to when the UV is on. The experimental procedure

was followed for $\text{Pb}_{0.75}\text{Co}_{0.25}\text{TiO}_3$. In Figure 4.15, it is seen that the effect of visible light irradiation is not significant.

Table 4.8 NO oxidation conversion over $\text{Pb}_{0.75}\text{Co}_{0.25}\text{TiO}_3$ at various rates

Sample	UV conversion
$\text{Pb}_{0.75}\text{Co}_{0.25}\text{TiO}_3$ - 0% RH in air 0.5L/min	0.139
$\text{Pb}_{0.75}\text{Co}_{0.25}\text{TiO}_3$ - 0% RH in air 1.0L/min	0.085
$\text{Pb}_{0.75}\text{Co}_{0.25}\text{TiO}_3$ - 0% RH in air 1.5L/min	0.074

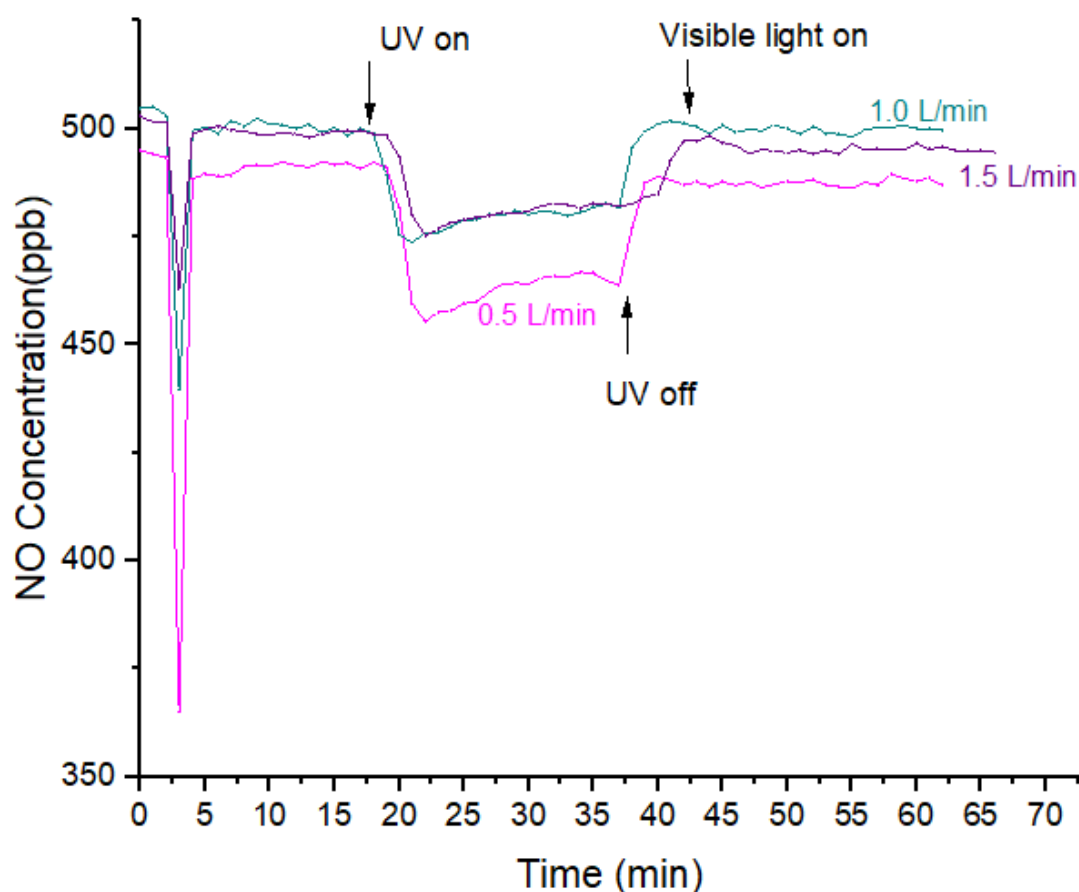


Figure 4.14 Photocatalytic NO Oxidation over $\text{Pb}_{0.5}\text{Co}_{0.5}\text{TiO}_3$ at various flow rates

Figure 4.14 and Table 4.9 show that NO conversion over $\text{Pb}_{0.5}\text{Co}_{0.5}\text{TiO}_3$ decreases with increasing flow rate. The sharp decrease at 20 min corresponds to when the UV is on. The experimental procedure was followed for $\text{Pb}_{0.5}\text{Co}_{0.5}\text{TiO}_3$. In Figure 4.16, it is seen that the effect of visible light irradiation is not significant.

Table 4.9 NO oxidation conversion over $\text{Pb}_{0.5}\text{Co}_{0.5}\text{TiO}_3$ at various rates

Sample	UV conversion
$\text{Pb}_{0.5}\text{Co}_{0.5}\text{TiO}_3$ - 0% RH in air 0.5L/min	0.058
$\text{Pb}_{0.5}\text{Co}_{0.5}\text{TiO}_3$ - 0% RH in air 1.0L/min	0.037
$\text{Pb}_{0.5}\text{Co}_{0.5}\text{TiO}_3$ - 0% RH in air 1.5L/min	0.028

4.7.1.2 Photocatalytic NO Oxidation in 50 RH% in Air

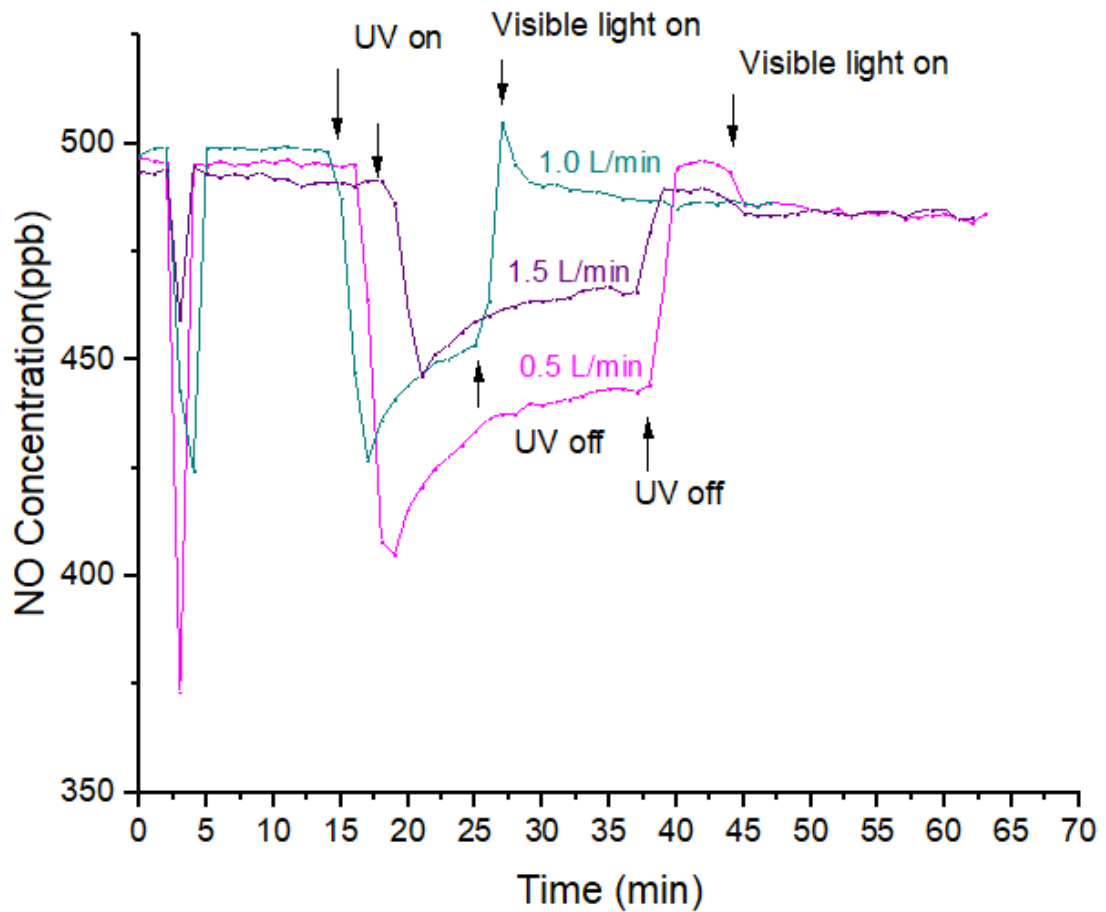


Figure 4.15 Photocatalytic NO Oxidation over PbTiO_3 at various flow rates

Figure 4.15 and Table 4.10 show that NO conversion over PbTiO_3 decreases with increasing flow rate. The sharp decrease at 15-20 min corresponds to when the UV is on. The experimental procedure was followed for PbTiO_3 . In Figure 4.17, it is seen that there is an effect of visible light but this effect is not very significant.

Table 4.10 NO oxidation conversion over PbTiO₃ at various rates

Sample	UV conversion
PbTiO ₃ - 50% RH in air 0.5 L/min	0.11
PbTiO ₃ - 50% RH in air 1.0 L/min	0.09
PbTiO ₃ - 50% RH in air 1.5 L/min	0.05

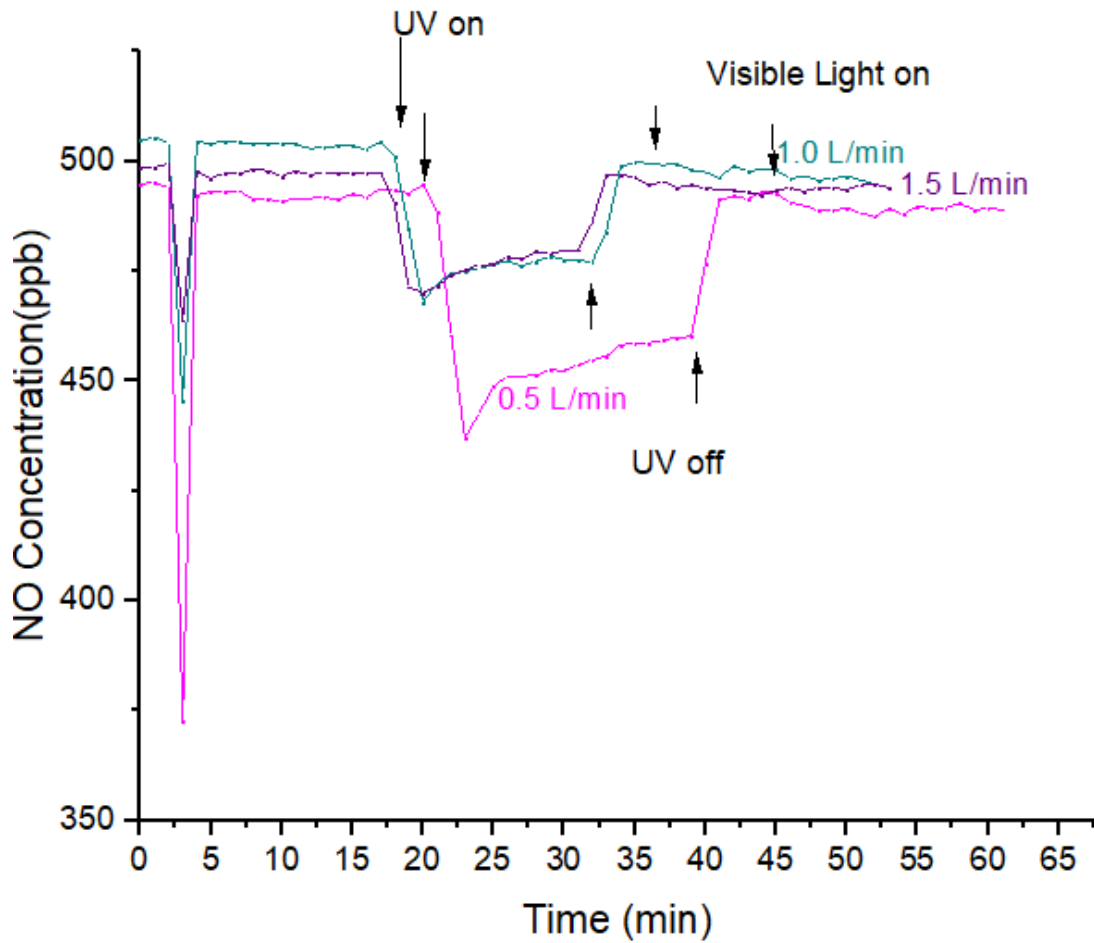


Figure 4.16 Photocatalytic NO Oxidation over Pb_{0.875}Co_{0.125}TiO₃ at various rates

Figure 4.16 and Table 4.11 show that NO conversion over Pb_{0.875}Co_{0.125}TiO₃ decreases with increasing flow rate. The sharp decrease at 20 min corresponds to when the UV is on. The experimental procedure was followed for PbTiO₃. In Figure 4.18, it is seen that the effect of visible light irradiation is not significant.

Table 4.11 NO oxidation conversion over $\text{Pb}_{0.875}\text{Co}_{0.125}\text{TiO}_3$ at various rates

Sample	UV conversion
$\text{Pb}_{0.875}\text{Co}_{0.125}\text{TiO}_3$ - 50% RH in air 0.5 L/min	0.073
$\text{Pb}_{0.875}\text{Co}_{0.125}\text{TiO}_3$ - 50% RH in air 1.0 L/min	0.045
$\text{Pb}_{0.875}\text{Co}_{0.125}\text{TiO}_3$ - 50% RH in air 1.5 L/min	0.035

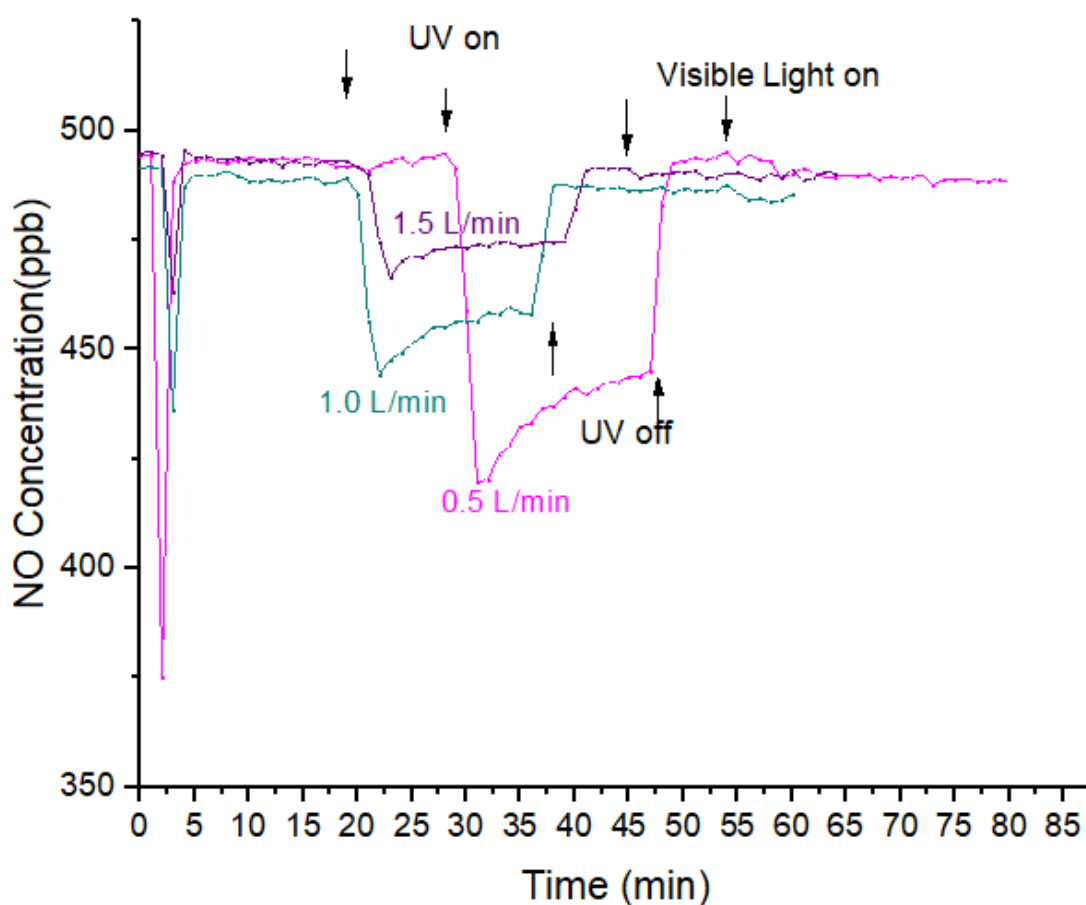


Figure 4.17 Photocatalytic NO Oxidation over $\text{Pb}_{0.75}\text{Co}_{0.25}\text{TiO}_3$ at various flow rates

Figure 4.17 and Table 4.12 show that NO conversion over $\text{Pb}_{0.75}\text{Co}_{0.25}\text{TiO}_3$ decreases with increasing flow rate. The sharp decrease at 30 min for 0.5 L/min and at 20 min for 1 L/min and 1.5 L/min corresponds to when the UV is on. The experimental procedure was followed for PbTiO_3 . In Figure 4.19, it is seen that the effect of visible light irradiation is not significant.

Table 4.12 NO oxidation conversion over $\text{Pb}_{0.75}\text{Co}_{0.25}\text{TiO}_3$ at various flow rates

Sample	UV conversion
$\text{Pb}_{0.75}\text{Co}_{0.25}\text{TiO}_3$ - 50% RH in air 0.5 L/min	0.099
$\text{Pb}_{0.75}\text{Co}_{0.25}\text{TiO}_3$ - 50% RH in air 1.0 L/min	0.063
$\text{Pb}_{0.75}\text{Co}_{0.25}\text{TiO}_3$ - 50% RH in air 1.5 L/min	0.054

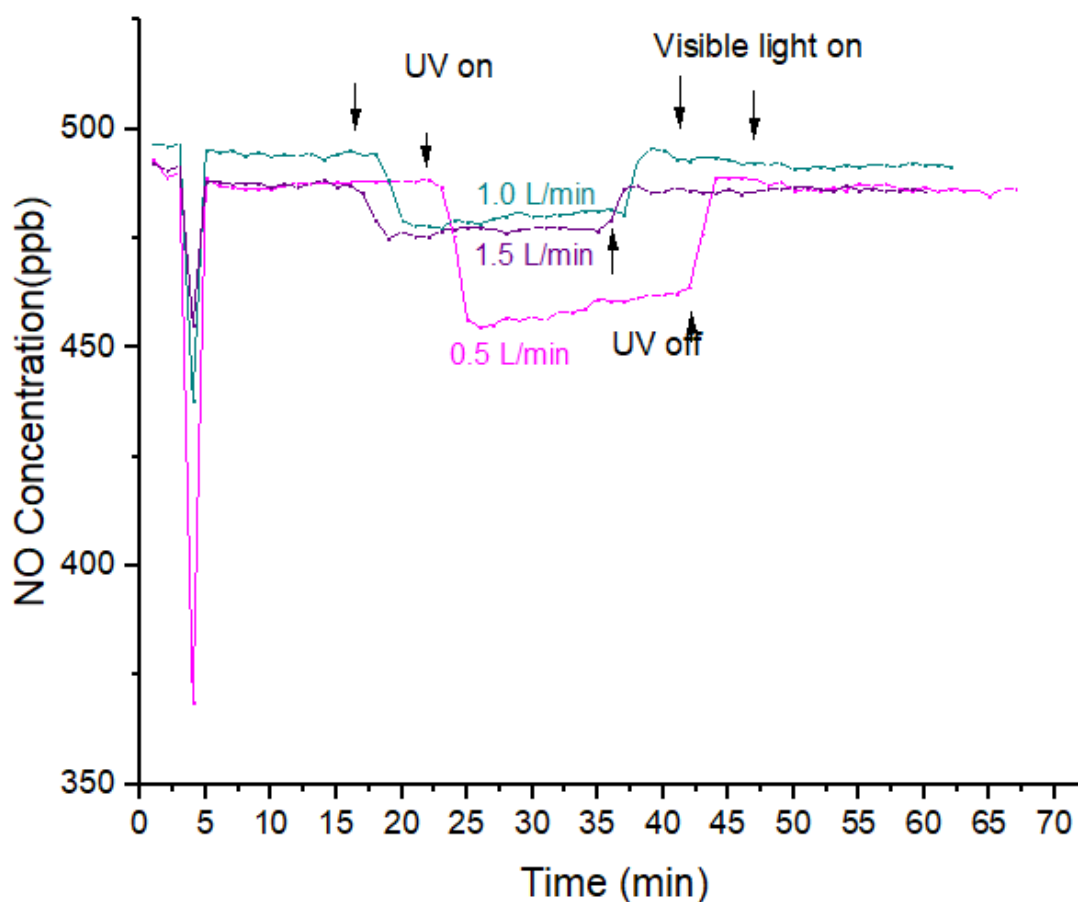


Figure 4.18 Photocatalytic NO Oxidation over $\text{Pb}_{0.5}\text{Co}_{0.5}\text{TiO}_3$ at various flow rates

Figure 4.18 and Table 4.13 show that NO conversion over $\text{Pb}_{0.5}\text{Co}_{0.5}\text{TiO}_3$ decreases with increasing flow rate. The sharp decrease at 25 min for 0.5 L/min and at 20 min for 1 L/min and 1.5 L/min corresponds to when the UV is on. The experimental

procedure was followed for PbTiO_3 . In Figure 4.29, it is seen that the effect of visible light irradiation is not significant.

Table 4.13 NO oxidation conversion over $\text{Pb}_{0.5}\text{Co}_{0.5}\text{TiO}_3$ at various flow rates

Sample	UV conversion
$\text{Pb}_{0.5}\text{Co}_{0.5}\text{TiO}_3$ - 50% RH in air 0.5 L/min	0.050
$\text{Pb}_{0.5}\text{Co}_{0.5}\text{TiO}_3$ - 50% RH in air 1.0 L/min	0.028
$\text{Pb}_{0.5}\text{Co}_{0.5}\text{TiO}_3$ - 50% RH in air 1.5 L/min	0.016

4.7.2 Effect of Relative Humidity on Photocatalytic NO Oxidation

The effect of RH on photocatalytic NO Oxidation over PbTiO_3 is seen in Table 14. As relative humidity increases, photocatalytic conversion of NO under UV irradiation increases. The effect of RH on visible light conversion could not be identified by these experiments.

Table 4.14 UV and Visible Light Conversions of NO over PbTiO_3 at different RH

Samples	UV conversion	
	50 % RH	0% RH
PbTiO_3 -0.5L/min	0.11	0.10
PbTiO_3 -1 L/min	0.09	0.07
PbTiO_3 -1.5L/min	0.05	0.04

The effect of RH on photocatalytic NO Oxidation over $\text{Pb}_{0.875}\text{Co}_{0.125}\text{TiO}_3$ is seen in Table 15. As relative humidity increases, photocatalytic conversion of NO under UV irradiation decreases. The effect of RH on visible light conversion could not be identified by these experiments.

Table 4.15 UV and Visible Light Conversions of NO over $\text{Pb}_{0.875}\text{Co}_{0.125}\text{TiO}_3$ at different RH

Sample	UV Conversion	
	50% RH	0% RH
$\text{Pb}_{0.875}\text{Co}_{0.125}\text{TiO}_3$ -0.5L/min	0.073	0.077
$\text{Pb}_{0.875}\text{Co}_{0.125}\text{TiO}_3$ -1 L/min	0.045	0.054
$\text{Pb}_{0.875}\text{Co}_{0.125}\text{TiO}_3$ -1.5L/min	0.035	0.044

The effect of RH on photocatalytic NO Oxidation over $\text{Pb}_{0.75}\text{Co}_{0.25}\text{TiO}_3$ is seen in Table 16. As relative humidity increases, photocatalytic conversion of NO under UV irradiation decreases. The effect of RH on visible light conversion could not be identified by these experiments.

Table 4.16 UV and Visible Light Conversions of NO over $\text{Pb}_{0.75}\text{Co}_{0.25}\text{TiO}_3$ at different RH

Sample	UV conversion	
	50% RH	0% RH
$\text{Pb}_{0.75}\text{Co}_{0.25}\text{TiO}_3$ - 0.5L/min	0.099	0.139
$\text{Pb}_{0.75}\text{Co}_{0.25}\text{TiO}_3$ - 1 L/min	0.063	0.085
$\text{Pb}_{0.75}\text{Co}_{0.25}\text{TiO}_3$ - 1.5L/min	0.054	0.074

The effect of RH on photocatalytic NO Oxidation over $\text{Pb}_{0.5}\text{Co}_{0.5}\text{TiO}_3$ is seen in Table 17. As relative humidity increases, photocatalytic conversion of NO under UV irradiation decreases. The effect of RH on visible light conversion could not be identified by these experiments.

Table 4.17 UV and Visible Light Conversions of NO over $\text{Pb}_{0.5}\text{Co}_{0.5}\text{TiO}_3$ at different RH

Sample	UV Conversion	
	50% RH	0% RH
$\text{Pb}_{0.5}\text{Co}_{0.5}\text{TiO}_3$ - 0.5L/min	0.050	0.058
$\text{Pb}_{0.5}\text{Co}_{0.5}\text{TiO}_3$ - 1 L/min	0.028	0.037
$\text{Pb}_{0.5}\text{Co}_{0.5}\text{TiO}_3$ - 1.5L/min	0.016	0.028

4.7.3 Dark-Light Cyclic Photocatalytic NO Oxidation Experiments

4.7.3.1 Dark-Light Cyclic Photocatalytic NO Oxidation Experiments in 0% RH in air

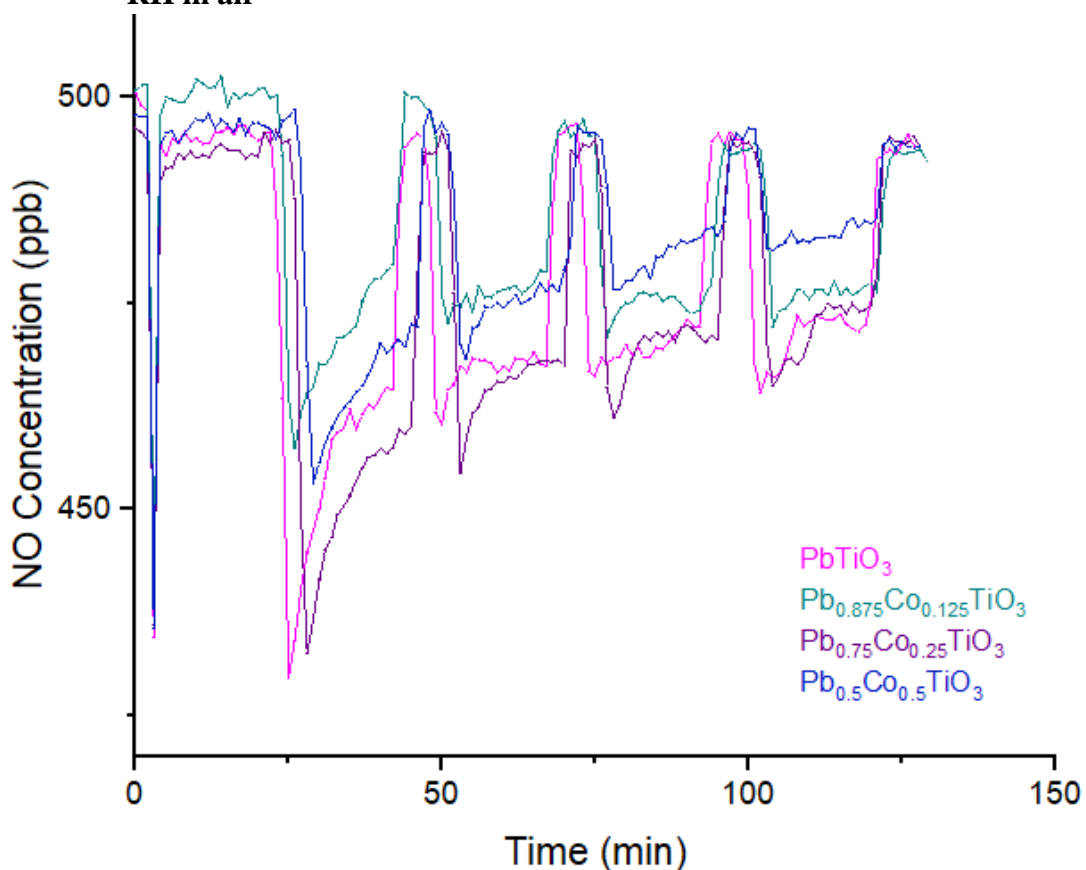


Figure 4.19 Dark-Light Cyclic Photocatalytic NO Oxidation over perovskites in 0% RH

Table 4.18 NO Conversions in 0% RH

Cycles	Conversion			
	PbTiO ₃	Pb _{0.875} Co _{0.125} TiO ₃	Pb _{0.75} Co _{0.25} TiO ₃	Pb _{0.5} Co _{0.5} TiO ₃
Cycle 1	0.063	0.040	0.071	0.050
Cycle 2	0.057	0.040	0.056	0.036
Cycle 3	0.050	0.044	0.048	0.026
Cycle 4	0.046	0.036	0.040	0.022

In Figure 4.19 and Table 4.18, it is seen that conversions decreases as the cycle number increases. It was shown in Chapter 4.14 that Pb_{0.75}Co_{0.25}TiO₃ has the largest NO conversion in 0% RH and it was followed by PbTiO₃, Pb_{0.875}Co_{0.125}TiO₃ and Pb_{0.5}Co_{0.5}TiO₃. In the first cycles, again, Pb_{0.75}Co_{0.25}TiO₃ has the largest NO conversion in 0% RH. However, it is followed by PbTiO₃, Pb_{0.5}Co_{0.5}TiO₃ and Pb_{0.875}Co_{0.125}TiO₃. As cycle number increases, NO conversion decreases for all samples. The rate of decrease is different for all samples so in cycle 4, PbTiO₃ shows better activity than Pb_{0.75}Co_{0.25}TiO₃ and also Pb_{0.875}Co_{0.125}TiO₃ shows better activity than Pb_{0.5}Co_{0.5}TiO₃.

4.7.3.2 Dark-Light Cyclic Photocatalytic NO Oxidation Experiments in 50% RH in air

Table 4.19 NO Conversions in 50% RH

Cycles	Conversion			
	PbTiO ₃	Pb _{0.875} Co _{0.125} TiO ₃	Pb _{0.75} Co _{0.25} TiO ₃	Pb _{0.5} Co _{0.5} TiO ₃
Cycle 1	0.068	0.055	0.057	0.034
Cycle 2	0.054	0.042	0.053	0.040
Cycle 3	0.050	0.038	0.053	0.036
Cycle 4	0.048	0.041	0.047	0.032

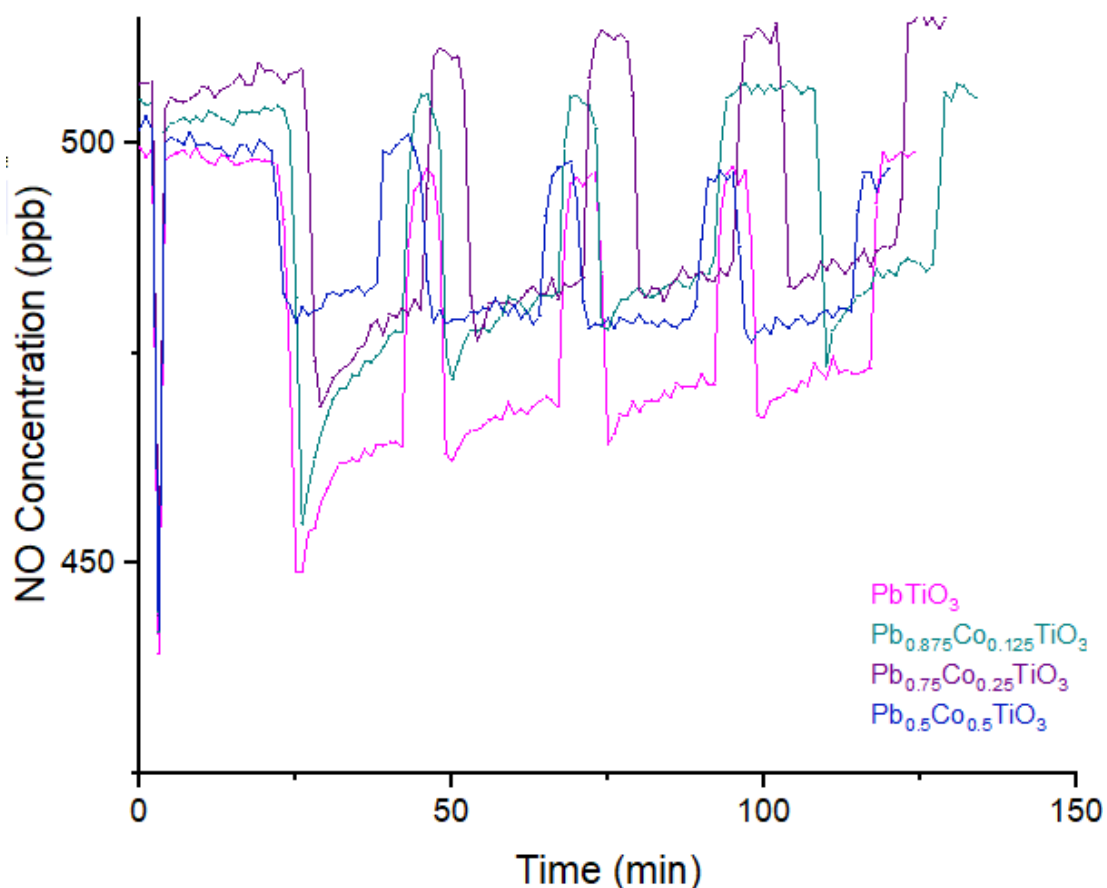


Figure 4.20 Dark-Light Cyclic Photocatalytic NO Oxidation over perovskites in 50% RH

In Figure 4.20 and Table 4.19, it is seen that conversions decreases as the cycle number increases. It was shown in Chapter 4.14 that PbTiO_3 has the largest NO conversion in 50% RH and it was followed by $\text{Pb}_{0.75}\text{Co}_{0.25}\text{TiO}_3$, $\text{Pb}_{0.875}\text{Co}_{0.125}\text{TiO}_3$ and $\text{Pb}_{0.5}\text{Co}_{0.5}\text{TiO}_3$. In the first cycles, again, PbTiO_3 has the largest NO conversion in 50% RH and it is followed by $\text{Pb}_{0.75}\text{Co}_{0.25}\text{TiO}_3$, $\text{Pb}_{0.875}\text{Co}_{0.125}\text{TiO}_3$ and $\text{Pb}_{0.5}\text{Co}_{0.5}\text{TiO}_3$. As cycle number increases, NO conversion decreases for all samples. However, the decrease in 50% RH is less than the decrease in 0% RH.

4.8 Adsorption Measurements and Adsorption Calorimetry

To investigate the H_2O adsorption capacity of synthesized perovskites, static volumetric chemisorption experiments were conducted on TiO_2 , PbTiO_3 , $\text{Pb}_{0.875}\text{Co}_{0.125}\text{TiO}_3$, $\text{Pb}_{0.75}\text{Co}_{0.25}\text{TiO}_3$ and $\text{Pb}_{0.5}\text{Co}_{0.5}\text{TiO}_3$.

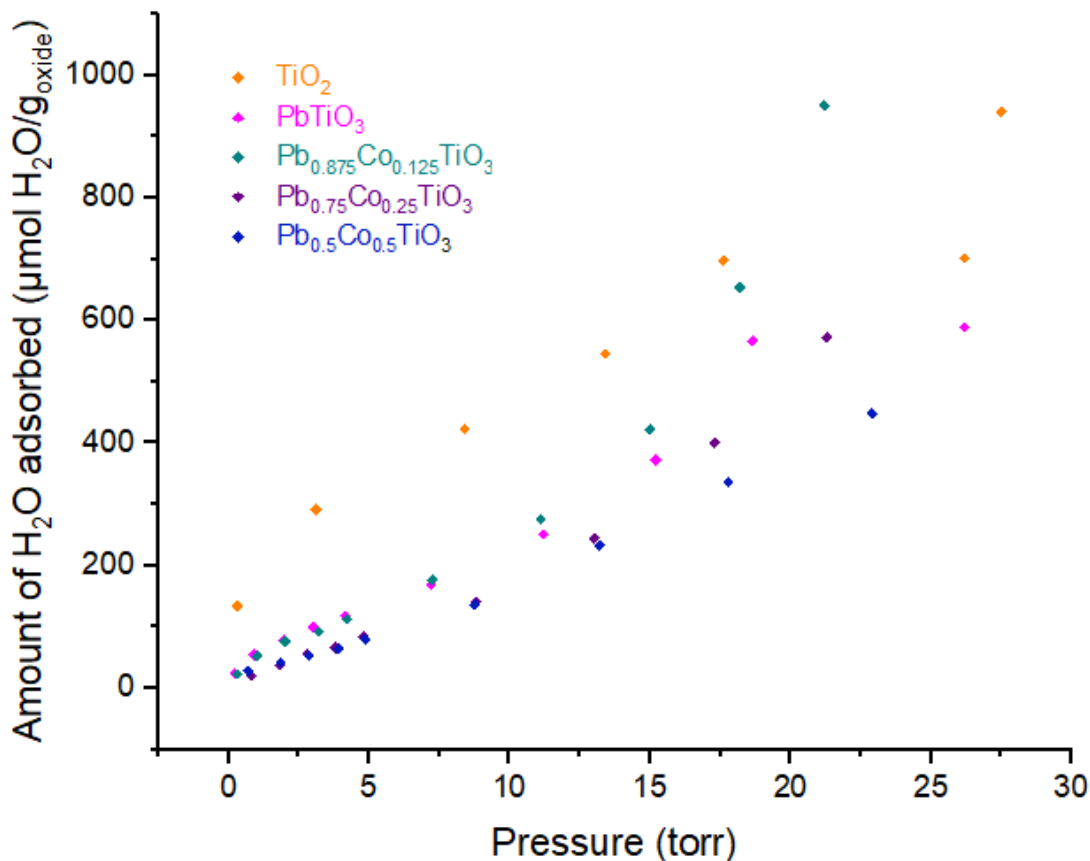


Figure 4.21 H₂O adsorption isotherms for TiO₂, PbTiO₃, Pb_{0.875}Co_{0.125}TiO₃, Pb_{0.75}Co_{0.25}TiO₃ and Pb_{0.5}Co_{0.5}TiO₃ at 50°C

Figure 4.21 shows that At lower pressures H₂O adsorption capacity of synthesized perovskites was found to be lower than H₂O adsorption capacity of TiO₂ and no significant difference was observed for perovskites. However, as pressure increases, H₂O adsorption capacity of Pb_{0.875}Co_{0.125}TiO₃ got larger than H₂O adsorption capacity of TiO₂ above 22 torr and H₂O adsorption capacity of perovskites got smaller as cobalt content increases for PbTiO₃, Pb_{0.75}Co_{0.25}TiO₃ and Pb_{0.5}Co_{0.5}TiO₃.

In Figure 4.22, the differential heats of adsorption of H₂O on TiO₂, PbTiO₃ and Pb_{0.875}Co_{0.125}TiO₃ show that adsorbing H₂O on TiO₂ surface causes to release more energy than perovskites. Also, differential heats of adsorption of H₂O on PbTiO₃ is larger than Pb_{0.875}Co_{0.125}TiO₃.

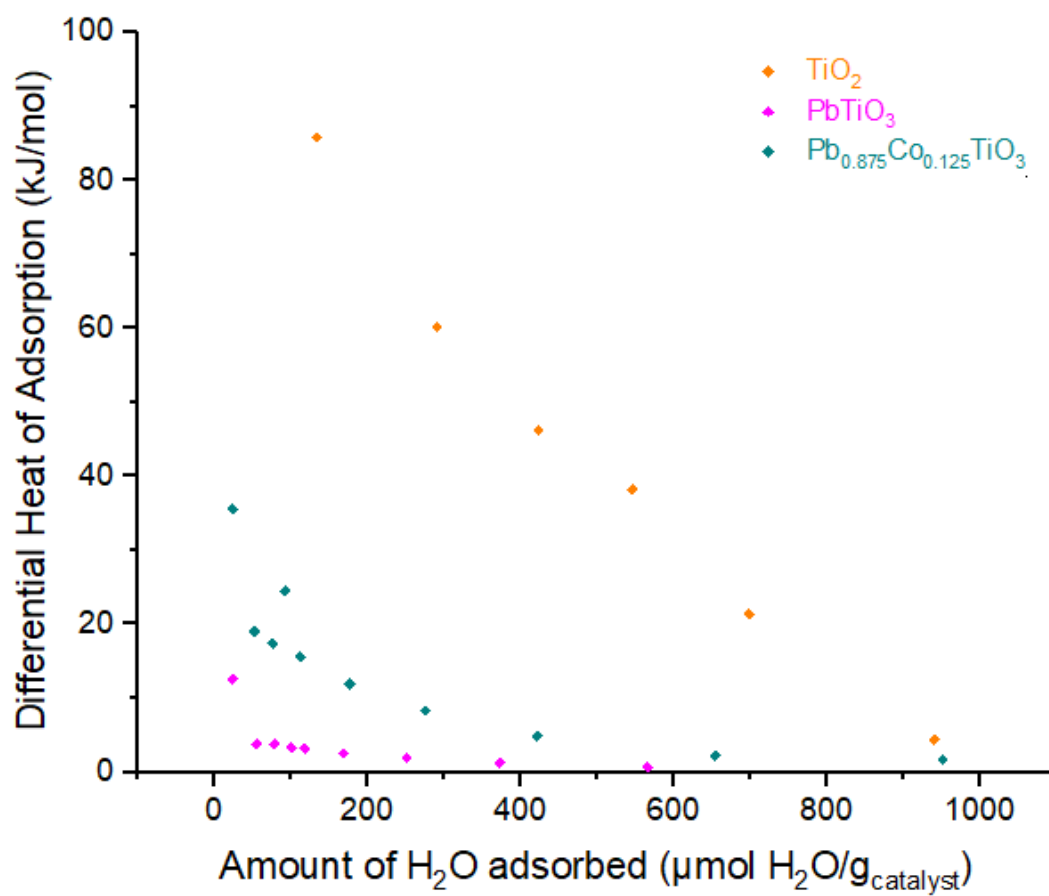


Figure 4.22 Differential heats of H₂O adsorption on TiO₂, PbTiO₃ and Pb_{0.875}Co_{0.125}TiO₃ at 50°C

CHAPTER V

CONCLUSION

The effect of cobalt doping on photocatalytic activity of lead titanate was studied by NO oxidation and TP_x analyses. $PbTiO_3$, $Pb_{0.875}Co_{0.125}TiO_3$, $Pb_{0.75}Co_{0.25}TiO_3$ and $Pb_{0.5}Co_{0.5}TiO_3$ were synthesized by sol-gel method. Crystal phases of the perovskites were studied by XRD analysis. For all perovskites, characteristic peaks for $PbTiO_3$ were detected and as Co content increases, peaks became less intense and wider. Therefore, as Co content increases, crystallite size decreases. BET Analysis was used to investigate the effect of Co-doping on the surface area. It is concluded that Co-doping causes higher surface areas and smaller crystallite size. DCS Analysis is used to see the effect of Co-doping on the Curie temperature of lead titanate. For lead titanate, characteristic peak of Curie temperature was observed. However, no peaks were observed between $30^\circ C$ - $550^\circ C$ for Co-doped perovskites. By ICP-OES analysis, the expected Pb/Co and (Pb+Co)/Ti ratios were obtained. However, oxygen stoichiometry was found to be lower than expected.

To see the effect of UV irradiation on oxygen desorption from the photocatalyst 0.5 wt% Pt/TiO₂, which is a better-known oxide, UV desorption and TPR experiments were conducted on Micromeritics Chemisorb 2720 equipment. It was found out that reducibility of TiO₂ and 0.5 wt% Pt/TiO₂ decreased after UV exposure. For fresh TiO₂, a peak at $125^\circ C$ and a broad peak between $200^\circ C$ and $700^\circ C$ were observed. For UV treated TiO₂, there are three peaks around $60^\circ C$, $181^\circ C$ and a broad peak around $200^\circ C$ and $700^\circ C$. The first peak around $50^\circ C$ and the second and third peaks around $120^\circ C$ and $130^\circ C$ were observed for TPR of fresh and UV-exposed 0.5 wt% Pt/TiO₂ samples. However, hydrogen consumed to reduce fresh sample was more than the hydrogen consumed to reduce UV-exposed sample. By the help of UV light irradiation, TiO₂ and 0.5 wt% Pt/TiO₂ was reduced and oxygen was desorbed during UV exposure.

The hydrogen consumption for UV treated PbTiO_3 and $\text{Pb}_{0.5}\text{Co}_{0.5}\text{TiO}_3$ was larger than fresh samples. However, The hydrogen consumption for UV treated $\text{Pb}_{0.875}\text{Co}_{0.125}\text{TiO}_3$ and $\text{Pb}_{0.75}\text{Co}_{0.25}\text{TiO}_3$ was smaller than fresh samples.

NO Oxidation experiments are conducted to see the effect of Co-doping on the photocatalytic activity of lead titanate. Experiments were conducted under UV and visible light irradiation. For all perovskites, the effect of Co-doping, flow rate and relative humidity in air were investigated. For all perovskites, it is seen that as flow rate increases conversion of NO decreases under UV and visible light irradiation. The higher flow rate means the lower residence time in reactor. The reaction is in the kinetically controlled regime. For PbTiO_3 as relative humidity increases conversion of NO increases under UV irradiation and there is no noticeable effect of visible light irradiation. The increase in conversion with the higher relative humidity is explained by the adsorption of water on the surface of the photocatalyst and more effective oxidation of NO by the help of OH species. However, Co-doped showed less photocatalytic activity under UV-irradiation and the effect of visible light irradiation was not noticeable. This is explained by the surface poisoning. When the water content in the air increases, water is adsorbed on the active sites. However, unlike PbTiO_3 , surface OH molecules cannot oxidize NO molecules. Dark-light cycling experiments showed that relative humidity helps to have more stable photocatalytic activity.

The amount of water adsorbed on TiO_2 and synthesized perovskites and the heats of H_2O adsorption experiments showed that the amount of water adsorbed on TiO_2 was more than the synthesized perovskites for lower pressures. However, water adsorbed on $\text{Pb}_{0.875}\text{Co}_{0.125}\text{TiO}_3$ was found to be more than TiO_2 around 22 torrs. Differential heat of water adsorption on TiO_2 was larger than PbTiO_3 and $\text{Pb}_{0.875}\text{Co}_{0.125}\text{TiO}_3$ and differential heat of water adsorption on PbTiO_3 was larger than $\text{Pb}_{0.875}\text{Co}_{0.125}\text{TiO}_3$.

Reactor analysis was done by using TiO_2 . The behavior of the reactor was found to be more like PFR.

REFERENCES

- [1] G. Pacchioni, "Oxygen Vacancy: The Invisible Agent on Oxide Surfaces," *ChemPhysChem*, vol. 4, no. 10, pp. 1041–1047, 2003.
- [2] M. V. Raymond and D. M. Smyth, "Defects and charge transport in perovskite ferroelectrics," *J. Phys. Chem. Solids*, vol. 57, no. 10, pp. 1507–1511, 1996.
- [3] R. Das, S. Sharma, and K. Mandal, "Aliovalent Ba²⁺ doping: A way to reduce oxygen vacancy in multiferroic BiFeO₃," *J. Magn. Magn. Mater.*, vol. 401, pp. 129–137, 2016.
- [4] T. Minato, M. Kawai, and Y. Kim, "Creation of single oxygen vacancy on titanium dioxide surface," *J. Mater. Res.*, vol. 27, no. 17, pp. 2237–2240, 2012.
- [5] U. Diebold, "The surface science of titanium dioxide," *Surf. Sci. Rep.*, vol. 48, no. 5, pp. 53–229, 2003.
- [6] J. T. Yates, "Photochemistry on TiO₂: Mechanisms behind the surface chemistry," *Surf. Sci.*, vol. 603, no. 10–12, pp. 1605–1612, 2009.
- [7] T. L. Thompson, O. Diwald, and J. T. Yates, "Molecular oxygen-mediated vacancy diffusion on TiO₂(110)-new studies of the proposed mechanism," *Chem. Phys. Lett.*, vol. 393, no. 1–3, pp. 28–30, 2004.
- [8] G. Wang, X. Lu, and Y. Li, "Hydrogen-Treated TiO₂ Nanowires for Charge Storage and Photoelectrochemical Water Splitting," *Black TiO₂ Nanomater. Energy Appl.*, pp. 189–213, 2017.
- [9] M. A. Henderson, W. S. Epling, C. L. Perkins, C. H. F. Peden, and U. Diebold, "Interaction of Molecular Oxygen with the Vacuum-Annealed TiO₂ (110) Surface: Molecular and Dissociative Channels," *J. Phys. Chem. B*, vol. 103, no. 25, pp. 5328–5337, 1999.
- [10] A. A. Ismail and D. W. Bahnemann, "Photochemical splitting of water for hydrogen production by photocatalysis: A review," *Sol. Energy Mater. Sol. Cells*, vol. 128, pp. 85–101, 2014.

- [11] G. Lu, A. Linsebigler, and J. T. Yates, "The photochemical identification of two chemisorption states for molecular oxygen on TiO₂(110)," *J. Chem. Phys.*, vol. 102, no. 7, pp. 3005–3008, 1995.
- [12] K. Tanaka and K. Miyahara, "Adsorption of COP on TiO₂ and Pt/TiO₂ Studied by X-ray Photoelectron Spectroscopy and Auger Electron Spectroscopy," no. 12, pp. 3504–3508, 1984.
- [13] Y. Na, P. Lincoln, J. R. Johansson, and B. Nordén, "Towards Artificial Photosynthesis of CO₂-Neutral Fuel: Homogenous Catalysis of CO₂-Selective Reduction to Methanol Initiated by Visible-Light-Driven Multi-Electron Collector," *ChemCatChem*, vol. 4, no. 11, pp. 1746–1750, 2012.
- [14] A. Kakekhani and S. Ismail-Beigi, "Ferroelectric oxide surface chemistry: Water splitting via pyroelectricity," *J. Mater. Chem. A*, vol. 4, no. 14, pp. 5235–5246, 2016.
- [15] L. G. Tejuca and J. L. G. Fierro, *Properties and Applications of Perovskite-Type Oxides*. New York: Marcel Dekker, 1993.
- [16] R. J. D. Tilley, *Perovskites: Structure-Property Relationships*. 2016.
- [17] M. Petrović, V. Chellappan, and S. Ramakrishna, "Perovskites: Solar cells & engineering applications - materials and device developments," *Sol. Energy*, vol. 122, pp. 678–699, 2015.
- [18] L. W. Martin and R. Ramesh, "Multiferroic and magnetoelectric heterostructures," *Acta Mater.*, vol. 60, no. 6–7, pp. 2449–2470, 2012.
- [19] W. Ge *et al.*, "Optimizing the photocatalysis in ferromagnetic Bi₆Fe_{1.9}Co_{0.1}Ti₃O₁₈ nanocrystal by morphology control," *RSC Adv.*, vol. 5, no. 67, pp. 54165–54170, 2015.
- [20] R. G. Harrison, "Calculating the spontaneous magnetization and defining the Curie temperature using a positive-feedback model," *J. Appl. Phys.*, vol. 115, no. 3, 2014.
- [21] A. Leonhardt *et al.*, "Synthesis, Properties, and Applications of Ferromagnetic-Filled Carbon Nanotubes," *Chem. Vap. Depos.*, vol. 12, no. 6, pp. 380–387,

2006.

- [22] A. Akbarzadeh, M. Samiei, and S. Davaran, “Magnetic nanoparticles : preparation , physical properties , and applications in biomedicine,” pp. 1–13, 2012.
- [23] K. Siratori, K. Kohn, and E. Kita, “Magnetolectric Effect in Magnetic Materials,” *Acta Phys. Pol. A*, vol. 81, no. 4, pp. 431–466, 1992.
- [24] M. Q. Le, F. Belhora, A. Cornogolub, P. J. Cottinet, L. Lebrun, and A. Hajjaji, “Enhanced magnetolectric effect for flexible current sensor applications,” *J. Appl. Phys.*, vol. 115, no. 19, pp. 0–10, 2014.
- [25] Y. Cui, J. Briscoe, and S. Dunn, “E ff ect of Ferroelectricity on Solar-Light-Driven Photocatalytic Activity of BaTiO₃ Influence on the Carrier Separation and Stern Layer Formation,” *Chem. Mater.*, vol. 25, pp. 4215–4223, 2013.
- [26] L. W. Martin and A. M. Rappe, “Thin-film ferroelectric materials and their applications,” *Nat. Rev. Mater.*, vol. 2, no. 2, 2016.
- [27] J. M. Hu, L. Q. Chen, and C. W. Nan, “Multiferroic Heterostructures Integrating Ferroelectric and Magnetic Materials,” *Adv. Mater.*, vol. 28, no. 1, pp. 15–39, 2016.
- [28] C. Pavithra and W. Madhuri, “Dielectric, piezo and ferroelectric properties of microwave sintered PbTiO₃ synthesized by sol–gel method,” *J. Sol-Gel Sci. Technol.*, vol. 85, no. 2, pp. 437–445, 2018.
- [29] V. A. Chaudhari and G. K. Bichile, “Synthesis, Structural, and Electrical Properties of Pure PbTiO₃ Ferroelectric Ceramics,” *Smart Mater. Res.*, vol. 2013, p. 147524, 2013.
- [30] N. A. Hill and A. Filippetti, “Why are there any magnetic ferroelectrics?,” *J. Magn. Magn. Mater.*, vol. 242–245, no. PART II, pp. 976–979, 2002.
- [31] H. S. Bhatti, S. T. Hussain, F. A. Khan, and S. Hussain, “Synthesis and induced multiferroicity of perovskite PbTiO₃; A review,” *Appl. Surf. Sci.*, vol. 367, pp. 291–306, 2016.
- [32] D. Damjanovic, “Ferroelectric, dielectric and piezoelectric properties of

- ferroelectric thin films and ceramics,” *Reports Prog. Phys.*, vol. 61, pp. 1267–1324, 1998.
- [33] Y. Liu, G. Xu, C. Song, Z. Ren, G. Han, and Y. Zheng, “First-principles study of elastic properties in perovskite PbTiO_3 ,” *Mater. Sci. Eng. A*, vol. 472, no. 1–2, pp. 269–272, 2008.
- [34] R. A. P. Ribeiro and S. R. De Lázaro, “Theoretical Investigations of the Bulk Modulus in the Tetra-Cubic Transition of PbTiO_3 Material,” *Quim. Nov.*, vol. 37, no. 7, pp. 1165–1170, 2014.
- [35] M. Okuyama and Y. Hamakawa, “Preparation and basic properties of PbTiO_3 ferroelectric thin films and their device applications,” *Ferroelectrics*, vol. 63, no. 1, pp. 243–252, 1985.
- [36] H. Takeuchi, S. Jyomura, Y. Ito, and K. Nagatsuma, “Rare-earth substituted piezoelectric PbTiO_3 ceramics for acoustic wave applications,” *Ferroelectrics*, vol. 51, no. 1, pp. 71–80, 1983.
- [37] Y. Ito, H. Takeuchi, S. Jyomura, K. Nagatsuma, and S. Ashida, “Temperature-compensated PbTiO_3 ceramics for surface acoustic wave applications,” vol. 35, no. October, pp. 595–597, 1979.
- [38] Z. Feng, H. Luo, Z. Yin, C. Guang, and N. Ling, “High electric-field-induced strain of $\text{Pb}(\text{Mg}_{1/3}\text{Nb}_{2/3})\text{O}_3\text{-PbTiO}_3$ crystals and their application in multilayer actuators,” *Appl. Phys. A Mater. Sci. Process.*, vol. 81, no. 6, pp. 1245–1248, 2005.
- [39] S. C. Woody, S. T. Smith, X. Jiang, and P. W. Rehrig, “Performance of single-crystal $\text{Pb}(\text{Mg}_{1/3}\text{Nb}_{2/3})\text{-32}\%\text{PbTiO}_3$ stacked actuators with application to adaptive structures,” *Rev. Sci. Instrum.*, vol. 76, no. 7, p. 75112, 2005.
- [40] L. L. Sun, O. K. Tan, W. G. Liu, W. G. Zhu, and X. Yao, “Poling of multilayer $\text{Pb}(\text{Zr}_{0.3}\text{Ti}_{0.7})\text{O}_3/\text{PbTiO}_3$ thin film for pyroelectric infrared sensor application,” *Infrared Phys. Technol.*, vol. 44, no. 3, pp. 177–182, 2003.
- [41] J. S. Jang *et al.*, “Vertically Aligned Core–Shell PbTiO_3 @ TiO_2 Heterojunction Nanotube Array for Photoelectrochemical and Photocatalytic Applications,” *J. Phys. Chem. C*, vol. 121, no. 28, pp. 15063–15070, 2017.

- [42] A. Sobhani-Nasab, M. Rangraz-Jeddy, A. Avanes, and M. Salavati-Niasari, "Novel sol-gel method for synthesis of PbTiO_3 and its light harvesting applications," *J. Mater. Sci. Mater. Electron.*, vol. 26, no. 12, pp. 9552–9560, 2015.
- [43] D. Arney, T. Watkins, and P. A. Maggard, "Effects of particle surface areas and microstructures on photocatalytic H_2 and O_2 production over PbTiO_3 ," *J. Am. Ceram. Soc.*, vol. 94, no. 5, pp. 1483–1489, 2011.
- [44] L. V. Bora and R. K. Mewada, "Visible/solar light active photocatalysts for organic effluent treatment: Fundamentals, mechanisms and parametric review," *Renew. Sustain. Energy Rev.*, vol. 76, no. November 2015, pp. 1393–1421, 2017.
- [45] J. Y. Do, Y. Im, B. S. Kwak, S. M. Park, and M. Kang, "Preparation of basalt fiber@perovskite PbTiO_3 core-shell composites and their effects on CH_4 production from CO_2 photoreduction," *Ceram. Int.*, vol. 42, no. 5, pp. 5942–5951, 2016.
- [46] L. G. Tejuca and L. G. Fierro, *Properties and Applications of Perovskite-Type Oxides*. 1993.
- [47] D. G. Wang, C. Z. Chen, J. Ma, and T. H. Liu, "Lead-based titanate ferroelectric thin films fabricated by a sol-gel technique," *Appl. Surf. Sci.*, vol. 255, no. 5 PART 1, pp. 1637–1645, 2008.
- [48] N. Solids, J. Phillips, and O.- Ch, "Non-crystalline solids," *Science (80-.)*, vol. 148, pp. 285–290, 1992.
- [49] S. M. Selbach, G. Wang, M. A. Einarsrud, and T. Grande, "Decomposition and crystallization of a sol-gel-derived PbTiO_3 precursor," *J. Am. Ceram. Soc.*, vol. 90, no. 8, pp. 2649–2652, 2007.
- [50] B. A. Hernandez-sanchez *et al.*, "Examination of Size-Induced Ferroelectric Phase Transitions in Template synthesised PbTiO_3 Nanotubes and Nanofibers," *Chem. Mater.*, vol. 2, no. 7, pp. 5909–5919, 2005.
- [51] R. Wongmaneerung, R. Yimmirun, and S. Ananta, "Effects of sintering condition on phase formation, microstructure and dielectric properties of lead titanate ceramics," *Appl. Phys. A Mater. Sci. Process.*, vol. 86, no. 2, pp. 249–

- 255, 2007.
- [52] J. Ryu, J.-J. Choi, and H.-E. Kim, "Effect of Heating Rate on the Sintering Behavior and the Piezoelectric Properties of Lead Zirconate Titanate Ceramics," *J. Am. Ceram. Soc.*, vol. 84, no. 4, pp. 902–904, 2001.
- [53] H. Espenschied and S. Cole, "Lead Titanate: Crystal Structure, Temperature of Formation, and Specific Gravity Data," *J. Phys. Chem.*, vol. 41, no. 8, pp. 445–451, 1936.
- [54] J. B. Blum and S. R. Gurkovich, "Sol-gel-derived PbTiO₃," *J. Mater. Sci.*, vol. 20, no. 12, pp. 4479–4483, 1985.
- [55] Z. Nurbaya *et al.*, "Fabrication of PVDF-TrFE based bilayered PbTiO₃/PVDF-TrFE films capacitor," *AIP Conf. Proc.*, vol. 1733, 2016.
- [56] S. Kim, M. Jun, and S. Hwang, "Preparation of Undoped Lead Titanate Ceramics via Sol – Gel Processing," *J. Am. Ceram. Soc.*, vol. 96, no. 2, pp. 289–296, 1999.
- [57] P. Löbmann, W. Glaubitt, J. Gross, and J. Fricke, "Preparation and characterization of lead titanate aerogels," *J. Non. Cryst. Solids*, vol. 186, pp. 59–63, 1995.
- [58] H. Cheng, J. Ma, and Z. Zhao, "Hydrothermal Synthesis of PbO-TiO₂ Solid Solution," *Chem. Mater.*, vol. 6, no. 7, pp. 1033–1040, 1994.
- [59] Z. Zhang, P. Wu, L. Lu, and C. Shu, "Study on vacancy formation in ferroelectric PbTiO₃ from ab initio," *Appl. Phys. Lett.*, vol. 88, no. 14, pp. 14–17, 2006.
- [60] T. Shimada, Y. Uratani, and T. Kitamura, "Emergence of ferromagnetism at a vacancy on a non-magnetic ferroelectric PbTiO₃ surface: A first-principles study," *Acta Mater.*, vol. 60, no. 18, pp. 6322–6330, 2012.
- [61] I. Nakamura, N. Negishi, S. Kutsuna, T. Ihara, S. Sugihara, and K. Takeuchi, "Role of oxygen vacancy in the plasma-treated TiO₂ photocatalyst with visible light activity for NO removal," *J. Mol. Cat. A.*, vol. 161, no. 1–2, pp. 205–212, 2000.

- [62] X. Sun *et al.*, “Hydrothermal synthesis and photocatalytic activity of Li-doped PbTiO₃ perovskite cubic particles,” *Surf. Coatings Technol.*, vol. 320, no. 3, pp. 527–530, 2017.
- [63] A. Stashans, S. Serrano, and P. Medina, “A quantum-chemical study of oxygen-vacancy defects in PbTiO₃ crystals,” *Phys. B Condens. Matter*, vol. 381, no. 1–2, pp. 82–89, 2006.
- [64] F. F. Ge *et al.*, “The structure and defect formation energy in tetragonal PbTiO₃: Ab initio calculation,” *Ferroelectrics*, vol. 401, no. 1, pp. 154–160, 2010.
- [65] H. Gu *et al.*, “Fabrication of lead titanate single crystalline nanowires by hydrothermal method and their characterization,” *J. Sol-Gel Sci. Technol.*, vol. 42, no. 3, pp. 293–297, 2007.
- [66] K. Nishida *et al.*, “Investigation of PbTiO₃ thin films with reduced and re-oxidized treatment using Raman spectroscopy,” *J. Ceram. Soc. Japan*, vol. 121, no. 1417, pp. 859–862, 2013.
- [67] K. Nishida *et al.*, “Oxygen vacancies in PbTiO₃ thin films probed by resonant Raman spectroscopy,” *J. Ceram. Soc. Japan*, vol. 121, no. 1416, pp. 598–601, 2013.
- [68] W. Zhao and Q. Zhong, “The effect of oxygen vacancies and fluorine dopant over adsorption behaviours of V₂O₅/TiO₂ for NO removal,” *RSC Adv.*, vol. 4, no. 11, pp. 5653–5659, 2014.
- [69] D. Zhang *et al.*, “Au nanoparticles enhanced rutile TiO₂ nanorod bundles with high visible-light photocatalytic performance for NO oxidation,” *Appl. Catal. B Environ.*, vol. 147, pp. 610–616, 2014.
- [70] H. Li, S. Yin, Y. Wang, T. Sekino, S. W. Lee, and T. Sato, “Roles of Cr³⁺-doping and oxygen vacancies in SrTiO₃ photocatalysts with high visible light activity for NO removal,” *J. Catal.*, vol. 297, pp. 65–69, 2013.
- [71] J. Ma, H. Wu, Y. Liu, and H. He, “Photocatalytic Removal of NO_x over Visible Light Responsive Oxygen-Deficient TiO₂,” *J. Phys. Chem. C*, vol. 118, no. 14, pp. 7434–7441, 2014.

- [72] J. A. Mendoza, D. H. Lee, and J. H. Kang, "Photocatalytic removal of gaseous nitrogen oxides using WO₃/TiO₂ particles under visible light irradiation: Effect of surface modification," *Chemosphere*, vol. 182, pp. 539–546, 2017.
- [73] L. Guo, Q. Zhong, J. Ding, Z. Lv, W. Zhao, and Z. Deng, "Low-temperature NO_x (x = 1, 2) removal with ·OH radicals from catalytic ozonation over a RGO–CeO₂ nanocomposite: the highly promotional effect of oxygen vacancies," *RSC Adv.*, vol. 6, no. 91, pp. 87869–87877, 2016.
- [74] S. Cai, S. Yu, W. Wan, W. Wen, and Y. Zhou, "Self-template synthesis of ATiO₃ (A = Ba, Pb and Sr) perovskites for photocatalytic removal of NO," *RSC Adv.*, vol. 7, no. 44, pp. 27397–27404, 2017.
- [75] D. Uner, I. Bayar, and T. Tabari, "The influence of relative humidity on photocatalytic oxidation of nitric oxide (NO) over TiO₂," *Appl. Surf. Sci.*, vol. 354, pp. 260–266, 2015.
- [76] R. Hailili, G. Dong, Y. Ma, S. Jin, C. Wang, and T. Xu, "Layered Perovskite Pb₂Bi₄Ti₅O₁₈ for Excellent Visible Light-Driven Photocatalytic NO Removal," *Ind. Eng. Chem. Res.*, vol. 56, no. 11, pp. 2908–2916, 2017.
- [77] Q. Zhang *et al.*, "Perovskite LaFeO₃-SrTiO₃ composite for synergistically enhanced NO removal under visible light excitation," *Appl. Catal. B Environ.*, vol. 204, pp. 346–357, 2017.
- [78] L. Wu, C. Liang, and C.-F. Shieu, "Piezoelectric properties of (Pb,Sr)(Zr,Ti,Mn,Zn,Nb)O₃ piezoelectric ceramic," *J. Mater. Sci.*, vol. 26, pp. 4439–4444, 1991.
- [79] G. King and E. Goo, "Crystal Structure and Defects of Ordered (Pb_{1-x}Ca_x)TiO₃," *J. Am. Ceram. Soc.*, vol. 60, pp. 454–460, 1988.
- [80] R. Poyato, M. Algueró, M. L. Calzada, and L. Pardo, "Enhancement of the 90° domain-wall mobility in sol-gel (Pb,La)TiO₃ thin films prepared by multiple deposition and crystallization," *J. Appl. Phys.*, vol. 98, no. 2, 2005.
- [81] R. Poyato, M. L. Calzada, L. Pardo, J. García López, and M. A. Respaldiza, "Compositional and structural study of ferroelectric multilayer (Pb,La)TiO₃/(Pb,Ca)TiO₃ sol-gel thin films," *J. Eur. Ceram. Soc.*, vol. 24, no.

- 6, pp. 1615–1619, 2004.
- [82] A. R. Raju and C. N. R. Rao, “Oriented ferroelectric thin films of PbTiO_3 , $(\text{Pb,La})\text{TiO}_3$, and $\text{Pb}(\text{Zr,Ti})\text{O}_3$ by nebulized spray pyrolysis,” *Appl. Phys. Lett.*, vol. 896, no. 1995, p. 896, 1995.
- [83] J. Zhu *et al.*, “Microstructure, domain structures and ferroelectric properties in $(\text{Pb}_{0.8},\text{La}_{0.1}\text{Ca}_{0.1})\text{TiO}_3/\text{Pb}(\text{Zr}_{0.2}\text{Ti}_{0.8})\text{O}_3$ bilayered thin film,” *Thin Solid Films*, vol. 518, no. 1, pp. 392–395, 2009.
- [84] C. C. Chou, C. S. Hou, and T. H. Yeh, “Domain pinning behavior of ferroelectric $\text{Pb}_{1-x}\text{Sr}_x\text{TiO}_3$ ceramics,” *J. Eur. Ceram. Soc.*, vol. 25, no. 12 SPEC. ISS., pp. 2505–2508, 2005.
- [85] S. Ikegami, “Electromechanical Properties of PbTiO_3 Ceramics Containing La and Mn,” *J. Acoust. Soc. Am.*, vol. 50, no. 4A, p. 1060, 1971.
- [86] J. Cho, I. Park, H. Kim, and H. Chung, “Sintering Behavior of Cadmium-Doped $\text{Pb}(\text{Ni}_{1/3}\text{Nb}_{2/3})\text{O}_3\text{--PbZrO}_3\text{--PbTiO}_3$ Ceramics,” *J. Am. Ceram. Soc.*, vol. 80, no. 6, pp. 1523–1534, 1997.
- [87] M. M. Kumar, “Effect of A and B Site Cations on the Dielectric and Electrical Properties of PbTiO_3 ,” *Analysis*, vol. 583, pp. 583–591, 2000.
- [88] W. Zhou, H. Deng, L. Yu, P. Yang, and J. Chu, “Optical band-gap narrowing in perovskite ferroelectric ABO_3 ceramics (A=Pb, Ba; B=Ti) by ion substitution technique,” *Ceram. Int.*, vol. 41, pp. 13389–13392, 2015.
- [89] C. Sun, J. Wang, P. Hu, M. J. Kim, and X. Xing, “Effects of Al substitution on the spontaneous polarization and lattice dynamics of the $\text{PbTi}_{1-x}\text{Al}_x\text{O}_3$,” *Dalt. Trans.*, vol. 39, no. 21, pp. 5183–5186, 2010.
- [90] L. Yang, Y. Wang, X. Wang, Y. Wang, and G. Han, “Hydrothermal Synthesis and Characterization of PbTiO_3 microrods,” *Adv. Mater. Res.*, vol. 149, pp. 903–906, 2011.
- [91] S. Deng *et al.*, “Hydrothermal Synthesis of Single-Crystalline Perovskite PbTiO_3 Nanosheets with Dominant (001) Facets,” *Inorg. Chem.*, vol. 53, no. 20, pp. 10937–43, 2014.

- [92] G. Dai, S. Liu, Y. Liang, and T. Luo, "Synthesis and enhanced photoelectrocatalytic activity of p-n junction $\text{Co}_3\text{O}_4/\text{TiO}_2$ nanotube arrays," *Appl. Surf. Sci.*, vol. 264, pp. 157–161, 2013.
- [93] L. Gao *et al.*, "Synthesis of octahedral Co_3O_4 via carbon-assisted method," *Appl. Surf. Sci.*, vol. 264, no. 2, pp. 85–87, 2015.
- [94] S. S. Kim, H. H. Lee, and S. C. Hong, "A study on the effect of support's reducibility on the reverse water-gas shift reaction over Pt catalysts," *Appl. Catal. A Gen.*, vol. 423–424, pp. 100–107, 2012.

APPENDIX A

SYNTHESIS



Figure A.1 The color of mixtures that contains LAT, CAT and solvents (a: PbTiO_3 , b: $\text{Pb}_{0.875}\text{Co}_{0.125}\text{TiO}_3$, c: $\text{Pb}_{0.75}\text{Co}_{0.25}\text{TiO}_3$, d: $\text{Pb}_{0.5}\text{Co}_{0.5}\text{TiO}_3$)

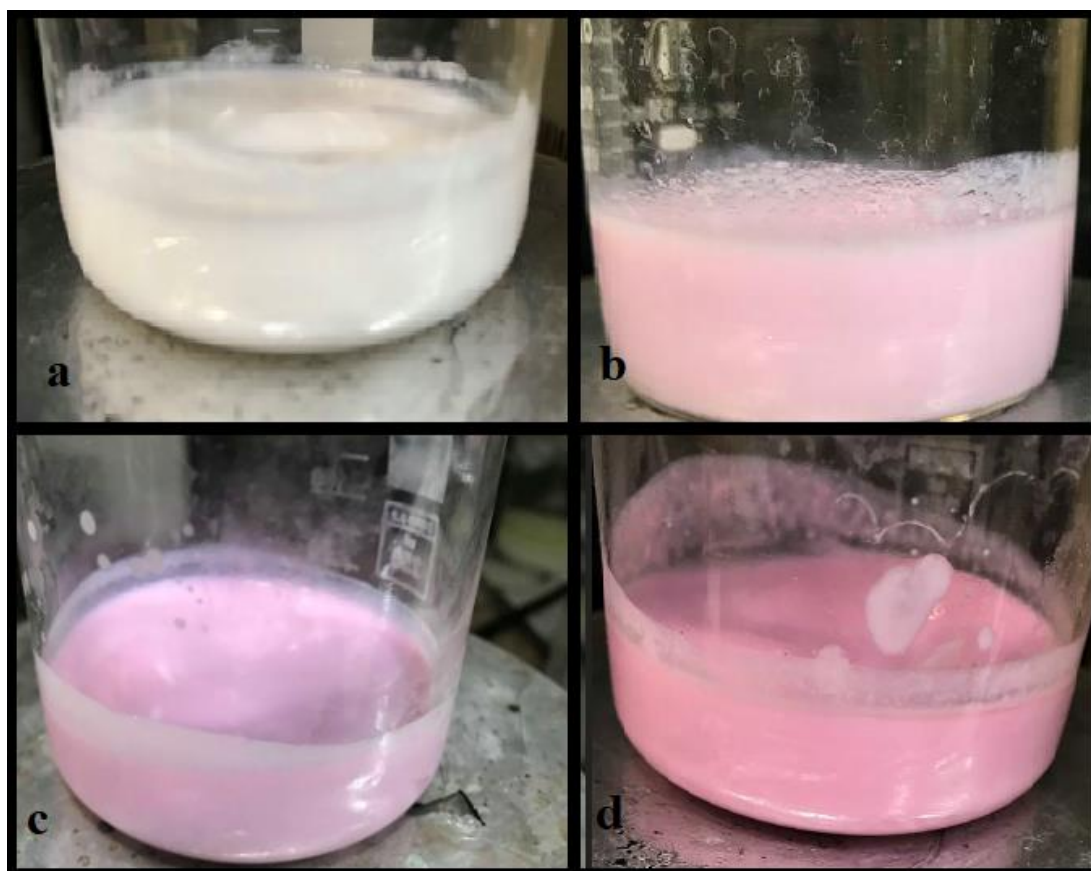


Figure A.2 The color of gel formed after the addition of CA- ethanol mixture (a: PbTiO_3 , b: $\text{Pb}_{0.875}\text{Co}_{0.125}\text{TiO}_3$, c: $\text{Pb}_{0.75}\text{Co}_{0.25}\text{TiO}_3$, d: $\text{Pb}_{0.5}\text{Co}_{0.5}\text{TiO}_3$)

APPENDIX B

NO OXIDATION REACTOR



Figure B.1 The photoreactor used in photocatalytic NO Oxidation experiments

APPENDIX C

EXPERIMENTAL PROCEDURE

NO Oxidation Experiments

1. Turn on the NO_x analyzer.
2. Let the instrument stabilize.
3. Turn the ozonator on.
4. Let the instrument stabilize.
5. Place coated flat glasses in the reactor.
6. Connect the reactor to the set up with plastic pipes.
7. Cover the reactor with a light-proof material.
8. Set the flow rate using mass flow controller.
9. Let the air flow through by-pass line.
10. Let the air flow through reactor.
11. Replace the light-proof material.
12. Turn on the UV lamp to get rid of organic and inorganic materials that the catalyst may contain.
13. Monitor NO₂ concent
14. Turn off the UV light when NO₂ produced is less than 10 ppb.
15. Cover the reactor with a light-proof material.
16. Let the air flow through by-pass line.
17. Set the initial NO concentration using mass flow controller.
18. Change the mood to manual NO and change the averaging time to 1 second.
19. Let the NO signal stabilize.
20. Let the air flow through reactor.
21. Wait for 20-30 minutes under air flow.

22. Replace the light-proof material.
23. Turn on the UV lamp for NO oxidation reaction.
24. Expose the reactor to UV-irradiation for 15-20 minutes.
25. Turn off the UV lamp.
26. Cover the reactor with light-proof material.
27. Wait for 5 minutes.
28. Replace the light-proof material.
29. Turn on the visible light source.
30. Expose the reactor to visible light irradiation for 15-20 minutes.
31. Turn off the visible light source.
32. Cover the reactor with a light-proof material.
33. Stop the NO flow.
34. Purge the reactor with air.
35. Let the air flow through by-pass line.

TP_x Experiments

Temperature Programmed Reduction

1. Place the sample between the pieces of quartz wool in the reactor.
2. Connect the reactor to Chemisorb 2720 equipment.
3. Confine the reactor in the furnace.
4. Place insulation materials on the top of furnace to avoid heat loss to environment.
5. Prepare a mixture of water, ice and isopropyl alcohol as cold trap.
6. Install cold-trap and put insulator material on the top of cold trap.
7. Switch the valves to by-pass and short path.
8. Push the Port A button which lets He to the system.
9. Open the helium gas cylinder valve.
10. Turn Chemisorb 2720 equipment on.
11. Check the flow rate. If it is different than 25 sscm, fix it at 25 sscm.
12. Turn the TP_x system on.
13. Adjust the maximum temperature, heating rate and dwell time using TP_x system.

14. Turn the computer on.
15. Open the TPx software. Click on File→Open→Sample. Enter the sample information. Choose the Analysis Condition as TPR. Click on Unit 1→Start Analysis.
16. After the TCD signal is stabilized, namely, by-pass and short path is purged, change the position of the valves to sample and long path.
17. Purge the system with helium.
18. Push the - polarity button on the equipment.
19. Open the 10% H₂-Ar gas cylinder valve.
20. Push the Port B button which lets hydrogen to the system.
21. Wait until the TCD signal is stabilized.
22. Start heating the sample using TP_x system as soon as starting recording the TCD signal, time and temperature.
23. Stop recording when the maximum temperature is reached.
24. Wait until the temperature of the sample reaches 400
25. Open the furnace and wait until the temperature reaches 200
26. Turn the cooling fan on.
27. Wait until the temperature reaches the ambient temperature.
28. Push the Port A button to get rid off the hydrogen gas inside the equipment.
29. Change the valves to short path and by-pass.
30. Turn the computer, TPx system and Chemisorb 2720 equipment off.
31. Close the gas cylinder valves.

UV Desorption

1. Place the sample between the pieces of quartz wool in the reactor.
2. Connect the reactor to Chemisorb 2720 equipment.
3. Place the UV lamp in front of the reactor.
4. Switch the valves to by-pass and short path.
5. Push the Port A button which lets He to the system.
6. Open the helium gas cylinder valve.
7. Turn Chemisorb 2720 equipment on.
8. Check the flow rate. If it is different than 25 sscm, fix it at 25 sscm.

9. Turn the computer on.
10. Open the TPx software. Click on File→Open→Sample. Enter the sample information. Choose the Analysis Condition as TPtD. Click on Unit 1→Start Analysis.
11. After the TCD signal is stabilized, namely, by-pass and short path is purged, change the position of the valves to sample and long path.
12. Push the - polarity button on the equipment.
13. Purge the system with helium.
14. Wait until the TCD Signal is stabilized.
15. Turn the UV lamp on and start recording the data for 2 hours.
16. Stop recording and turn off the UV lamp.
17. Change the valves to short path and by-pass.
18. Turn the computer, TPx system and Chemisorb 2720 equipment off.
19. Close the gas cylinder valves.

APPENDIX D

REACTOR ANALYSIS

Reactor analysis on NO reactor was done using TiO₂. Since there are many studies about NO oxidation over TiO₂, the reliability of the experiments was checked using TiO₂ and the results provided a basis for the experiments conducted by using synthesized perovskites.

CSTR Assumption

NO Oxidation reaction is assumed to be first order and irreversible.

Design equation for CSTR is given as:

$$F_{A_0} - F_A + r_A V = 0 \quad \text{Equation D.1}$$

Assume the reaction as first order and irreversible.

$$\frac{F_{A_0} x}{k c_{A_0} (1-x)} = V \text{ where } r_A = -k c_{A_0} (1-x) \text{ and } F_A = F_{A_0} (1-x) \quad \text{Equation D.2}$$

$$\frac{F_{A_0}}{V} = \frac{c_{A_0} v}{V} = \frac{c_{A_0}}{\tau} \quad \text{Equation D.3}$$

$$\frac{x}{1-x} = k\tau \quad \text{Equation D.4}$$

$y = mx$ so the slope of y vs x graph gives m (which is k)

Table D.1 Parameters for CSTR Assumption

v_0 (L/min)	C_{NO_0} (ppb)	x_{NO}	τ (min)	$x/1-x$	k (1/min) calculated	% Error
0.5	500	0.98	2	49	24.5	34.3
1	250	0.86	1	6.14	6.1	435.6
1.5	167	0.78	0.67	3.55	5.3	518.6
2	125	0.71	0.5	2.45	4.9	571.9
0.5	485	0.98	2	49	24.5	34.3
1	500	0.85	1	5.67	5.7	480.6
1.5	485	0.7	0.67	2.33	3.5	840.0
2	485	0.61	0.5	1.56	3.1	951.7

k is also calculated for each step using Equation D.4.

%Error calculations are done using Equation D.5.

$$\%Error = \frac{|k_{calculated} - k_{slope\ of\ graph}|}{k_{calculated}} \times 100$$

Equation D.5

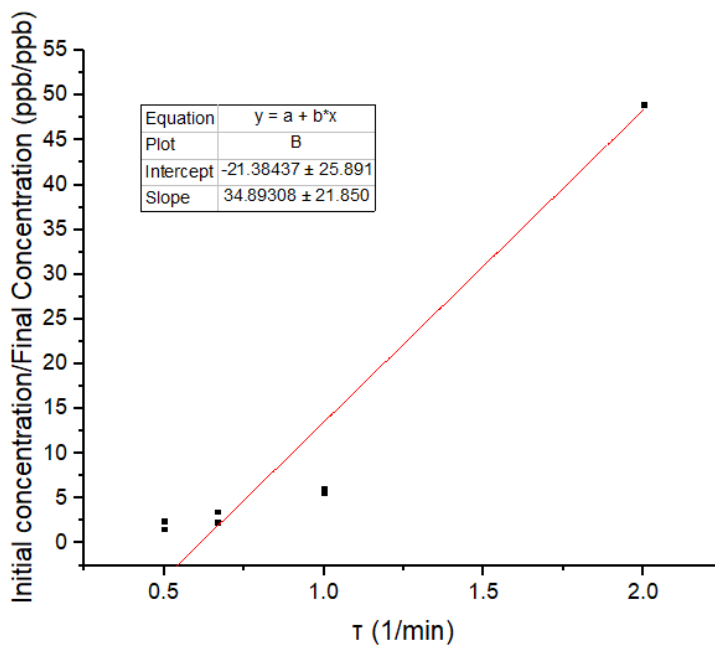


Figure D.1 c_{A0} vs τ graph for CSTR assumption

When $\tau=2$ is omitted, the graph is seen as in Figure D.2.

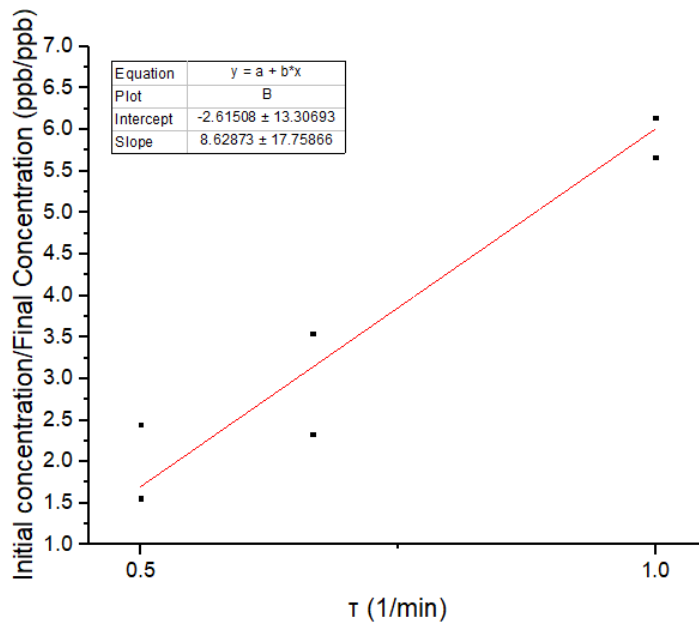


Figure D.2 c_{A0} vs τ graph for CSTR assumption ($\tau=2$ is omitted)

PFR Assumption

Design equation for PFR is given as:

$$F_{A_0} - F_A + \int_0^V r_A dV = 0 \quad \text{Equation D.6}$$

Assume the reaction as first order and irreversible.

$$\frac{dF_A}{dV} = r_A \text{ where } F_A = c_A v \quad \text{Equation D.7}$$

$$\frac{dc_A}{d(V/v)} = -k c_A \quad \text{Equation D.8}$$

$$\ln \frac{c_{A_0}}{c_A} = -k \tau \quad \text{Equation D.9}$$

$y = mx$ so the slope of y vs x graph gives m (which is k)

Table D.2 Parameters for PFR Assumption

v_0 (L/min)	C_{NO_0} (ppb)	x_{NO}	τ (min)	$x/1-x$	k (1/min) calculated	% Error
0.5	500	0.98	2.00	3.91	1.96	2.86
1.0	250	0.86	1.00	1.97	1.97	3.36
1.5	167	0.78	0.67	1.51	2.27	16.30
2.0	125	0.71	0.50	1.24	2.48	23.30
0.5	485	0.98	2.00	3.91	1.96	2.86
1.0	500	0.85	1.00	1.90	1.9	0.15
1.5	485	0.7	0.67	1.20	1.81	5.21
2.0	485	0.61	0.50	0.94	1.88	0.89

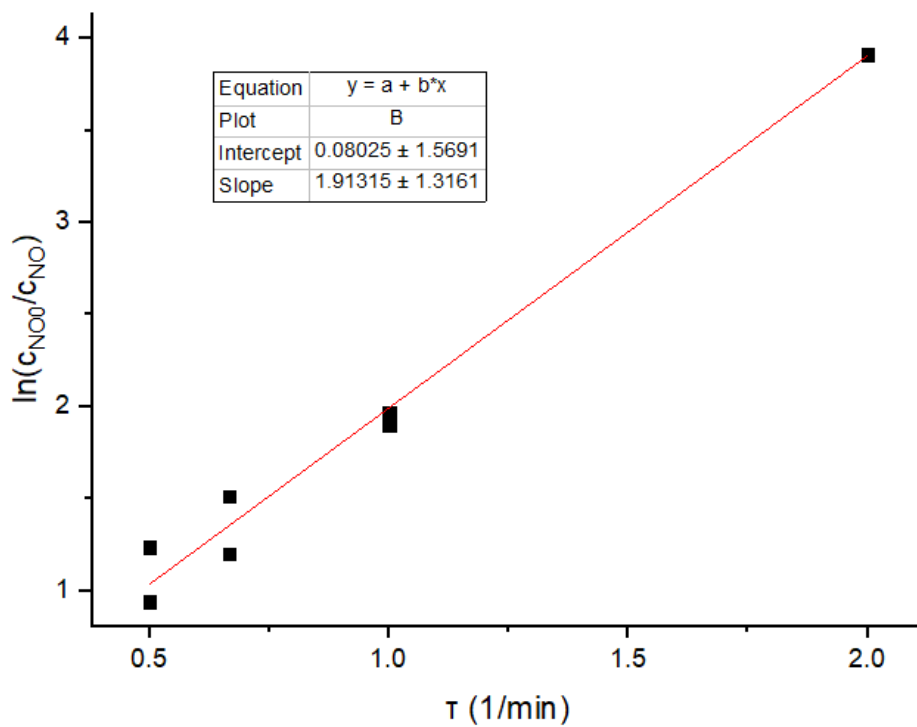


Figure D.3 $\ln(c_{A0}/c_A)$ vs τ graph for PFR Assumption

Table D.3 Comparison of CSTR and PFR Assumptions

Assumption	k (1/min)	R ²
CSTR	8.62	0.92
PFR	1.91	0.99

PFR assumption is more valid because of both R² values and %Error calculations.

APPENDIX E

TPR OF $\text{Pb}_{0.875}\text{Co}_{0.125}\text{TiO}_3$ BEFORE AND AFTER PHOTODESORPTION

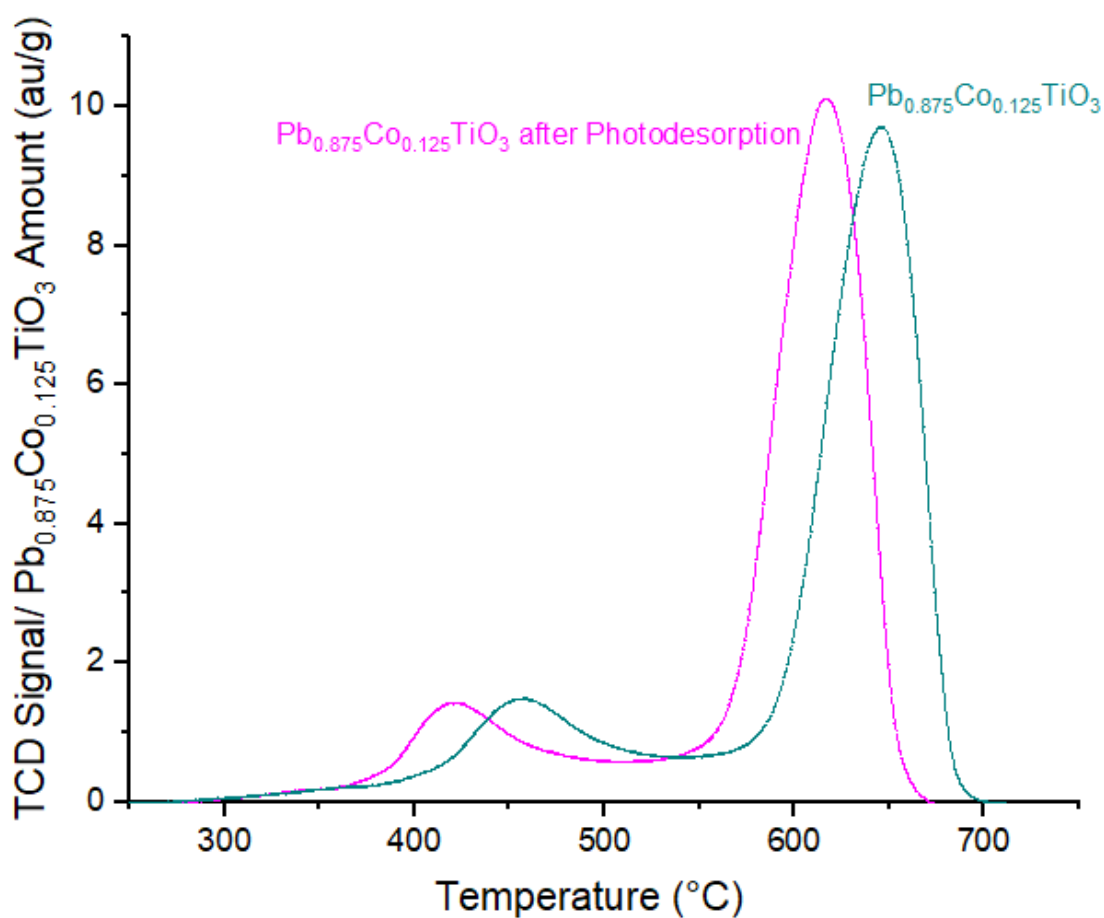


Figure E.1 TPR profile of $\text{Pb}_{0.875}\text{Co}_{0.125}\text{TiO}_3$ before and after photodesorption

Figure E.1 shows that there are two peaks for $\text{Pb}_{0.875}\text{Co}_{0.125}\text{TiO}_3$ before and after photodesorption. For UV treated sample the first and second peaks are at 420 $^{\circ}\text{C}$ and 617 $^{\circ}\text{C}$, respectively. However, for fresh sample the first and second peaks are at 455 $^{\circ}\text{C}$ and 646 $^{\circ}\text{C}$, respectively. It means that UV treated sample can be reduced at lower temperatures. On the other hand, hydrogen consumed to reduce UV-treated sample is

more than hydrogen consumed to reduce fresh sample. The area calculated under the UV treated sample was found as 67.9 au and hydrogen consumed to reduce 1 g of sample was 5.0×10^{-3} mol.